

Experimental Investigation of Heat Transfer to Air–Water Flow in Downward Inclined Square Pipe

Rafel H. Hameed

Iraq / University of Babylon / College of Engineering / Mechanical Engineering Dept.

Email: rafel.hekmat@yahoo.com

ABSTRACT

Two-phase local heat transfer coefficient and flow pattern in 4.5 cm inner length of glass square test section downwardly pipe inclination angles of 5° , 10° , and 15° were investigated experimentally. Two superficial velocities for each air and water were used 0.164 m/s, 0.411 m/s and 1.1506 m/s, 1.4815 m/s respectively. Local heat transfer coefficient was calculated from the temperature recorded by using eight thermocouples type K positioned along the test section. It was found that the heat transfer coefficient of air-water flow increase with increasing flow rate of water, air, and inclination angle. In addition a high speed camera was used in order to obtain images sequence of the flow under different selected conditions. The flow regimes, which are stratified, intermittent, and annular flow are observed and recorded by high speed camera. At 5° inclination angle and low air-water superficial velocity stratified flow observed, transition from stratified to intermittent flow and annular flow occurs at increasing the inclination angle and air-water superficial velocity. Correlations on average Nusselt number were obtained for three inclination angle 5° , 10° , and 15° .

Keywords: local heat transfer coefficient; two-phase flow; inclined pipe; downward flow; square pipe; flow regime.

الخلاصة

تم خلال هذا البحث حساب معامل انتقال الحرارة الموقعي وملاحظة انواع انظمة الجريان عمليا لجريان ثنائي الطور نحو الاسفل وبزاويا ميل 5° ، 10° ، 15° في انبوب زجاجي ذو مقطع مربع طول ضلعه الداخلي 4.5 cm. تم استخدام سرعتين لكل من الماء والهواء حيث كانت 0.164 m/s، 0.411 m/s للهواء و 1.1506 m/s، 1.4815 m/s للماء. تم حساب معامل انتقال الحرارة الموقعي من خلال قياس درجات الحرارة المسجلة على طول انبوب الاختبار باستخدام ثمانية ثرموكبلات نوع K. لقد وجد ان معامل انتقال الحرارة للجريان الثنائي (هواء- ماء) يزداد مع زيادة معدل جريان الماء والهواء وكذلك مع ازدياد زاوية ميل الأنبوب. تم استخدام كاميرا رقمية سريعة لتصوير نمط الجريان ثنائي الطور وبأوضاع مختلفة. تم ملاحظة انماط الجريان الطباقى (stratified)، المتقطع (intermittent) و الحلقي (annular) باستخدام الكاميرا الرقمية. في حالة سرعة الماء والهواء قليلة وعندما تكون زاوية الميل 5° كان نوع الجريان المسيطر هو الطباقى ثم انتقل الى النمط المتقطع والحلقي في حالة زيادة السرعة للماء والهواء مع زيادة زاوية ميل الأنبوب. تم استنتاج معادلات تصحيحية لمعدل Nusselt لزوايا الميل المختلفة 5° ، 10° ، 15° .

1. INTRODUCTION

Two-phase flow is a characteristic term for a gas-liquid, gas-solid, or a liquid-solid flow, flowing simultaneously in a pipe, channel, or other conduit. Gas-liquid two-phase flow is the best described as the interactive motion of two different kinds of media. They are extremely important in many industrial applications: solar collectors, chemical plants, nuclear reactors, oil wells and pipelines, etc. The knowledge of non-boiling two-phase, two-component (liquid and permanent gas) heat transfer is required. When a gas-liquid mixture flows in pipe, a variety of flow pattern may occur, depending primarily on flow rates, the physical properties of the fluids, and pipe inclination angle that reported by [1].

Downward simultaneous flow of gas and liquid, although rare, is important in the chemical process industry and also in petroleum production. Gas-liquid two-phase flow heat transfer and flow patterns in inclined pipes have been studied by many researchers.

Experimental work with 10.16 cm diameter pipe, 36 m long $\pm 2^\circ$, $\pm 15^\circ$, and $\pm 30^\circ$ inclinations angle, containing oil and carbon dioxide as working fluids was observed by [2]. Superficial oil velocity between 0.2 and 2.0 m/s and superficial gas velocity between 1 and 4 m/s were used. They were observed that the dominant regime for upward inclinations was slug flow. No stratified flow was observed for these conditions. As the angle of upward inclination increases from 2° to 15° , the transition from plug to slug flow occurs at higher superficial gas velocities. As the angle of downward inclination increases, the transition from stratified to slug flow occurs at higher liquid and gas flow rates. The transition from slug to annular flow occurred at slightly higher gas flow rates when inclination was changed from -2° to -15° . However, little difference was found during the transition from slug to annular flow when the inclination was changed from -15° to -30° . Experimental work to study the flow regimes and heat transfer in air-water flow in 8° inclined tube of inner diameter of 49.2 and 25 mm were performed by [3]. The thermal pattern on the heated wall and local heat transfer coefficients were obtained by infrared thermography. They observed the local heat transfer coefficient on the upper part of the pipe is described by empirical correlation with standard deviation of 18%. Under conditions of dry out in open annular air-water flow the heat transfer coefficient is about 2.5 to 8 times higher than that for single-phase airflow. Two-phase air-water flow and heat transfer in a 25 mm diameter horizontal pipe, the water superficial velocity varied from 24.2 m/s to 41.5 m/s and the air superficial velocity varied from 0.02 m/s to 0.09 m/s were investigated experimentally [4].

The flow patterns were visualized using a high speed video camera, and the film thickness was measured by conductive tomography technique. The heat transfer coefficient was calculated from the temperature measurements using the infrared thermography method. It was found that the heat transfer coefficient at the bottom of the pipe is up to three times higher than that at the top, and becomes more uniform around the pipe for higher air flow-rates. Correlations on local and average Nusselt number were obtained and compared to other authors. The behavior of local heat transfer coefficient was analyzed and the role of film thickness and flow patterns was clarified. A 27.9 mm stainless steel test section with a length to diameter ratio of 100 in horizontal and slightly upward inclined (2° , 5° , and 7°) positions, many experiments have been carried out by [5]. The heat transfer data points were collected under a uniform wall heat flux boundary condition ranging from about 1800 to 10900 W/m², the superficial Reynolds numbers ranging from 740 to 26000 for water and 560 to 48000 for air. They observed that the heat transfer coefficient was significantly depending on the superficial liquid, gas Reynolds numbers, inclination angle, and flow pattern. The experimental data indicated that even in a slightly upward inclined pipe, there is a significant effect on the two-phase heat transfer of air-water flow. Two-phase air-water flow in test pipe (6.5 m) long positioned at angles between -20° downwards and vertical upwards was described by [6]. Two pipe diameters were used 38 mm and 67 mm, superficial velocities for air ranged from 0.15 to 8.9 m/s and from 0.04 to 0.7 m/s for water. High speed video system was used to obtain image sequence of the flow under different selected conditions. It was found that for upward inclined flow most of the experiments fall within the slug flow regime whereas for inclined downward flow the dominant flow pattern is stratified flow. An effect of the pipe diameter was also found under certain flow conditions mainly on the liquid holdup, pressure drop and structure velocity. He was investigated that increase pipe diameter displaces the bubbly-slug transition to the right hand side on the flow pattern map for inclined flow, and for horizontal pipe the stratified-slug transition is moved up. A CFD code was used to successfully model the hydrodynamics of the slug flow pattern, using the volume of fluid model based on the Euler-Euler approach.

The principal interest of this study was to identify the effect of inclination angle in downward air-water flow on the heat transfer coefficient of two phases as well as study the effect of inclination angle in the pattern of the flow. Connection between flow parameters and heat transfer was also studied.

2. EXPERIMENTAL APPARATUS AND PROCEDURE

Experiments were carried out in a smooth transparent test section glass pipe with square cross section. The square test section with an inner length of 4.5 cm, outer length of 6.5 cm, hydraulic diameter is 4.5 cm, and over length of 400 cm was used in the experiments. The inclination angles of the test section are 5° , 10° , and 15° . The schematic description of the experimental facility is presented in Fig. 1. Water and air is used as working fluids. The water and air supply systems work independently. Water in the system was controlled by water flow meter with different measure range. The water was heated to 60°C by two heaters, and was pumped to mixer, and test section.

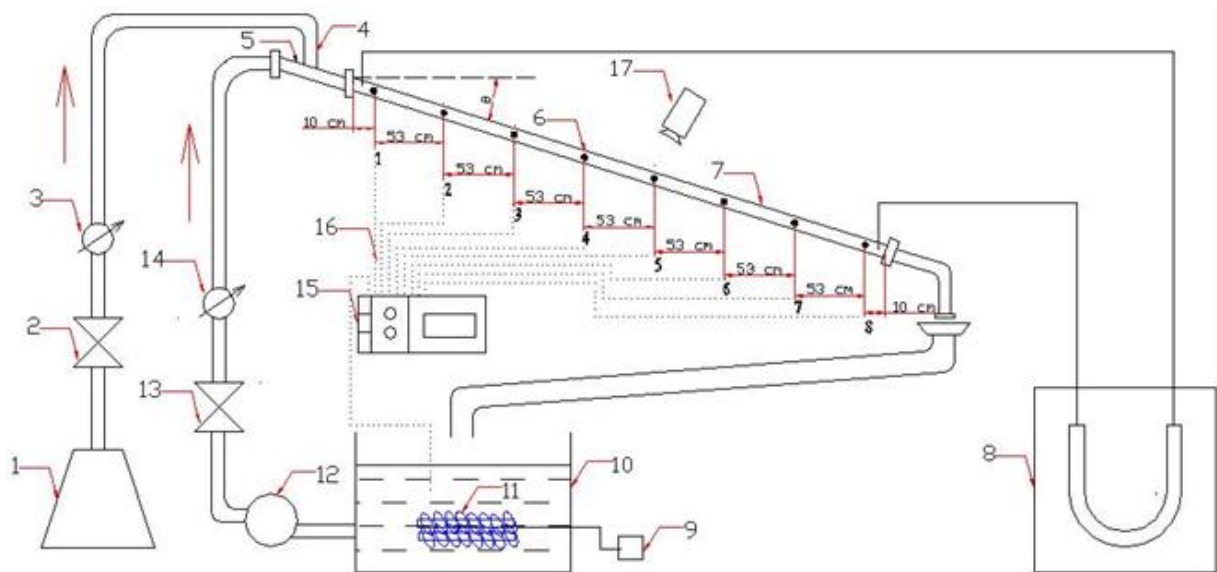


Fig. 1. Experimental facility: (1) compressor, (2) air valve, (3) air flow meter, (4) air injector, (5) air-water mixer, (6) thermocouple, (7) test section, (8) U-tube manometer, (9) power supply, (10) water tank, (11) heater, (12) pump, (13) water valve, (14) water flow meter, (15) data logger, (16) 12 channels temperature recorder device, (17) camera.

The air at 30°C and atmospheric pressure from the air compressor was pumped through air valve, the air flow meter, the air-water mixer, and the test section.

Air-water mixer was made of mild steel. Both the air and water were brought together in a mixer. Water flows through the mixer at diameter of 2.54 cm, and air from 1.27 cm of diameter, and overall length of 3.81 cm. The test section of air-water mixer was shown in Fig.2.

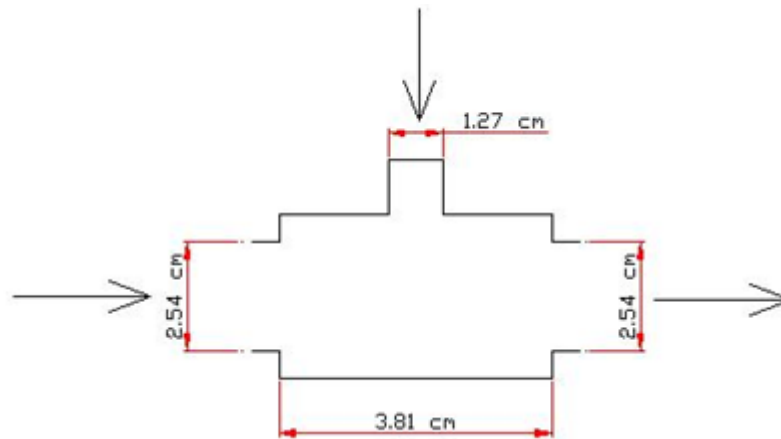


Fig. 2. Schematic diagram of air-water mixer

Eight thermocouples type K (chromium⁻ - aluminum⁺) were fixed inside the flow of test section on the equal distance between them 53cm to measure the two-phase air-water temperature. Temperature recorder with SD memory card data logger with sensor type K thermocouple was used to read the temperature with time. This device has calibration certificate with accuracy ($\pm 0.4\% \text{ }^{\circ}\text{C} + 1 \text{ }^{\circ}\text{C}$). Pressure drop at the inlet of the test section and out let was measured by using U-tube manometer. Flow pattern was detected by using a digital camera, which was used to take video capture for the flow. It uses an SD card memory with 8 GB capacity for recording and it has 14.1 Mega pixels.

All measurement equipments were calibrated by measuring actual reading with different instruments. Then, the water mass flow rate was measured with flow meter (accuracy $\pm 3\%$). Also, the air mass flow rate was measured with flow meter (accuracy $\pm 0.15\%$). The pressure drop for every test was measured by U-tube manometer (accuracy $\pm 25\%$). Experiments were carried out at two values of water superficial velocities: 1.1506 m/s and 1.4815 m/s. Then, for each water velocity two values of air superficial velocities were used (0.164 m/s and 0.411 m/s) through every experimental test. For each combination of water and air velocities experiments were carried out for the following values of pipe inclination angles: 5° , 10° , 15° . For each inclination angle of the pipe and for each air and water velocity considered temperatures were recording from all eight thermocouples to calculate heat transfer coefficient of two phase flow experimentally. Photograph type-of flow happened run in each case was detected by using a digital camera.

3. ANALYTICAL CONSIDERATIONS

A heat transfer coefficient for the two-phase flow was calculated experimentally as reported by [5]:

$$h_{TP_EXP} = \frac{1}{L} \int \bar{h} \, dz = \frac{1}{L} \sum_{k=1}^{N_{ST}} \bar{h}_k \Delta z_k \quad (1)$$

Where $Q = h A \Delta T$, then

$$h_{TP_EXP} = \frac{1}{L} \sum_{k=1}^{N_{ST}} \left(\frac{Q}{A (\bar{T}_w - T_b)} \right)_k \Delta z_k \quad (2)$$

Where \bar{h} ($W/m^2 \cdot ^\circ C$) is the local mean heat transfer coefficient, L (cm) is the length of the test section, k is the index of the thermocouple stations, N_{ST} is the number of the thermocouple station, and Δz (cm) is the distance between each thermocouple 53 cm. Fig. 3 shows the axial distance along the test section. Where Q (W) is the electrical power supply to heat the water in the tank until $60^\circ C$. Using a single digital voltmeter device to measure the voltage. The current was measured by single digital ammeter device. Then, the electrical power ($P=VI$) supply to heaters as electrical energy rate Q , which equal (4034 W). A is the wetted area in each thermocouple station (cm^2), which was calculated ($A=4 \times a \times b$) as shown in Fig. 4. T_b is the bulk temperature in each thermocouple station, which equal the temperature recorded by temperature recorder with SD card data logger with time (air-water temperature). T_w is the water temperature.

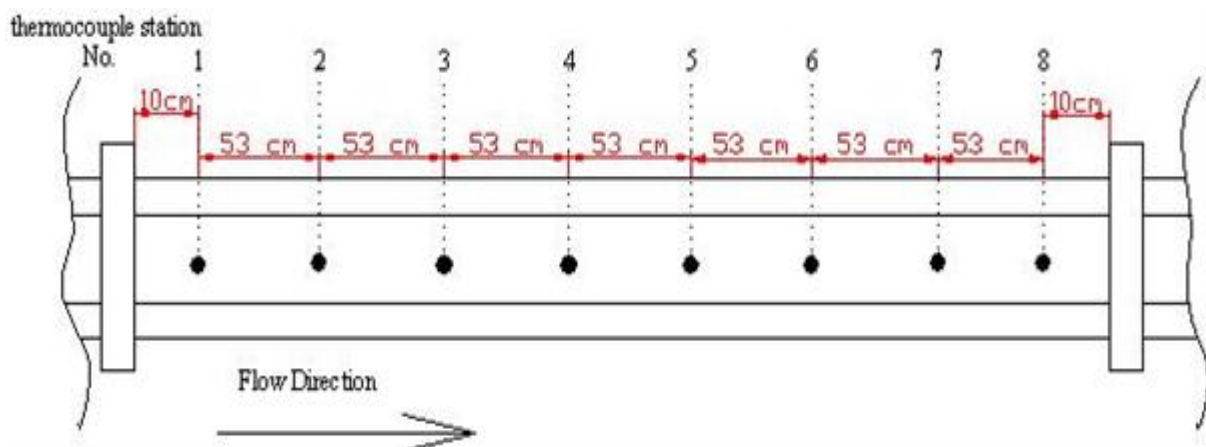


Fig.3. Axial distance along the test section.

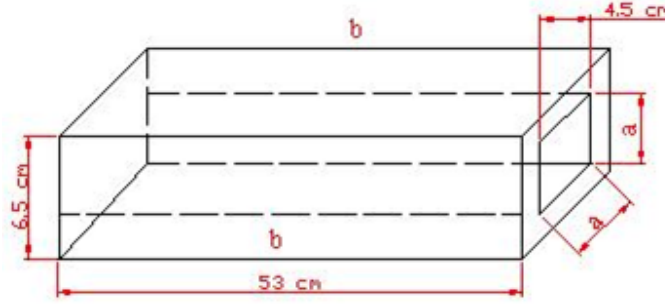


Fig. 4. Element of wetted area

All the temperature readings with time in the experimental work of these channels were calibrated with accuracy factor ± 1.004 in order to get the true value of temperature readings. \bar{T}_w is the wall temperature of test section in each thermocouple station its calculated by using finite difference analysis by using heat conduction balance at steady state condition eq. (3). In this calculation, axial conduction was assumed negligible, but heat conduction through glass test section wall was included as shown in Fig.5.

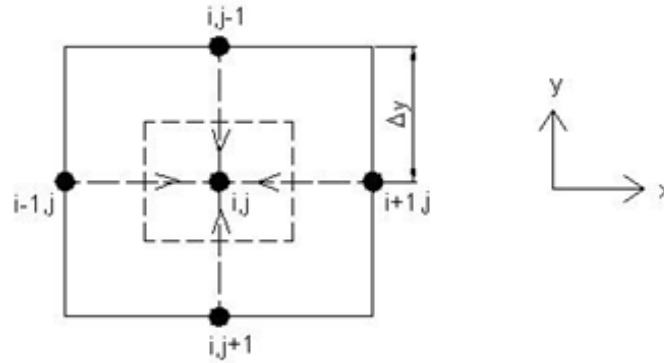


Fig. 5 Finite-difference grid arrangement

$$\frac{\partial^2 T}{\partial x^2} + \frac{\partial^2 T}{\partial y^2} = 0 \quad (3)$$

Represent eq. (3) in finite difference form

$$\frac{T_{i+1,j} - 2T_{i,j} + T_{i-1,j}}{\Delta x^2} + \frac{T_{i,j+1} - 2T_{i,j} + T_{i,j-1}}{\Delta y^2} = 0 \quad (4)$$

As assumption the axial conduction negligible, then eq. (4) becomes

$$\frac{T_{i,j+1} - 2T_{i,j} + T_{i,j-1}}{\Delta y^2} = 0 \quad (5)$$

Where $T_{i,j-1}$ was represented the ambient temperature of laboratory, $T_{i,j}$ was the wall temperature, which was calculated by eq. (5), and $T_{i,j+1}$ was represented the air-water temperature measured by sensor 1.

The non-dimensional parameters chosen for the analysis are liquid Nusselt number (Nu_L), liquid Froude number (Fr_L), and the gas Reynolds number (Re_G). (Nu_L), (Re_G) are calculated by the laws which are described by [4] as:

$$Nu_l = \frac{hD_h}{k_l} \quad (6)$$

Where h ($W/m^2 \text{ } ^\circ C$) is the heat transfer coefficient, D_h is the hydraulic diameter of test section 4.5 cm, and k_L ($W/m \text{ } ^\circ C$) is the thermal conductivity of the water at $60 \text{ } ^\circ C$.

The Reynolds number of air (Re_G) was calculated as:

$$Re_G = \frac{u_G D_h}{\nu_G} \quad (7)$$

Where u_G (m/s) is the velocity of air, d_p (cm) is the hydraulic diameter of test section, ν_G (m^2/s) is the kinematics viscosity of air at $30 \text{ } ^\circ C$

The Froude number of liquid was presented by [7] as:

$$Fr_l = \frac{u_l}{\sqrt{g D_h \sin \theta}} \quad (8)$$

Where u_L (m/s) is the velocity of water, g is the acceleration gravity ($9.81 \text{ m}^2/s$), θ is the inclination angle of test section, and D_h is the hydraulic diameter of test section.

4. RESULT AND DISCUSION

4.1. Heat Transfer Results

Figures (6) and (7) represent the thermocouple readings along the test section at different stations for test run in two-phase flow from values of water Reynolds numbers 108094.106 to 139180.791 and with two values of air Reynolds numbers 461.222 and 1153.055 with different angle values of inclination at interval time 5 seconds. Each figure shows the relationship between average temperature of air-water and the distance of thermocouple station along the square test section. The response was a downward relationship. The average temperature of air-water flow decreases at different station in test section. This is due to the heating water was cooled down by air. The heat was dissipation from the wall of the rig tube by heat transfer. This dissipation of heat was calculated in the analysis in order to calculate local heat transfer coefficient in each thermocouple station along the test section.

It has been shown the level of average temperature of air-water decreasing with increasing the inclination angles and also with increasing the water superficial velocity, and air superficial velocity (i.e. increasing the values of Reynolds numbers of water and air). Each run dependent upon three factors water velocity, air velocity and temperature of water in tank. These conditions will control on temperature readings of air-water flow. These experimental results were confirmed with the experimental results of [7].

Figures (8) and (9) illustrate the relationship between the local heat transfer coefficients of air-water flow at each thermocouple station along the test section. Each figure demonstrated upward relation with one value of water velocity, and two values of air velocities 0.164 and 0.411 m/s with inclination angle values are 5° , 10° , and 15° . The local value of heat transfer coefficient was calculated through every thermocouple station dependent upon the analysis considerations, which were detailed in section 3. These results show that the calculation of local value of heat transfer coefficient increasing upward along the distance of test tube. This is due to the heat dissipation between air-water, and wall of the test section. That leads to decrease the temperature difference between the bulk temperature of two phases, and wall temperature of test tube. Then, the value of heat transfer coefficient was increased. This is due to the temperature difference was inversely proportional with heat transfer coefficient. These results show the value of (h) was increased with increasing the values of water velocity, and air velocity. Also, these results were pointed the effective of inclination angle values of a square test section on the values of (h) through the run test. It has been shown higher values of (h) with increasing the values of inclination angle.

It has been pointed from these two figures the value of (h) in station number 1 higher than another stations. This is due to the increment length from the starting of test tube to station number 1 was smaller than another increment length of others as shown in Fig.3. This produces smaller wetted area of this station than another station. Where the value of (h) was inversely proportional with wetted area as mention in eq. (2). These results consistent with result of [4].

Figure (10) describes the relationship between the calculations the overall mean values of two-phase heat transfer coefficient in all thermocouples station. These were calculated through every run for water superficial velocity 1.150 to 1.481 m/s, and air superficial velocity 0.164 to 0.411 m/s. This figure show the influence of inclination angle on the overall mean ($h_{TP\ EXP.}$). Due to gravitational effect, inclining the tube affects the flow characteristics of two-phase flow, which in turn affects the air-water heat transfer coefficient ($h_{TP\ EXP.}$).

Overall, the mean ($h_{TP\ EXP.}$) increased when the inclination angle value was increased. Also, it has been shown higher values of ($h_{TP\ EXP.}$) with increasing the air and water velocity through the experimental test. It has noted maximum value of ($h_{TP\ EXP.}$) was calculated at 15° , which was about $6900\ W/m^2 \cdot ^\circ C$ at water superficial velocity $1.48\ m/s$, and air velocity $0.411\ m/s$. These results were consistent with the results of many authors such as [3,5].

Figure (11) shows the dependence of the local Nusselt number on the parameter $Fr_L Re_G$ at $\theta=5^\circ$, $\theta=10^\circ$, and $\theta=15^\circ$. These results were calculated the average values of these parameters the local Nusselt number and $Fr_L Re_G$ with different conditions. These conditions are different values of water and air velocities through many run test of experimental work by inclining the square test section at three values of angle, from these curves of this figure, it has been produced the fitting equations for every value of inclining angle. The following equations were found to describe the experimental data:

$$Nu_L(5^\circ) = 4.953(Re_G Fr_L)^{0.089} \quad (9)$$

$$Nu_L(10^\circ) = 5.230(Re_G Fr_L)^{0.081} \quad (10)$$

$$Nu_L(15^\circ) = 5.755(Re_G Fr_L)^{0.027} \quad (11)$$

These results were conformed to the result of [4].

4.2 Flow Pattern

It is not possible to understand the two-phase flow phenomenon without a clear understanding of the flow patterns encountered. Flow patterns play very important roles in two-phase flow. Each regime has certain hydrodynamic characteristic, occurrence in nature and many applications in industries. The observation in the present work are illustrated in Fig. 12 by a set of photograph that show mainly the effect of inclination angle, change the air and water flow rate on the flow pattern. The observed flow patterns can be described as follows:

1. Stratified smooth flow: For low superficial air and water velocities the flow is gravity dominated, and the phases are segregated. Fig 12 (a), and (g) illustrate stratified smooth flow $v_w=1.1506\ m/s$ with two air velocity $v_g = 0.164\ m/s$, $v_g = 0.411\ m/s$, and $\theta= 5^\circ$. At the same angle, an increase of superficial velocity $v_w=1.4815\ m/s$ causes the appearance of stratified wavy flow as shown in Fig.12 (d), and (j). That was consistent with experimental work of [8]. It has been noted stratified flow was only observed when the

- pipe inclined downwards 5° . Due to the buoyancy force the gas phase tends to the flow along the upper wall of the tube than the lower wall, as the gas velocity is increased some droplets appeared at the upper wall of the test section.
- Intermittent flow: plug or slug of liquid which fill the pipe are separated by gas zones which contain liquid layer flowing along the bottom of the pipe. At low superficial velocity of air and with increase the inclination angle of test section this flow pattern was notched, Fig. 12 (b) depicts plug flow regime with bubble appeared at the top of the tube, where $v_w = 1.1506$ m/s, $v_a = 0.164$ m/s, and $\theta = 10^\circ$. The transition from plug to slug flow at higher superficial air velocity $v_a = 0.411$ m/s at the same angle $\theta = 10^\circ$ as shown in Fig. 12 (h). Slug flow was also presented at angle 15° with $v_w = 1.1506$ m/s, and $v_g = 0.164$ m/s as shown in Fig. 12 (c). This due to increase the superficial velocity of air, and the angle of downward inclination, these results confirmed with experimental results of [2].
 - Annular flow: the annular flow consists of a water film around the pipe and an air core. This flow dominated at angle 15° with superficial velocity of water and air $v_w = 1.4815$ m/s, $v_g = 0.164$ and 0.411 m/s as shown in Fig. 12 (f) and (L). Also, the annular flow regime appears at $v_w = 1.4815$ m/s with air velocity $v_g = 0.411$ m/s, and $\theta = 10^\circ$ as pointed in Fig. 12 (k). In case of smaller superficial velocities, droplets appeared at the top of the test section as can be seen in Fig. 12 (e), and (i). This is called annular bubbly flow regime. These patterns results consistent with results of [4].

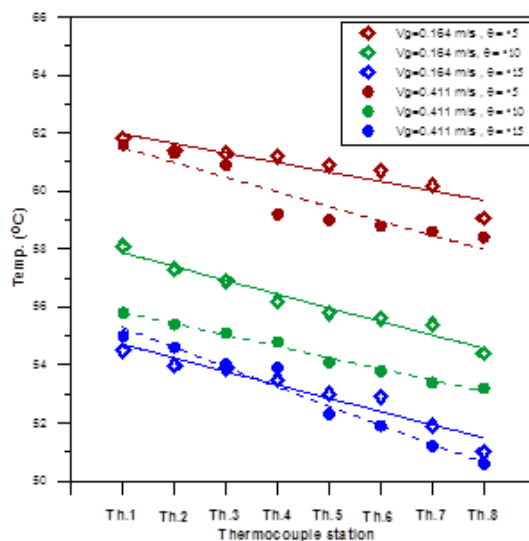


Fig. 6. Temperature reading in two phase air-water flow at $V_w = 1.1506$ m/s

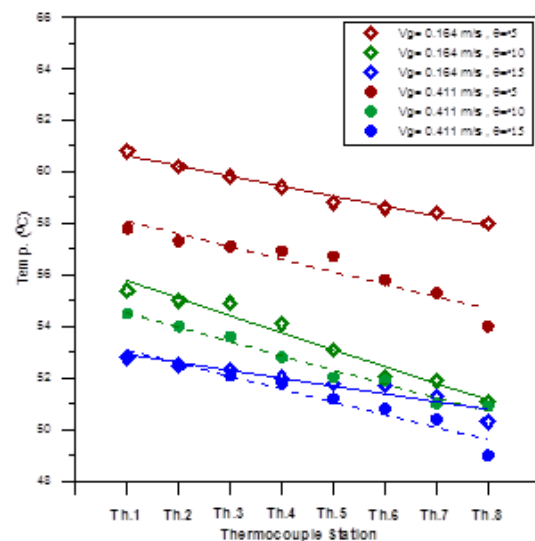


Fig. 7. Temperature reading in two phase air-water flow at $V_w = 1.4815$ m/s

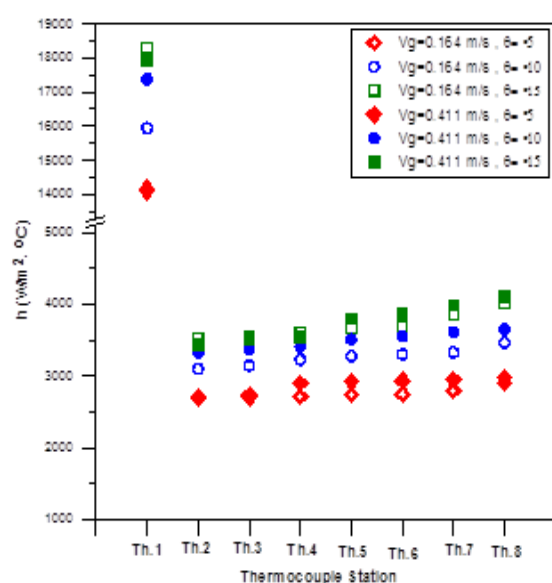


Fig. 8. Effects of inclination angle on two-phase heat transfer coefficient at $V_w=1.0 \text{ m/s}$.

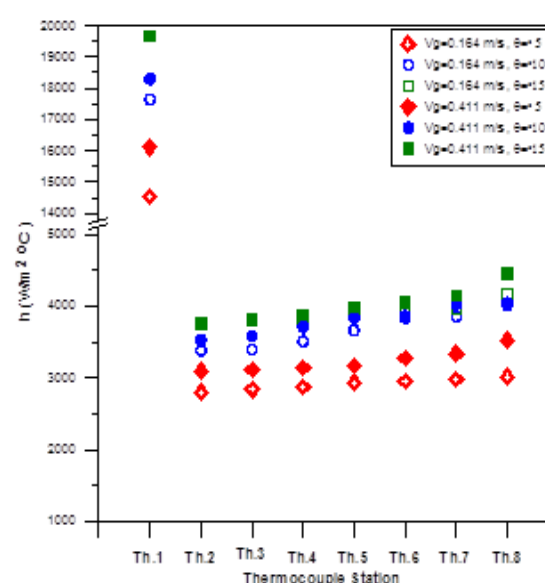


Fig. 9. Effects of inclination angle on two-phase heat transfer coefficient at $V_w=1.5 \text{ m/s}$.

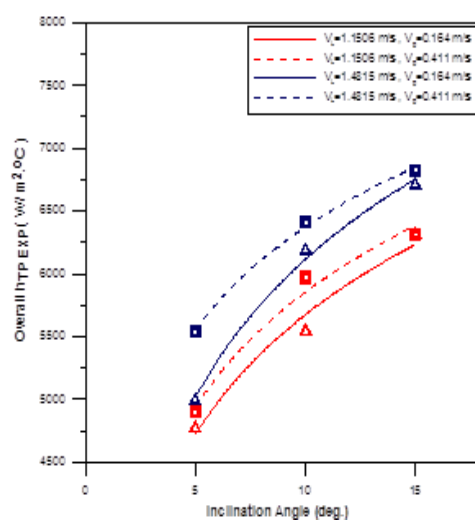


Fig. 10. Effect of inclination angle on the overall mean two-phase heat transfer coefficient

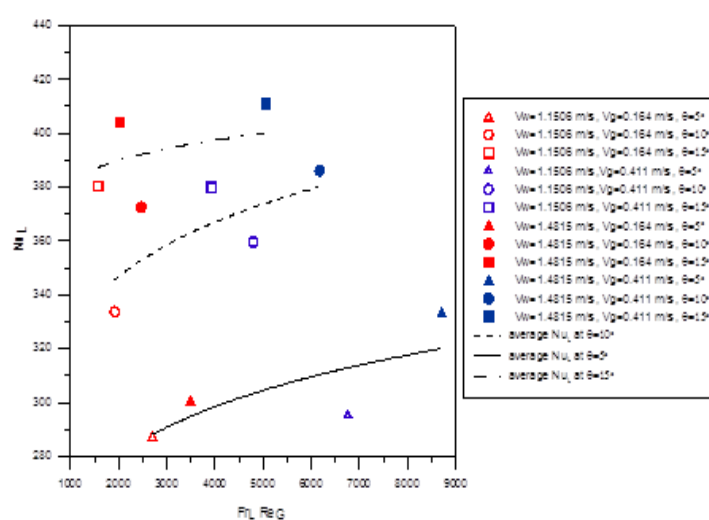
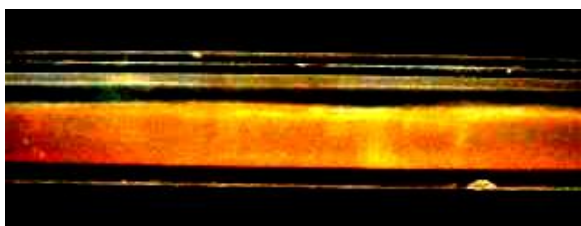
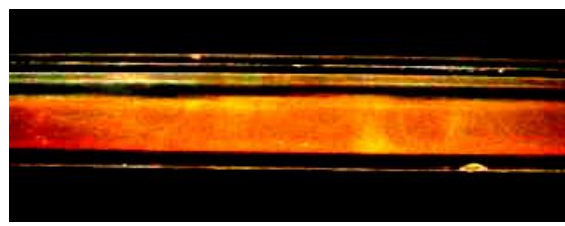


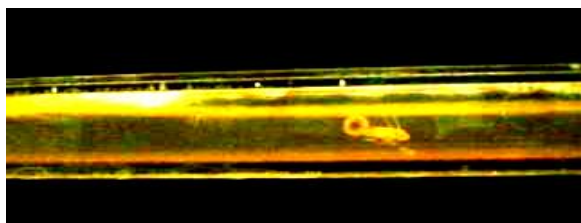
Fig. 11. Nusselt number correlation



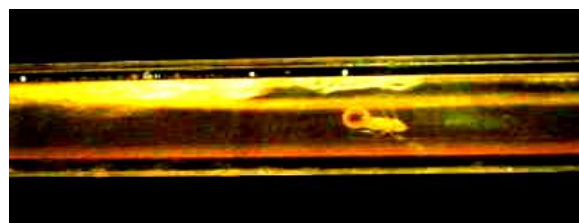
a: $v_w = 1.1506 \text{ m/s}$, $v_a = 0.164 \text{ m/s}$, $\theta = ^\circ 5$



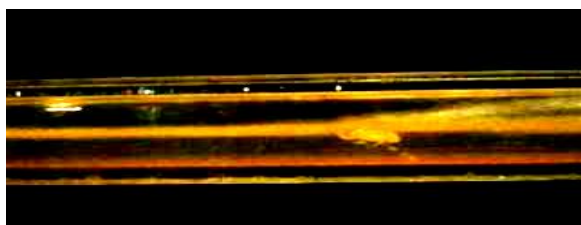
g: $v_w = 1.1506 \text{ m/s}$, $v_a = 0.411 \text{ m/s}$, $\theta = ^\circ 5$



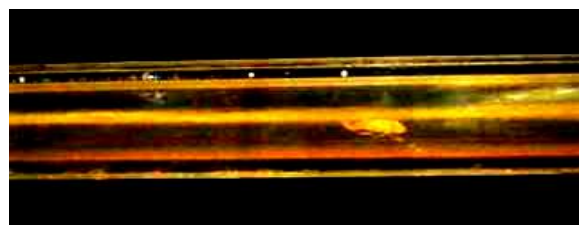
b: $v_w = 1.1506 \text{ m/s}$, $v_a = 0.164 \text{ m/s}$, $\theta = ^\circ 10$



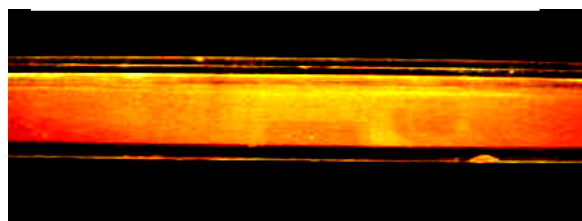
h: $v_w = 1.1506 \text{ m/s}$, $v_a = 0.411 \text{ m/s}$, $\theta = ^\circ 10$



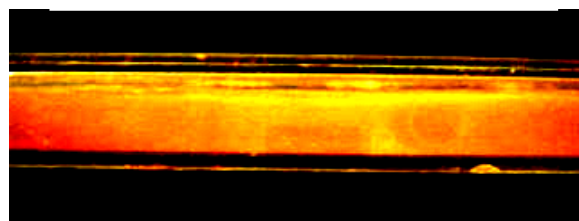
c: $v_w = 1.1506 \text{ m/s}$, $v_a = 0.164 \text{ m/s}$, $\theta = ^\circ 15$



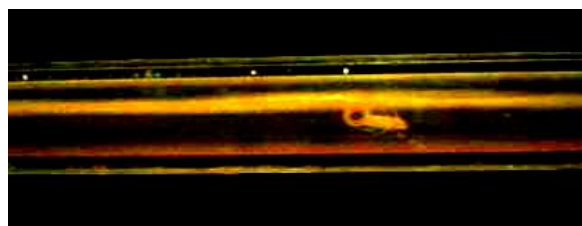
i: $v_w = 1.1506 \text{ m/s}$, $v_a = 0.411 \text{ m/s}$, $\theta = ^\circ 15$



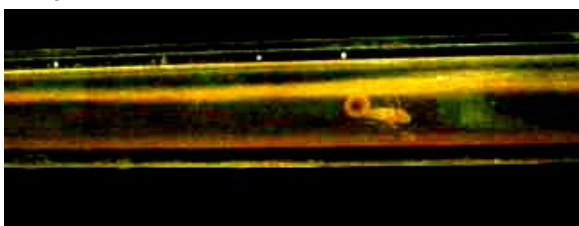
d: $v_w = 1.48156 \text{ m/s}$, $v_a = 0.164 \text{ m/s}$, $\theta = ^\circ 5$



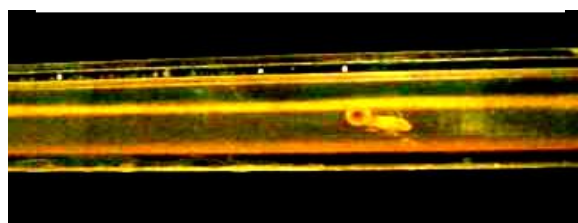
j: $v_w = 1.48156 \text{ m/s}$, $v_a = 0.411 \text{ m/s}$, $\theta = ^\circ 5$



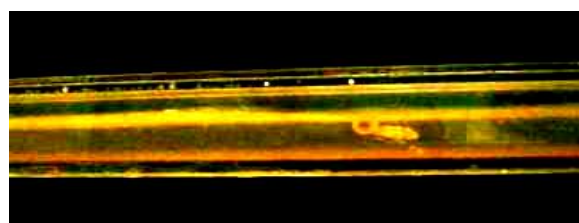
e: $v_w = 1.48156 \text{ m/s}$, $v_a = 0.164 \text{ m/s}$, $\theta = ^\circ 10$



k: $v_w = 1.48156 \text{ m/s}$, $v_a = 0.411 \text{ m/s}$, $\theta = ^\circ 10$



f: $v_w = 1.48156 \text{ m/s}$, $v_a = 0.164 \text{ m/s}$, $\theta = ^\circ 15$



L: $v_w = 1.48156 \text{ m/s}$, $v_a = 0.411 \text{ m/s}$, $\theta = ^\circ 15$

Fig. 12. Flow patterns of downward air-water flow in inclined square pipe.

4. CONCLUSIONS

Local heat transfer coefficients and flow pattern were measured for air-water in 4.5 cm, inner length of square section pipe and downward inclined 5° , 10° , and 15° positions. The water superficial velocity varied from 1.150 to 1.481 m/s and the air superficial velocity varied from 0.164 to 0.411 m/s.

1. These results showed the heat transfer coefficient increases with increasing pipe inclination angle, air and water superficial velocity.
2. Stratified flow pattern was observed in the case of inclination angle 5° as $V_w = 1.150$ m/s with two values of air velocity 0.164 and 0.411 m/s. Also, stratified wavy regime was dominated when the water superficial velocity increasing to 1.48 m/s.
3. Plug flow pattern was observed at $V_w = 1.150$ m/s and $V_a = 0.164$ m/s with inclination angle 10° .
4. The transition from plug to slug flow occurred when increasing the inclination angle to 15° at the same values of air and water velocities.
5. The transition from slug to annular flow occurred with higher superficial water velocity with increase in downward inclination angle to 15° .
6. Empirical correlations on local and average Nusselt number were developed. The results of the present study can be used to predict the wall temperature for the heat transfer to air-water flow in inclination pipe, in the range of studied superficial velocities.
7. The experimental results showed that the inclination angle, air and water velocities have significant effect on the heat transfer coefficient and flow pattern.

1. REFERENCES

- [1] Ghajar , A. J., March, 2005, " Non-Boiling Heat Transfer in Gas-Liquid Flow in Pipes – a Tutorial", J. of Braz. Soc. of Mech. Sci. & Eng., 46 Vol. XXVII, No. 1.
- [2] Kang, C., Jepson, W.P., and Wang, H., 2002, "Flow Regime Transition in Large Diameter Inclined Multiphase Pipelines", NASE International Publication Division, paper No., 02243, U.S.A.
- [3] Hetsroni , G., Mewes, D., Gurevich, M., Mosyak, A., and Rozenblit, R., 2003, "Heat transfer to two-phase flow in inclined tubes", International Journal of Multiphase Flow, Vol. 29, pp. 173-194.
- [4] Zimmerman, R., Gurevich, M., Mosyak, A., Rozenblit, R., Hetsroni, G., 2006, "Heat transfer to air-water annular flow in horizontal pipe", International Journal of Multiphase Flow, Vol. 32, pp.1-19.
- [5] Ghajar, A. J., Tang, C.C, 2007, "Heat Transfer Measurements, Flow Pattern Maps, and Flow Visualization for Non-Boiling Two-Phase Flow in Horizontal and Slightly Inclined Pipe", J. Heat Transfer Engineering, Vol. 28, No. 6.
- [6] Perez, V. H., 2007, "Gas-Liquid Two-Phase Flow in Inclined Pipes", Ph.D Thesis University of Nottingham
- [7] Malhotra, K., December 2004, "Heat Transfer Measurement of Slug Two-Phase Flow in a Horizontal and a Slightly Upward Inclined Tube", M.Sc. Thesis, Oklahoma State University.
- [8] Tzotzi, C., Bontozoglou, V., and Andritsos, N., 2011, "Effect of Fluid Properties on Flow Patterns in Two-Phase Gas-Liquid Flow in Horizontal and Downward Pipes" Ind. Eng. Chem. Res., Vol. 50. No. 2.

Recovery of Cu (II) from Model Water using Emulsion Liquid Membrane (ELM) Technique

Dr. Mohammed D. Salman

Adnan Abdul Hussain

Mechanical Engineering Department – Thi Qar University

ABSTRACT

The proper condition of the emulsion liquid membrane (ELM) technique for the recovery and concentration of copper (II) from model water is investigated. The ELM is a solution of di (2-ethylhexyl) phosphoric acid in kerosene and sorbitan monooleate Span 80 as surfactant. The extraction efficiency of the metallic ion in the ELM in batch tests is determined. The results show good extraction percentage in relatively period of time (15 minutes) under the following conditions: pH of the feed is 8; feed concentration of 500 ppm, carrier concentration of di (2-ethyl-hexyl) phosphoric acid (D2EHPA) 4% and treatment ratio (volume of external phase to volume of emulsion phase) of 2.

Key words: Emulsion, Membrane Technique, Metallic Efficiency.

الخلاصة

الظروف المثلى لتقنية الغشاء النفاذي السائل لازالة وتركيز النحاس الثنائي التكافؤ قد اختبرت في هذه الدراسة. يتكون الغشاء النفاذي السائل من محلول داي(٢- ايثايل هكسايل) حامض الفوسفوريك في النفط الابيض والمادة السطحية سوربيتون مونوليبيت (سبان ٨٠). كفاءة الاستخلاص للمعدن النحاس الثنائي التكافؤ في تقنية الغشاء النفاذي السائل باستخدام نظام دفعي قد استخدمت. اوضحت النتائج نسبة استخلاص جيدة في وقت قصير يقدر بـ (١٥) دقيقة بالظروف التالية: الدالة الحامضية (٨) ، تركيز الداخل (٥٠٠ ملغم /لتر)، تركيز الحامل (٤%) ونسبة المعاملة (٢).

INTRODUCTION

In the near future, the exhaustion of heavy metals from industry will become a more serious problem all over the world. In order to overcome the problem towards creating favorable environment, recovering the valuable metals from industrial waste effluents offers a good alternative approach. This is important in order to save precious raw materials and to protect the environment from heavy metal contamination⁽¹⁾.

There are many methods, which have been established commercially to recover metals from industrial wastes such as solvent extraction, precipitation, ion exchange, electrolysis, cementation, and membrane separation. Current technology shows that the electrochemical method for metal recovery is promising technique, but it has low plate efficiency due to waste

streams are often dilute in metals. As a result, solvent extraction of metals has been extensively used in hydrometallurgical process, however because of metal salts usually is not soluble in organic solvents, the process requires the introduction of an extractant that will combine with the metal ion to form an organic soluble species. However, the capital outlay for such equipment can be expensive, large volumes of organic extractants are required and the performance is often limited by hydrodynamic constraints such as flooding and entrainment. There is also the potential for cross-contamination of the aqueous stream with the organic solution and it is not suitable for dilute metal concentration of wastes in term of cost and equipment's ⁽²⁾.

Problems associated with polymeric membranes such as: low selectivity, low mechanical strength, low flux rates due to high diffusional resistance and short life span have restricted the use of supported liquid membrane as a potential industrial separation process. Thus, mass transfer area, efficiency and economic viability have become necessary requirements in the application of liquid membranes in any large-scale operation. Emulsion liquid membrane (ELM) developed by Li ⁽³⁾, overcome the problem encountered in achieving large mass transfer area at low cost.

The basic principle of the liquid membrane process lies basically on solute partitioning between three liquid phases as shown in figure (1); feed, membrane and receiving phases. The emulsion liquid membrane process has three phases dispersion system, which is also known as double emulsion system. This system consists of organic solution (membrane phase), stripping solution (internal phase) and dispersed phase (external phase), which is the feed or effluent to be treated ⁽⁴⁾.

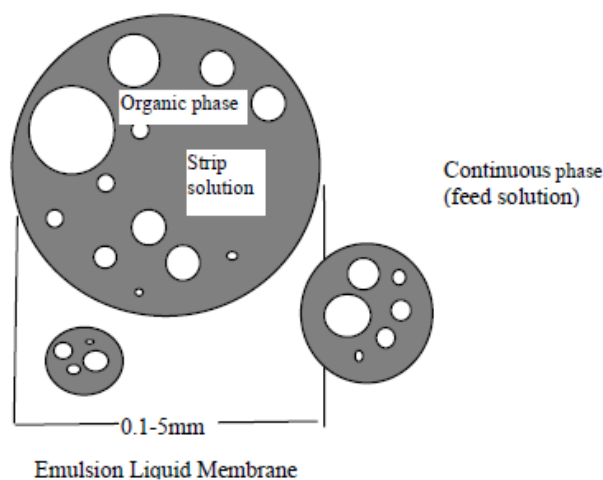


Figure (1) A Schematic Diagram of Liquid Membrane.

Emulsion liquid membrane in different formulations renders it an extremely versatile process useful for different applications. This includes waste water treatment, minerals recovery, hydrocarbon separation and a number of biochemical and biomedical applications. Due to the advantages of these membranes, several recent studies employed this technique⁽⁴⁾. Chakravarti et al.⁽⁵⁾ showed the results of Cr (VI) and Cu (II) separation with ELM from simulated wastewater solutions. They studied the effect of variation of oil membrane constituents, different concentrations of sulfuric acid as stripping in the internal phase, pH and the ion concentration in the refine, and the Cu (II) content in the wastewater. They found that the main cause of Cr (VI) transport was the ion-exchange behavior of carriers in the membrane and the coupled counter-transport resembling a “chemical pump”. They, also, found that the application of the reaction site model and involvement of a pseudo-first-order process reasonably justified the transport method of Cu (II) separation. Bourenane and El-Hadi⁽⁶⁾ presented the applicability of the Liquid Surfactant Membrane (LSM) process for the removal and the concentration of lead and cobalt. The aim of their work is to find a process for the purification of wastewater, which contains cobalt and lead. A complete study of the metal extraction by the liquid membrane process using HDEHP as extract ant and SPAN 80 as surfactant is performed in terms of extraction and stripping efficiencies, emulsion breaking and swelling. The results show that it is possible to recover 98.83% of cobalt and 94.21% of lead in the inner phase after 2 minutes of contacting time with a concentration factor of 50 for lead and 50 for cobalt. . Reis and Bart⁽⁷⁾ investigated the liquid membrane permeation of zinc in a continuous counter current column. The permeation of zinc with emulsion liquid membranes was carried out in a stirred countercurrent column. The carrier used in the membrane phase was bis (2-ethylhexyl) monothiophosphoric acid. The composition of the aqueous feed was zinc sulphate ($4.59 \times 10^{-3} \text{ kmol m}^{-3}$) and sulphuric acid. The influence of the stirring speed on zinc extraction was tested in the range of 200-320 rpm. The experimental concentration profiles of the external aqueous phase were compared with the ones predicted by numerical simulation. The mathematical model used takes into account the diffusion and reaction of solutes within the membrane and connects the hydrodynamics with mass transfer.

The goal of this paper is to study the effect of different parameters (pH of the feed, Contact Time, Feed Concentration, Carrier Concentration and Treat Ratio) on the performance of liquid membrane for recovering the copper ion from modeled water.

EXPERIMENTAL

Material Used

The mobile carrier di (2-ethyl-hexyl) phosphoric acid (D2EHPA) (Molecular Weight=322g/mole, density=1.06 g/cm³ is purchased from Fluka company. Sorbitan monooleate (Span 80) acts as non-ionic surfactant and is a product of Fluka Company. Commercial kerosene was used as diluent. Other chemical reactants such as sulfuric acid (H₂SO₄), ammonia (NH₃), sodium hydroxide (NaOH) and sodium carbonate (Na₂CO₃) were analytically graded.

Experimental Procedure

The emulsification of the organic phase and the internal phase was prepared by mixing (200 ml) of kerosene containing surfactant concentration (5% v/v) and mobile carrier concentration (1-8% v/v) with aqueous solution of internal phase (H₂SO₄, pH=1) ratio (2/1) for 15 minutes. The emulsion phase being formed was transferred to a vessel containing a known concentration of copper (500-1000 ppm) in feed solution (external phase) with treat ratio (external volume to emulsion volume) with range of (2-10) ratio. The mixture was stirred in a vessel equipped with a four bladed agitator for a given contact time. The stirrer was then, stopped and the mixture was left to settle for 5 minutes. The emulsion droplets floated to the top and the external aqueous phase and the emulsion were recovered from the extractor. Then the de-emulsification process was done by placing the emulsion between two parallel plate electrodes 16 mm part and applying an AC voltage. A schematic diagram of the equipment is as shown in Figure 2.

Samples were analyzed using atomic absorption spectrophotometer. The extraction efficiency was calculated by:

$$\%Ex = \frac{[Cu]_i - [Cu]_f}{[Cu]_i} \times 100 \quad (1)$$

Where $[Cu]_i$ and $[Cu]_f$ are initial and final concentration of copper in the aqueous phase, respectively.

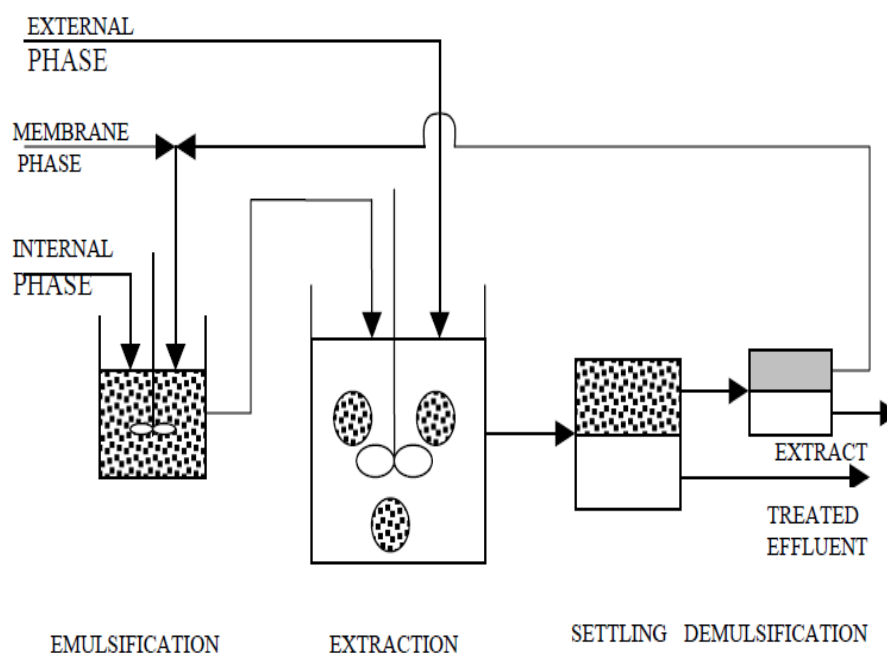


Figure (2) Schematic diagram of apparatus

RESULTS and DISCUSSIONS

2. Effect of Contact Time

Figure (3) shows the effect of contact times on extraction efficiency. As the contact time increases, the mass transfer rate of Cu increases and hence the extraction efficiency increases. With increasing contact time, the mass transfer of copper through the membrane phase increases and increasing the extraction percentage.

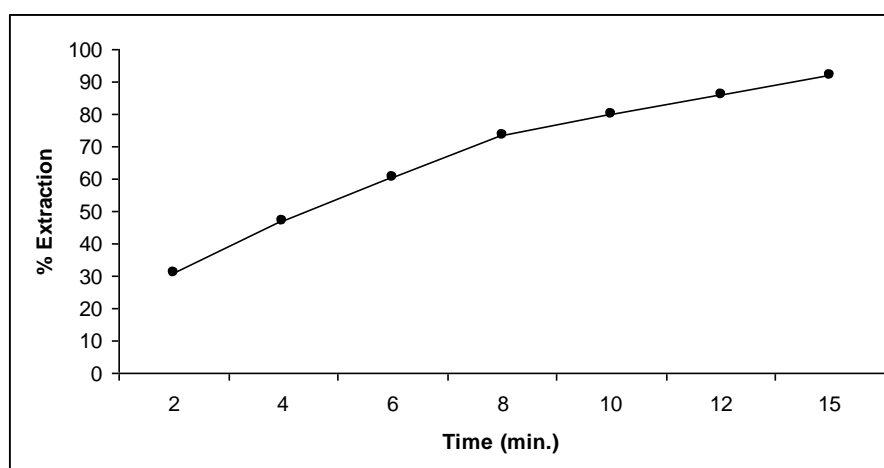


Figure (3) Effect of contact time on percent extraction operating conditions (pH = 8, feed conc. = 500ppm, carr. Conc. = 4%, treatment ratio = 2)

3. Effect of Feed Concentration

Figure (4) shows the effect of the initial copper concentration in the external aqueous phase. As can be seen that the extraction percentage decrease with increasing the concentration of copper in the feed solution. An increase in the concentration of copper the transfer resistant of the membrane increased. Also this is may be due to the emulsion breakup.

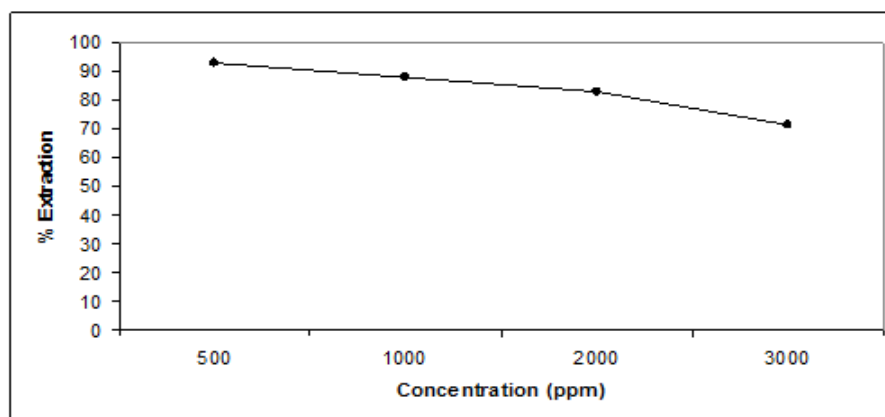


Figure (4) Effect of copper concentration in Feed on percent extraction, operating conditions (pH = 8, time = 15 min., carr. Conc. = 4%, treatment ratio = 2)

4. Effect of pH on Feed

The extraction curve obtained for copper ion solution in pH range of 3-10 is shown in figure (5); the range of pH values was adjusted with sulfuric acid. Extraction of copper metal from external phase and concentrate it in the internal phase depend on the strength of the acid/base of these phases, as can be seen that the extraction increase with decrease in acidity and it is maximum at pH=8 (base range).

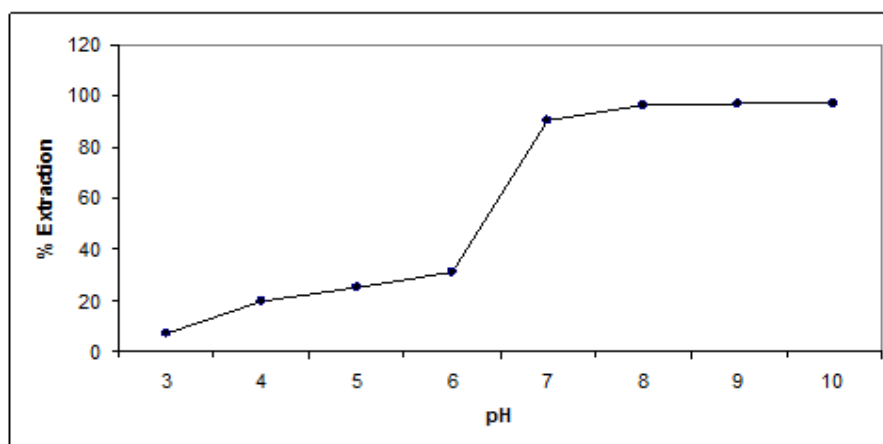


Figure (5) Effect of pH on Feed on percent extraction, operating conditions (time = 15min., feed conc. = 500ppm, carr. Conc. = 4%, treatment ratio = 2)

5. Effect of Carrier Concentration

Figure (6) shows the effect of carrier concentration in the membrane phase on extraction, it can be seen that the extraction increases until carrier concentration reaches 4%, then it decreases with increasing the concentration. This decreasing may be, due to the increase in the viscosity of the liquid membrane phase. The interfacial tension sharply decreased with increasing D2EHPA concentration. Increasing the D2EHPA concentration would not result in an improvement in the extraction of copper because the viscosities of both the membrane and emulsion have a tendency to increase for higher carrier concentrations. Larger globules would then be produced and the diffusivity of the complex would be lowered under such conditions, as is noted by A. Elsayed. From this data, it is concluded that the copper extraction is controlled by the interfacial interaction.

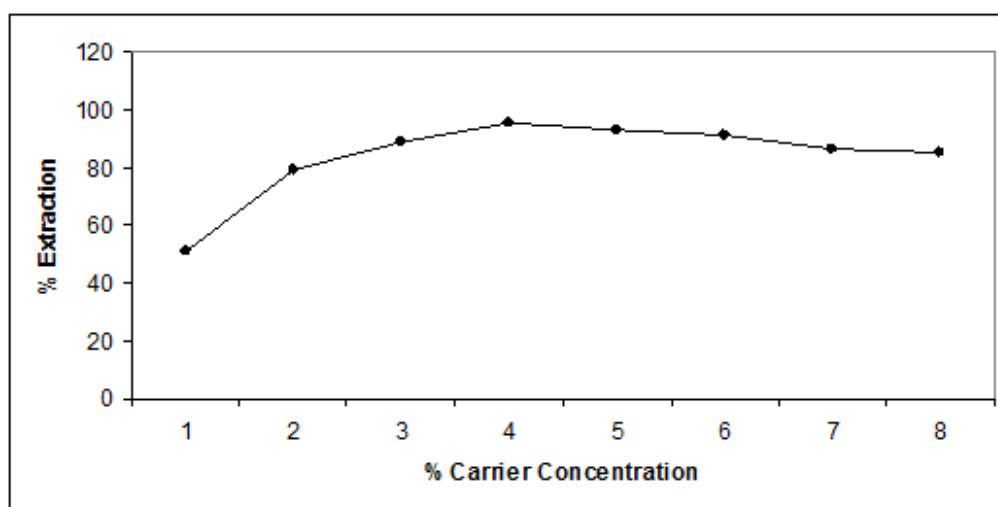


Figure (6) Effect of Carrier Concentration on percent extraction, operating conditions (pH = 8, feed conc. = 500ppm, time = 15min., treatment ratio = 2)

6. Effect of Treat Ratio

Figure (7) shows the effect of treat ratio of external volume to the emulsion volume. It can be seen that the extraction decreases slightly with increasing the ratio. This parameter controls the equipment size and chemicals used, i.e. minimize the economical cost of the process. With a decrease in the treatment ratio, the volumes of both the carrier and the stripping agent, i.e., the volume of emulsion as a whole, increased towards the external aqueous phase. Therefore, the surface area for mass transfer increased due to the formation of a larger number of emulsion globules. As a result, a higher degree of extraction was obtained. The higher treatment ratio means less emulsion is required to extract the metal ions, which is desirable from a processing point of view to ensure maximum enrichment with respect to the feed phase.

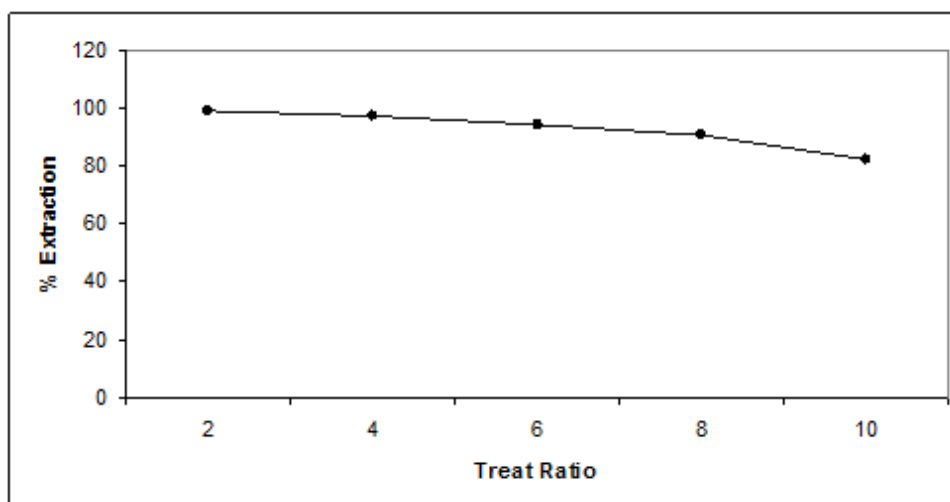


Figure (7) Effect of Treat Ratio ($V_{\text{external}}/V_{\text{emulsion}}$) on percent extraction, operating conditions (pH = 8, feed conc. = 500ppm, carr. Conc. = 4%, time = 15min.)

CONCLUSION

In this research application of emulsion liquid membrane to copper separation is studied. It was concluded that the best conditions for metal extraction are carried at pH equals (8) with contact time (15 min.), the best carrier concentration is (4%) and (2) for external to emulsion volumes ratio.

REFERENCES

- 1- Kentish S.E., Stevens G.W. (2001), "Innovations in Separation Technology for the recycling and re-use of Liquid waste Streams, Chem. Eng. J., 84, 149.
- 2- Draxler, J.fuerst W. (1988)" Sparation of Metal Species by Emulsion Liquid, J.Memb. Sci. 3,281-293.
- 3- Li, N.N and Long, R.B, (Oct.3, 1972) "Liquid membrane separation process" U.S.Pat. , 3 696 028.
- 4- Marchese J., Compderros M. (1995) "Transport and separation of Cobalt, Nickel and Copper Ions with Alamine Liquid membranes, J. Chem. Biotechnol., Vol.64, PP 293-297.
- 5- Chakravarti A.K., Chowdhury B., Mukherjee D. (1995) "Liquid Membrane multiple Emulsion Process of chromium (VI) Separation from Waste Waters, Physiochem. Eng. Vol. 103, PP 59-71.
- 6- Bourenane, S. and EL-hadi, M., (2002),"Extraction of cobalt and lead from waste water using a liquid surfactant membrane", internet connection, E-mail: samarmh@yahoo.fr.
- 7- ReisH.-J. Bart, (2004), "Liquid membrane permeation of zinc in a continuous countercurrent column", Internate connection, www.uni.kl.de/lS-Bart/bart.com.
- 8- A. Elsayed , (2008) "Zinc and Copper Separation through an Emulsion Liquid Membrane Containing Di-(2-Ethylhexyl) Phosphoric A) cid as a Carrier" chem. Eng. Tech. Vol 31, No. 103, PP 370-376.
- 9- B. Sengupta, R. Sengupta, N. Subrahmanyam, "Process intensification of copper extraction using (ELM) experimental search for optimum conditions" Hydrometallurgy 2006, 84 (1/2), 43.

Experimental and Computational Investigation of Dynamics Effects in a High Speed Centrifugal Pump

Khudheyer S. Mushatet

College of Engineering

Thiqar University

Khudheyer2004@yahoo

Abdul Kareem A. Wahab

College of Engineering

Babylon University

kareemwahab@yahoo.com

Wissam H. Ajeel

lecturer

wissam_ajeel@yahoo.com

Abstract: - Experimental and numerical investigation of a high speed centrifugal pump has been carried out. In experimental work, a test rig which includes a centrifugal pump, fast response piezoelectric pressure transducers, Rota meter flow and measurement instrumentations is designed and constructed. Two impellers having different outlet diameters were examined for the same volute. A data acquisition system (hardware) and its software (Visual Basic language) have been developed to analyze the pressure transducer signal in order to obtain the pressure fluctuations. The governing partial differential equations (continuity, momentum) besides to turbulence model are discretized to algebraic equations by using finite volume method. The solution of these equations was done by using FLUENT 6.3 commercial code. This code has the ability to use a grid generation technique and transform the physical domain to a computational domain by using GAMBIT 2.2.3 software. The effect of turbulence was simulated by using a standard $k-\varepsilon$ model. The wall function laws are used to remedy the regions near the rotating and volute walls. The effect of angular position of impeller and impeller's diameter on the flow behavior is studied for different values of volume flow rate. The obtained results show that the pressure fluctuations registered in the volute were found to be very dependent on both angular position and volume flow rate. It is observed that the pressure fluctuations have maximum values at volume flow rate ($Q=0.5Q_N$) for the considered two impellers at angular position ($\phi=270^\circ$). These values increase as impeller diameter increases. The results also show that the higher static pressure values are observed upstream of the leading edge at the volute tongue (stagnation point) while the minimum was found at impellers eye. A comparison between experimental and numerical results is done and the agreement was acceptable.

Key words: Centrifugal pump, impeller volute interaction, shrouded impeller

المستخلص: تم اجراء دراسة عملية وعددية لسلوك الجريان والتغير غير المستقر للضغط في المجمع الحلزوني لمضخة الطرد المركزي ذات السرعة العالية. في الدراسة العملية تم انشاء وتصنيع منظومة اختبار تحتوي على متحسسات الضغط وادوات قياس معدل الجريان. استخدمت منظومة معالجة الاشارة لحساب اشارات تذبذب الضغط واجريت الاختبارات على دافعتين وبأقطار مختلفة $D_2=124\text{mm}$, $D_2=132\text{mm}$. تم معالجة الاشارات الكهربائية الخارجة من متحسسات الضغط عن طريق منظومة معالجة الاشارة (Data acquisition and logging interface) من اجل الحصول على اشارات تذبذب الضغط داخل المجمع الحلزوني لمضخة الطرد المركزي. في الدراسة تم تحويل المعادلات التفاضلية الحاكمة الى معادلات جبرية باستخدام طريقة الحجم المحددة وتم حل هذه المعادلات باستخدام برنامج (FLUENT 6.3) والذي لديه القابلية لاستخدام تقنية التحويل الشبكي وتحويل المجال الفيزيائي الى المجال الحسابي باستخدام برنامج GAMBIT 2.2.3. تم معالجة تأثير الاضطراب باستخدام نموذج الاضطراب $k-\epsilon$ بينما استخدمت قوانين دالة الجدار لمعالجة المناطق القريبة من جدران الدافعة والمجمع الحلزوني. تم دراسة تأثير البعد الزاوي وقطر الدافعة على سلوك الجريان ولقيم مختلفة من معدل الجريان. أوضحت النتائج التي تم الحصول عليها أن تذبذبات الضغط المسجلة تعتمد بصورة كبيرة على قطر الدافعة والموقع الزاوي للدافعة ومعدلات التدفق الحجمي للجريان حيث تصل الى اقصى قيمة عند معدل التدفق الحجمي $(Q=0.5Q_N)$ والموقع الزاوي $(\varphi = 270^\circ)$ علما ان هذه القيم تزداد مع زيادة قطر الدافعة. بينت النتائج ايضا ان هناك زيادة في قيم الضغط بعد مغادرة المائع منطقة القطع (stagnation point) وأن قيم الضغط الاستاتيكي تقل عند مركز الدافعة. أجريت مقارنة بين النتائج العملية والنتائج النظرية واعطت المقارنة توافقا مقبولا.

1. Introduction

The analysis of flow dynamics in a centrifugal pump is considered a very complex due to presence of system rotation, separation, turbulence and secondary flows. A pump is a machine which is called by this name due to a centrifugal force imposing on a liquid. The liquid attains its velocity and pressure when passing through impeller and this liquid is then decelerates at impeller. The centrifugal pump is widely separated in diverse technological applications. Many studies were done on investigating the flow dynamics and performance centrifugal pump. A particle Doppler velocimetry (PDV) technique was used by Dong et al.[1] to analyze the flow inside the volute of centrifugal pump. A particles $30\mu m$ used as seed. The obtained results showed that the entire flux pulsating within the value reached the maximum when the blade lines up with the tip of the tongue. Moreover, they observed that although most of the blade effects occur near the impeller tip, they are not limited to this region. The velocity distribution corresponding to design and off-design operation was studied by Elholm et al. [2]. LDV method was used to obtain the velocity distribution. They observed that the swirl has a forced vortex type velocity distribution and the location of its center was altered with mass flow rate.

Also it was found the circumferential curvature of the volute was responsible for a radial gradient of the flow velocity. Leakage flows in the tongue region was found to have a significant impact on position of the swirl center. Van Esch[2] performed an experimental study on the effect of a mixed-flow pump and hydrodynamic forces on the impeller. The obtained result show that the influence of the suction flow profile and blade interaction on pump performance and forces. Chu et al. [3] considered a particle image velocimetry complemented with noise and pressure measurements to measure the velocity distribution and compute the unsteady pressure field in the near-tongue region of the volute of a centrifugal pump. The concluded that the primary sources in noise generation were associated with the interaction of the non uniform out flux from the impeller (jet-wake phenomenon) with the tongue. Timushev and Ovsyannikov [4] performed the numerical techniques of pressure fluctuation amplitude estimation at blade frequencies in the volute casing passage of the centrifugal pump. Their results showed that the sources of hydrodynamic nature bring about considerable vibrations and noise of centrifugal pumps .A finite element technique was adopted by kaps [5] to study unsteady turbulent flow in centrifugal pumps. The conducted results showed that the strong influence of the casing tongue on the flow conditions was near the trailing edge and vice versa while the trailing edge was near to the tongue. Qin and Tsukamoto [6] studied the unsteady flow induced by the interaction between impeller blades and diffuser vanes volute casing in a diffuser pump. The unsteady flow in the diffuser vane passage, as well as the volute casing, was assumed to be induced by the five kinds of singularities—the bound vortices distributed on the impeller blades. They analysed the unsteady pressure downstream of the impeller for a variety of parameters by using the singularity method incorporated the effect of volute casing. The pressure fluctuations due to interaction between impeller and diffuser vanes was studied numerically by Wang and Tsukamoto [7].They found that the potential effect of the wake effect on the pressure fluctuations can be predicted satisfactorily by the present vortex method whereas the pressure fluctuations near the diffuser inlet were affected by the potential interaction, the pressure fluctuations near the outlet were predominantly affected by the wake effects due to wake transport. Shi and Tsukamoto [8] made a numerical study for the prediction of pressure fluctuations caused by impeller–diffuser interaction in a vaned centrifugal pump and they concluded that impeller–diffuser interaction was caused chiefly by potential interaction and wake impingement with the diffuser vanes. Dong et al. [9] used PDV technique to visualize the flow inside the volute of a centrifugal pump.

They verified that the entire flux pulsating within the volute reaches a maximum when the blade lines up with the tip of the tongue. Ozturk et al. [10] investigated the flow behavior in a non- traditional centrifugal pump, whose diffuser was subjected to different radial gaps using multi- purpose fluent code. They found that the Performance curve for centrifugal pumps shows a good approximation with experimental results under fluent solver. The three dimensional turbulent flow was investigated numerically by Silva et al. [11]. They found that an attempt to model an industrial centrifugal pump as a bench-mark test case. Many numerical studies such as Aarts a Jonker [12], Seldar [13], Sano et al. [14] and Sano et al. [15] were performed to predict the velocity distribution and pressure fluctuations through the centrifugal pump.

In the present work, an experimental and computational study was done to investigate the dynamics effects arise due to impeller-volute interaction in a shrouded logarithmic profile high speed centrifugal pump. The test rig was designed and constructed to get the pump performance and the mentioned dynamic effects while the computations were done by using a Fluent 6.2. Commercial code. Two impellers having different outlet diameters were examined for the same volute. Modern high response pressure transducers along with a data acquisition system were used to obtain the pressure fluctuations at multiple points on the centrifugal pump volute. The volume flow rate values were ranged from 0.5QN to 1.5QN. To the knowledge of the authors, there is no many studies has been cited on a high speed centrifugal pump of logarithmic profile. So the present work extends the related research area through documentation of experimental and numerical results to obtain a good understanding of the flow mechanism for this type of centrifugal pumps. The description of physical problem is shown in Fig.1. The objective of the present study is to cover the following:

1. The variation of static, dynamic pressure and unsteady flow effects inside a centrifugal pump due to impeller-volute interaction is to be experimentally and numerically investigated.
2. Constructing an experimental test rig by using modern measurement instrumentations.
3. Using data acquisition techniques to process the pressure fluctuating signals.
4. The Comparison between numerical and experimental results is to be conducted.

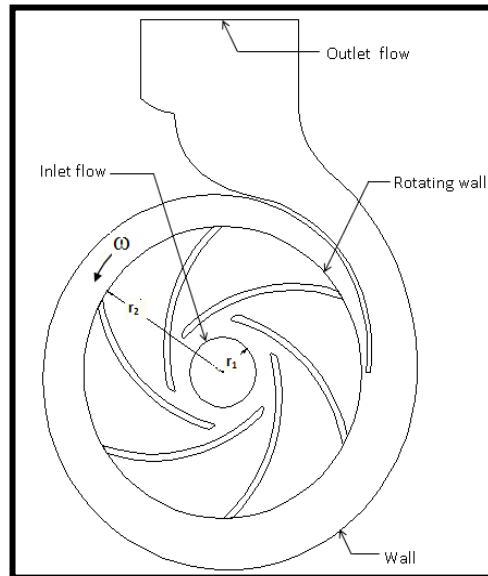


Fig.1 Schematic diagram of the considered problem.

2. Theoretical Work

2.1 Model description.

The physical model considered in this study is shown in Fig.1 which represents a centrifugal pump having a single axial suction and vane- less volute casing, equipped with an impeller of 132mm in outside diameter and six backwards curved blades. The liquid particles enter into the impeller via a cylindrical surface of radius r_1 with an absolute velocity V_1 and exit the impeller via a cylindrical surface of radius r_2 with an absolute velocity of V_2 and inclined at angle α_2 to the peripheral velocity U_2 . The flow patterns at inlet and exit of an impeller rotating with a constant angular velocity which is defined by the velocity triangle as shown in Fig.2. It is assumed that the flow at impeller is irrotational ($\alpha_1 = 90^\circ$).

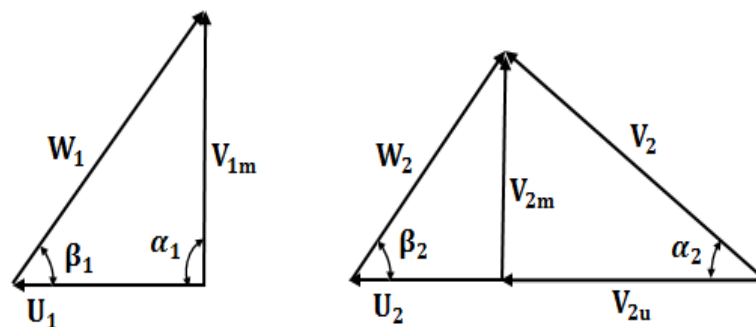


Fig.2. velocity triangles at the impeller inlet and outlet

2.2 Mathematical Model and Numerical simulation.

To simplify the proposed model, the following assumptions are conducted.

- 1- The fluid has constant properties.
- 2- Two dimensional flows.
- 3- Steady state flow.
- 4- Incompressible flow.
- 5- Non-slip flow is assumed.

The governing equations of fluid flow for a steadily rotating frame can be written as follows [14]:

Conservation of mass:

$$\frac{\partial \rho}{\partial t} + \nabla \cdot \rho \vec{v}_r = 0 \quad \text{..... (3.1)}$$

Conservation of momentum:

$$\frac{\partial}{\partial t}(\rho \vec{v}_r) + \nabla \cdot (\rho \vec{v}_r \vec{v}_r) + \rho(2\vec{\omega} \times \vec{v}_r + \vec{\omega} \times \vec{\omega} \times \vec{r}) = -\nabla p + \nabla \bar{\tau}_r + \vec{F} \quad \text{..... (3.2)}$$

$$\bar{\tau}_r = \mu \left[(\nabla \vec{v}_r + \nabla \vec{v}_r^T) - \frac{2}{3} \nabla \cdot \vec{v}_r I \right] \quad \text{..... (3.3)}$$

The effect of turbulence was modeled by using a k-ε model which describes two equations, one for turbulence energy and the other for the dissipation of turbulence energy.

$$\frac{\partial}{\partial t}(\rho k) + \frac{\partial}{\partial x_i}(\rho k u_i) = \frac{\partial}{\partial x_j} \left[\left(\mu + \frac{\mu_t}{\sigma_k} \right) \frac{\partial k}{\partial x_j} \right] + G_k - \rho \epsilon \quad \text{..... (3.4)}$$

$$\frac{\partial}{\partial t}(\rho \epsilon) + \frac{\partial}{\partial x_i}(\rho \epsilon u_i) = \frac{\partial}{\partial x_j} \left[\left(\mu + \frac{\mu_t}{\sigma_\epsilon} \right) \frac{\partial \epsilon}{\partial x_j} \right] + C_{1\epsilon} \frac{\epsilon}{k} G_k - C_{2\epsilon} \rho \frac{\epsilon^2}{k} \quad \text{..... (3.5)}$$

The turbulent (or eddy) viscosity, μ_t , is computed by combining k and ϵ as follows:

$$\mu_t = \rho C_\mu \frac{k^2}{\epsilon} \quad \text{..... (3.6)}$$

The model constant $C_{1\epsilon}$, $C_{2\epsilon}$, C_μ , σ_k and σ_ϵ have the following default values [40]:

$$C_{1\epsilon} = 1.44, C_{2\epsilon} = 1.92, C_\mu = 0.09, \sigma_k = 1.0, \sigma_\epsilon = 1.3$$

2.2.1 Boundary Conditions

The physical understanding of turbomachinery flow made assigning the design conditions for the present research. Steady uniform axial velocity is imposed at inlet while a constant static pressure is maintained at outlet. The flow rate was changed by modeling the static pressure at exit to kinetic energy by monitoring closing positions of the valve. The considered boundary conditions for the flow can be mentioned as follows:

For impeller A ($D_2=132$ mm):

- 1- For flow rate ($Q=0.5Q_N$), the static pressure at outlet ($P_{\text{outlet}}=200000$ pa).
- 2- For flow rate ($Q=0.7Q_N$), the static pressure at outlet ($P_{\text{outlet}}=180000$ pa).
- 3- For flow rate ($Q=Q_N$), the static pressure at outlet ($P_{\text{outlet}}=140000$ pa).
- 4- For flow rate ($Q=1.3Q_N$), the static pressure at outlet ($P_{\text{outlet}}=130000$ pa).
- 5- For flow rate ($Q=1.5Q_N$), the static pressure at outlet ($P_{\text{outlet}}=120000$ pa).

For impeller B ($D_2=124$ mm)

- 1- For flow rate ($Q=0.5Q_N$), the static pressure at outlet ($P_{\text{outlet}}=190000$ pa).
- 2- For flow rate ($Q=0.7Q_N$), the static pressure at outlet ($P_{\text{outlet}}=170000$ pa).
- 3- For flow rate ($Q=Q_N$), the static pressure at outlet ($P_{\text{outlet}}=130000$ pa).
- 4- For flow rate ($Q=1.3Q_N$), the static pressure at outlet ($P_{\text{outlet}}=120000$ pa).
- 5- For flow rate ($Q=1.5Q_N$), the static pressure at outlet ($P_{\text{outlet}}=110000$ pa).

Fluent 6.2 commercial codes were used to simulate the discretized governing equations. The discretization of the governing equations was done by using finite volume method with sliding mesh techniques. Creating the required computations mesh for the considered problem was done by using GAMBIT2.3. This facility gives different types of meshes such as hexahedral and tetrahedral and the mesh may be structured or non-structured. To ensure that the computed flow field is not affected by changing the mesh, different numbers of cells were used. It was found that any increase above 60940 will not affect the trend of the predicted mass flow rate at outlet as depicted in Fig.3.

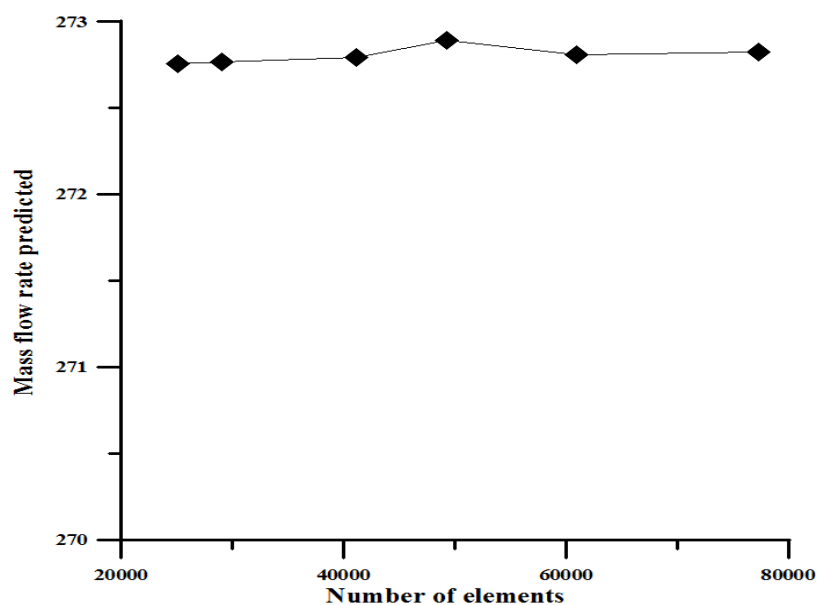


Fig. 3. Mass flow rate versus number of element

The computational mesh created by GAMBIT is shown in Fig.4. The calculations of Fluent were performed for convergence criteria less or equal 1×10^{-5} .

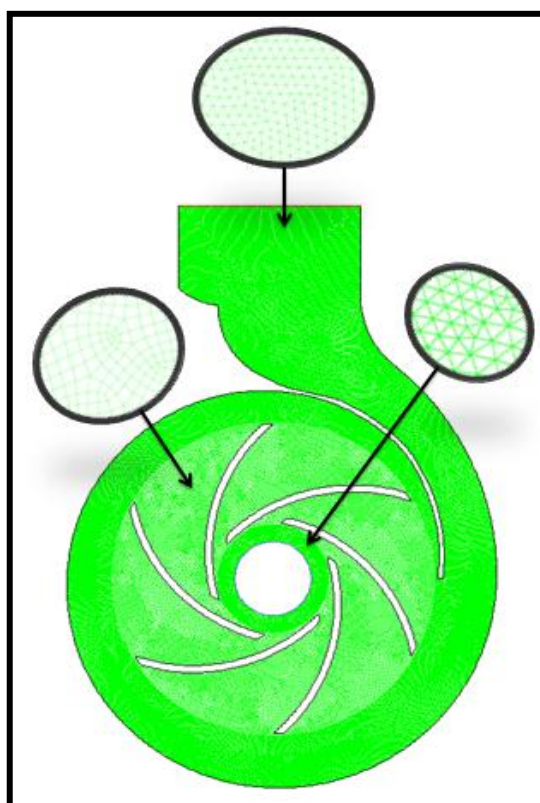


Fig. 4. Mesh used for centrifugal pump with 132 mm impeller

3. Experimental work

A test rig shown in Fig.2 has been designed and constructed to be suitable for the purpose of present and future research. The test pump is a single stage centrifugal pump with shrouded impeller and volute. The test rig consisted of a constant-speed electric pump, a throttle valve, a rotameter flow, and piping. The outlet pipe of the pump is connected to a water flow meter through 45 cm length pipe. The throttle valve (gate valve), fitted on the discharge side of the piping which allows an accurate and fine control of the volume flow rate. The pump is directly driven by a motor single phase 1.5 kW, 220 V AC which has a constant rotational speed of 2900 rpm. Two impeller (A and B) with different outlet diameters were considered. The blades of these impellers were of backward shape having a thickness of 3mm. The number of blades of impeller is six. The details of the impeller technical data are shown in table 1. The measurements for the present study are carried out on the volute of the pump (shrouded side). Four pressure transducers were located (one each 90 deg) on circumference with $R=71\text{mm}$. The location of the tongue of the volute is 270° after the first transducer as. Figure 5 shows the schematic diagram of the experimental test rig.

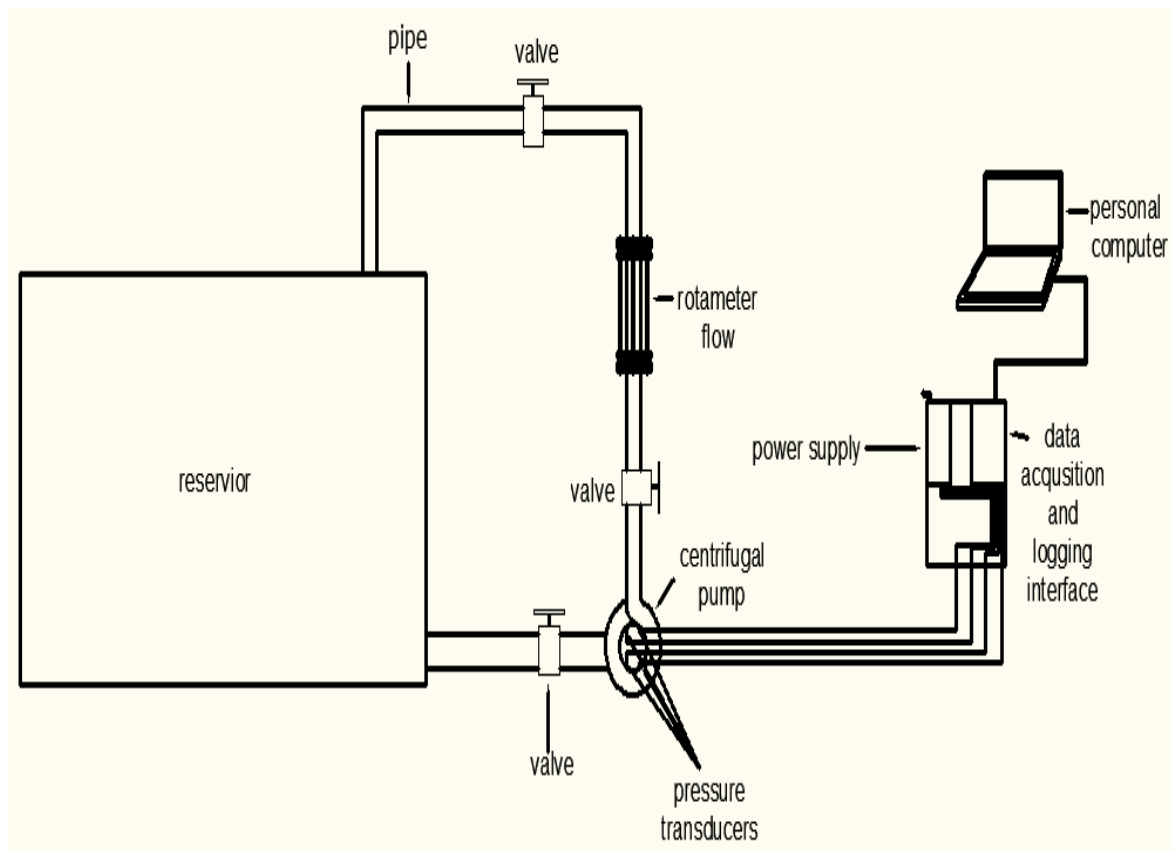


Fig. 5. Schematic diagram of the Experimental test rig

Table1. Pump technical data

Impeller exit diameter	Impeller A, $D_2=132\text{mm}$ Impeller B, $D_2=124\text{mm}$
Impeller inlet diameter	$D_1=48\text{mm}$
Number of impeller blades	$Z=6$
Speed	$N=2900\text{ rpm}$
Inlet blade angle	$\beta_1=15^\circ$
outlet blade angle	$\beta_2=20^\circ$
Blade thickness	$t=3\text{mm}$
Inlet blade width	$b_1=15\text{mm}$
Outlet blade width	$b_2=9\text{mm}$
The gap between the tongue and the impeller	Impeller A=2mm Impeller B=6mm

4. Results and Discussion.

Computational and experimental study for predicting the performance and the hydrodynamic parameters of high speed centrifugal pump has been performed. The discussion of the present results has been divided into two sections.

4.1 Analysis of Numerical Results

The obtained numerical results covered the distribution of static pressure, dynamic pressure, velocities, and turbulent kinetic energy. The results of dynamic pressure are not included here because of the limited available space.

Figs.6-7 show the contours of static pressure distribution for impeller A and impeller B at $Q=0.5Q_N$. It is observed that the static pressure has a minimum value at impeller eye and increases as angular position increases. The maximum values of pressure are recorded down stream the leading edge of volute tongue (stagnation point). The same trend of pressure was in the channels of the two impellers (A &B). At exit of the two impellers, there is obvious increase in the values of pressure distribution. As the figure show, when the impeller diameter increases, the values of pressure decreases.

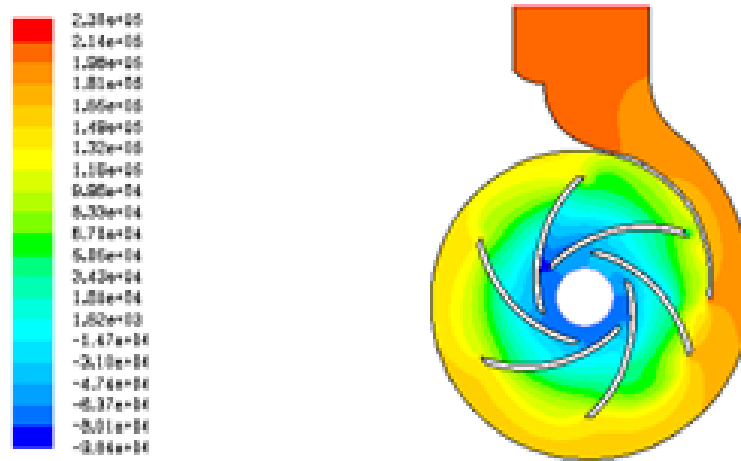


Fig.6 Contours of static pressure distribution (Pascal) for
impeller A at $Q=0.5Q_N$.

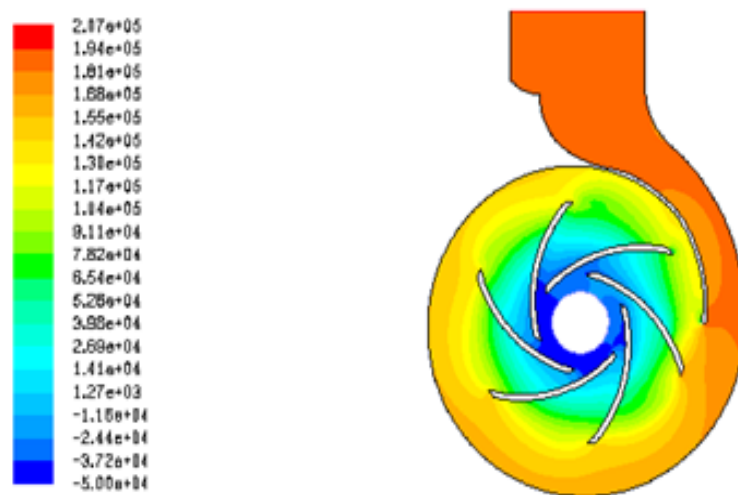


Fig.7 Contours of static pressure distribution (Pascal) for
impeller B at $Q=0.5Q_N$.

The design operating condition ($Q=Q_N$) is demonstrated through Figs.8-9. For the two impellers (A&B). It can be observed that the pressure values increase gradually along the blade passage. It is expected that the pressure trend in the impeller is equal that in the volute. The pressure trend seems to be uniform for this design condition ($Q=Q_N$) but this behavior is changed as flow rates increase or decrease. The pressure trend is changed significantly when the flow rate increases to $Q= 1.5 Q_N$ as shown in Figs10-11. The large or minimum values of pressure distribution are shifted about the previous positions. A high pressure values were recorded in the tongue zone and these are larger in impeller A compared with impeller B.

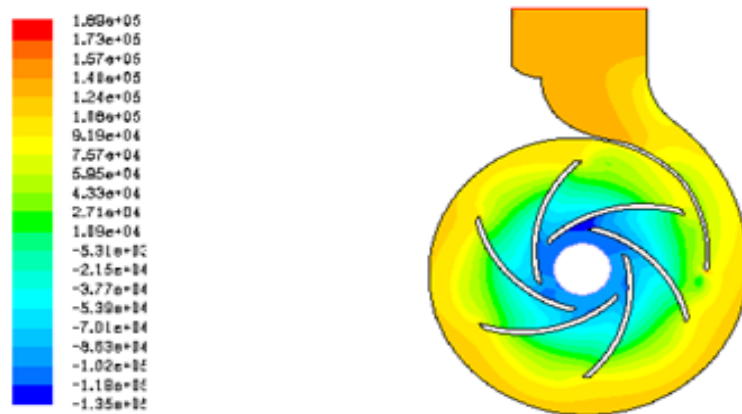


Fig.8 Contours of static pressure distribution (Pascal) for impeller A at $Q=Q_N$.

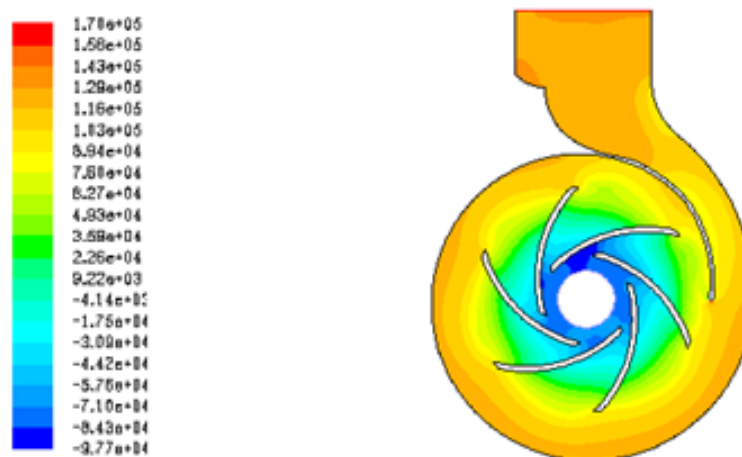


Fig. 9 Contours of static pressure distribution (Pascal) for impeller B at $Q=Q_N$.

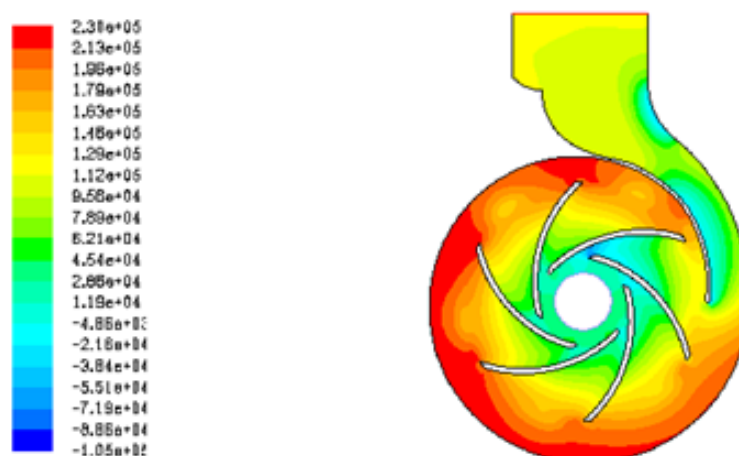


Fig.10 Contours of static pressure distribution (Pascal) for impeller A at $Q=1.5Q_N$.

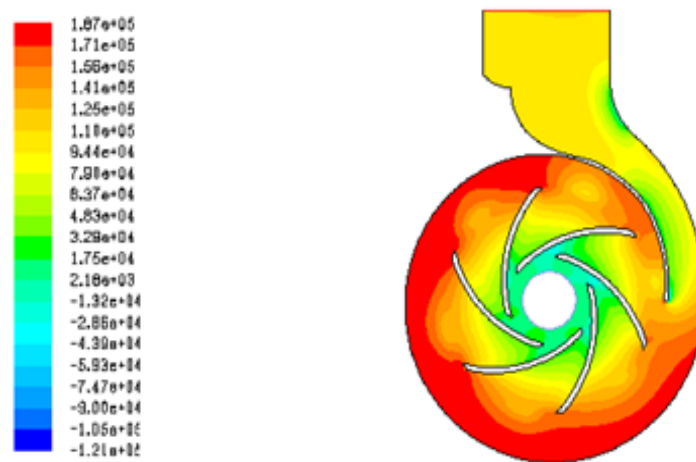


Fig.11 Contours of static pressure distribution (Pascal) for impeller B at $Q=1.5Q_N$.

The contours of absolute velocity for the considered two impellers and for different flow rates are shown in Figs. 12-13. It is observed that there is a recirculation region for all the studied volume flow rates. However the position of these regions is changed as volume flow rate changes. At $Q=0.5Q_N$, low values of velocity distribution is observed at discharge pipe and this increases as impeller diameter increases.

At $Q=Q_N$, the change in velocity becomes less and the velocity increases in the discharge pipe and the distribution of the recirculation regions and the maximum and minimum values of velocity seems to be matching in the impeller and volute. However this trend is reflected at high volume flow rates ($Q= 1.5 Q_N$) where the large amount of the flow is pushed towards the outlet duct. As a result, the stagnation point on the tongue is moved to impeller side and there is a wake on exit of the tongue.

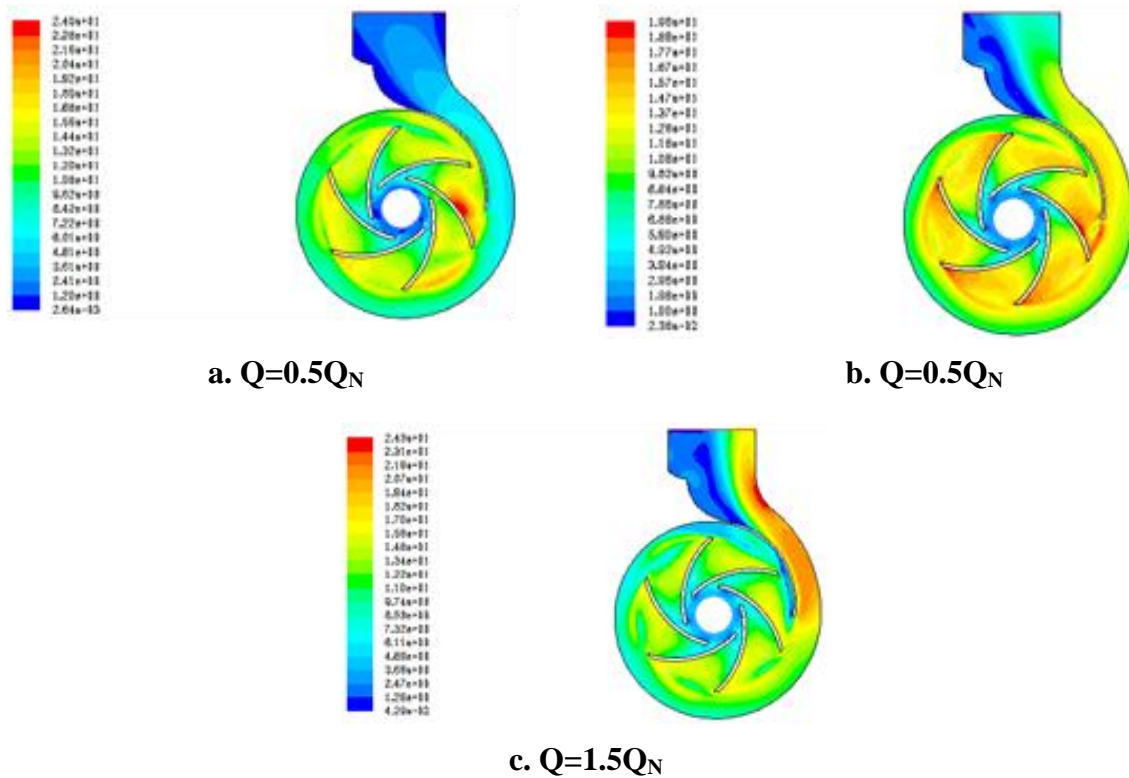


Fig.12 Contours of absolute velocity distribution (m/s) for impeller A.

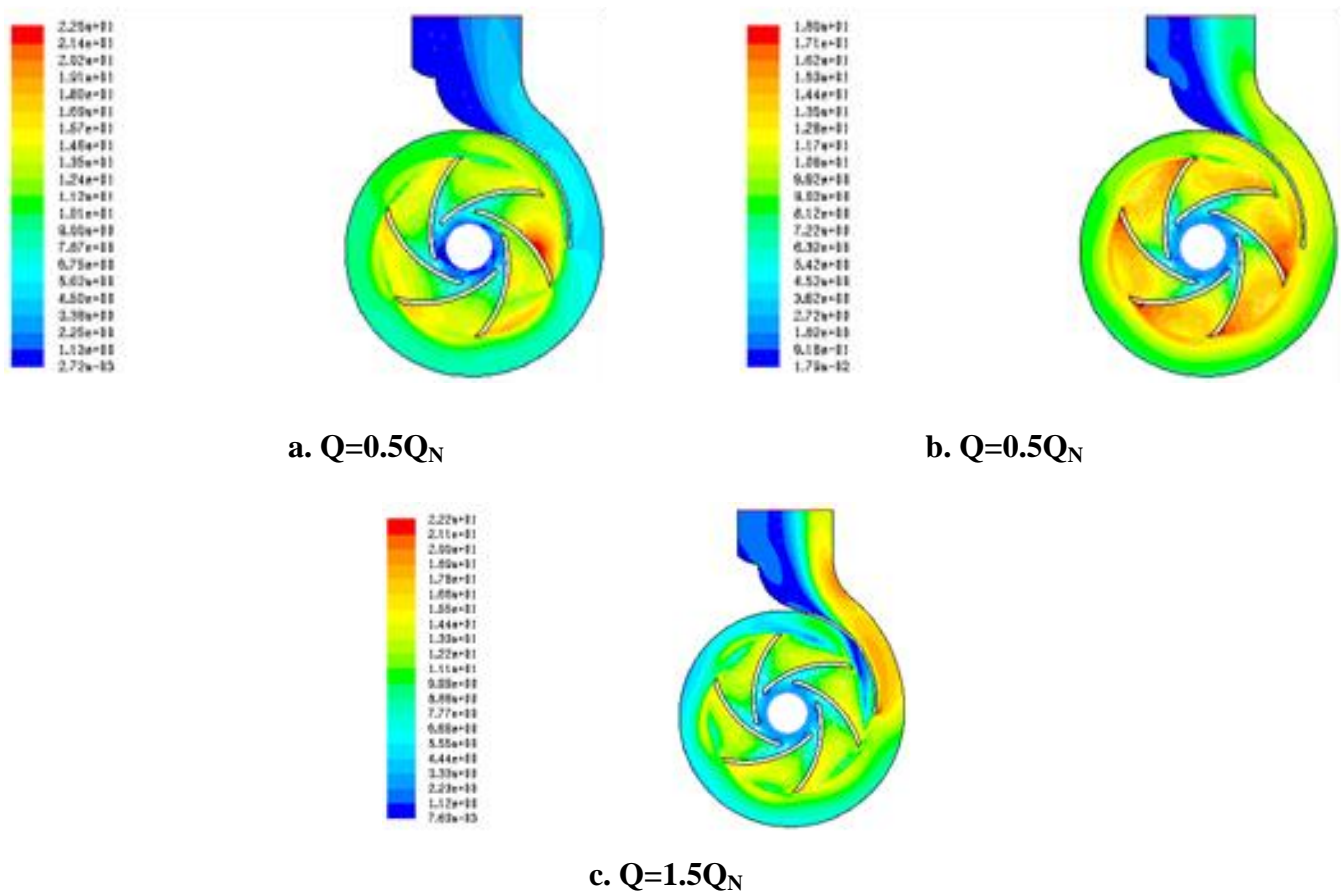


Fig.13 Contours of absolute velocity distribution (m/s) for impeller B.

Figs.14-15 shows the distribution of turbulent kinetic energy for the two considered impellers (A&B) and for different values of volume flow rates. It can be observed that the maximum values of turbulent kinetic energy are found at trailing edge of impeller blades for the mentioned cases. The values of turbulent kinetic energy are decreased as impeller diameter decreases. At nominal volume flow rates, the maximum values of this energy at trailing edge become little while it increases as the volume flow rate increase.

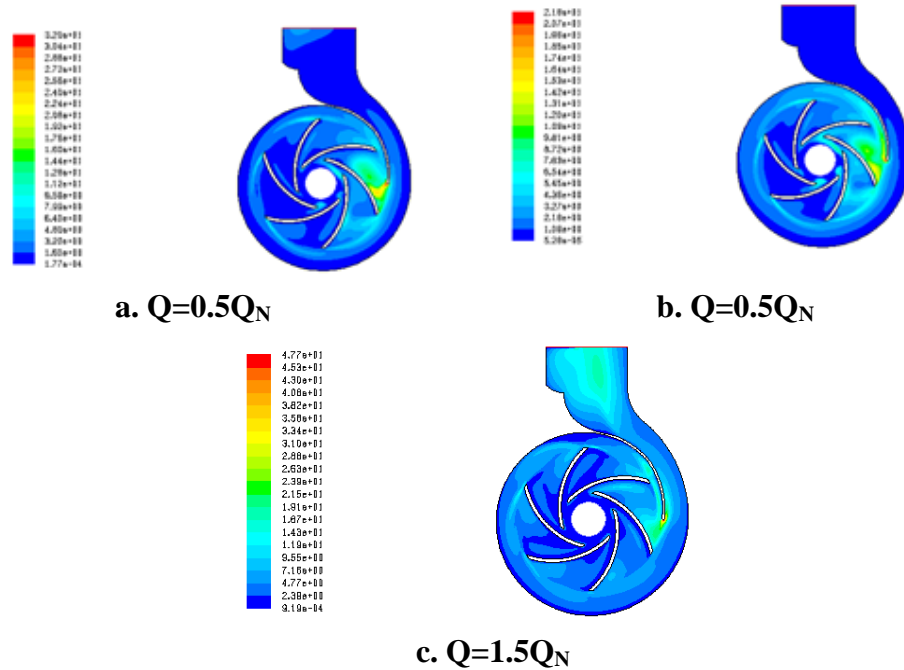


Fig.14 Contours of turbulent kinetic energy distribution (m/s) for impeller A.

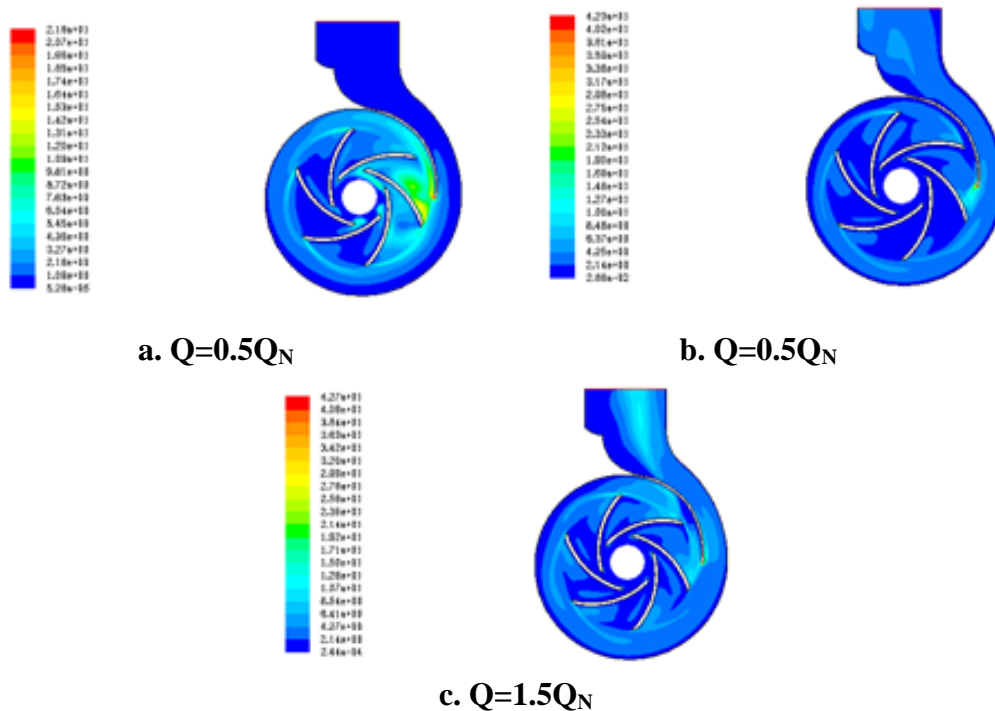


Fig.15 Contours of turbulent kinetic energy distribution (m/s) for impeller B.

4.2 Analysis of experimental results

Figures 16-17 show the distribution of the static pressure fluctuation around the impeller for two different values of diameters (impeller A & impeller B) at volume flow rates $Q=0.5Q_N$ & $Q=0.7Q_N$. It can be seen that the pressure fluctuations have a maximum value at position $\varphi=270^\circ$ and they have small values at other positions. This phenomenon occurs because of the switching in the flow trace between the recirculation duct and the discharge duct. It can be indicated that the pressure fluctuations have maximum values at volume flow rate ($Q=0.5Q_N$) for the two impellers (A & B). As the figures show, for a given flow rate, the maximum amplitudes of the pressure fluctuations increase as the impeller diameter increases i.e when reducing the blade to tongue gap. This is an expectable result since a smaller rotor-stator distance implies less space for the flow to adapt to the geometry changes, i.e., greater velocity gradients, greater stresses and, in summary, a greater fluid-dynamic interaction.

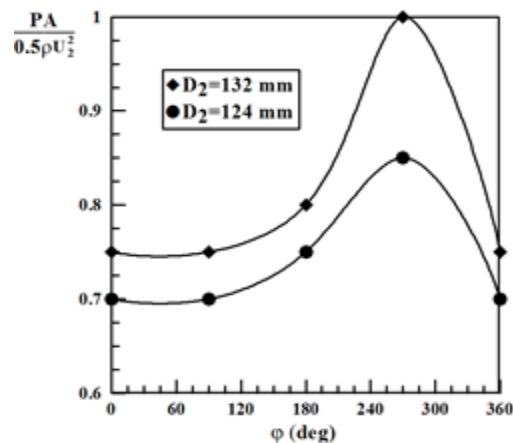


Fig. 16 Distribution of the pressure fluctuation around the angular position of the impeller at $Q=0.5Q_N$.

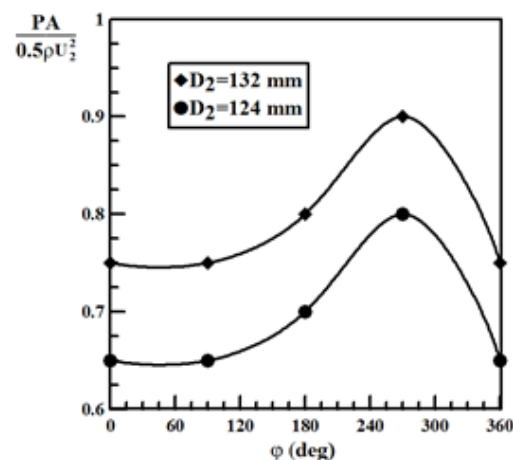


Fig. 17 Distribution of the pressure fluctuation around the angular position of the impeller at $Q=0.7Q_N$.

The variation of normalized static pressure distribution around the angular position of the two considered impellers (A & B) for nominal flow rate is shown in figure 18. It can be seen that the pressure fluctuations are not high in both impeller diameters at the tongue of the volute and there is a difference in the values of these fluctuations between impeller A and B. It can be noted that the pressure fluctuations have a maximum value at position $\varphi=100^\circ$ for impeller A and $\varphi=185^\circ$ for impeller B. Also the impeller A indicated the larger expected pressure fluctuations.

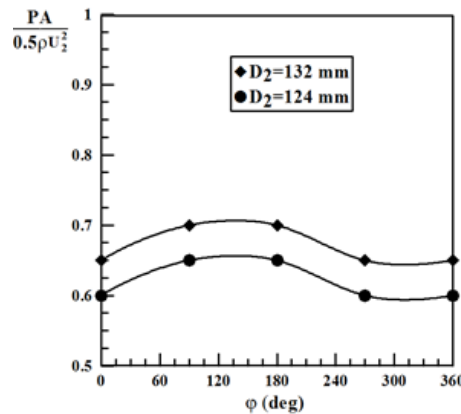


Fig. 18 Distribution of the pressure fluctuation around the angular position of the impeller at $Q=Q_N$.

Figures 19-20 show the distribution of the normalized pressure fluctuation around the angular position of the two considered impellers (A & B) for volume flow rate greater than nominal one. It can be noted that the trend of the pressure distribution is changed compared with the case of $Q < Q_N$. It is evident that the pressure fluctuation values are low and have the same value for the both impellers (A & B) at volute tongue. That means that the flow is accumulating at the tongue and because this accumulation, the pressure decrease at volute tongue. However, impeller A indicated the larger pressure distribution as expected.

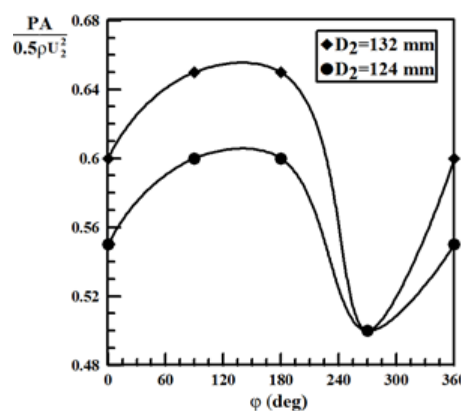


Fig. 19 Distribution of the pressure fluctuation around the angular position of the impeller A at $Q=1.3Q_N$.

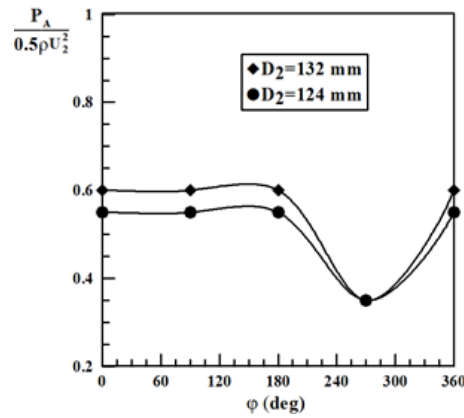


Fig.20 Distribution of the pressure fluctuation around the angular position of the impeller B at $Q=1.5Q_N$.

4.1 Validation

The results of experimental work is compared with the numerical results that obtained by using a commercial CFD Fluent 6.3 code as shown in figure 21-22. The numerical simulation were performed for the same geometry and locations considered in the experiments. It can be observed that an acceptable agreement is achieved between experimental and numerical result. However some discrepancies have arisen in the comparison between the numerical and experimental pressure fluctuation in the volute of the tested centrifugal pump, especially near tongue region. A part of these differences can be attributed to the leakage flow between the volute and the impeller inlet, which was not considered in the numerical model.

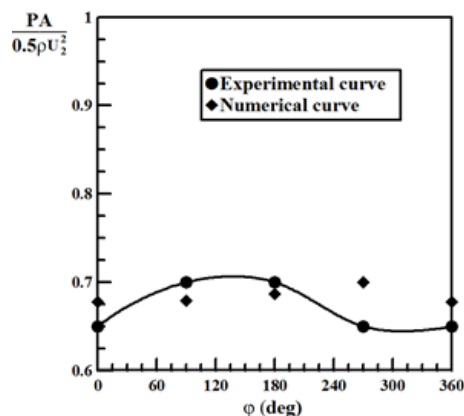


Fig. 21 Comparison between the present experimental and numerical results for impeller A at $Q=Q_N$.

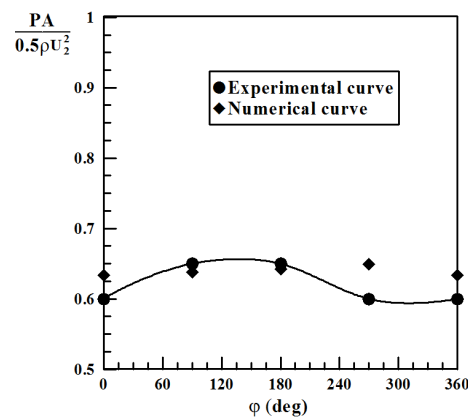


Fig.22 Comparison between the present experimental and numerical results for impeller B at $Q=Q_N$.

5. Conclusions

The following conclusions can be drawn from this study. The pressure fluctuations registered in the volute were found to be very dependent on both angular position and volume flow-rate, with maximum values corresponding to the tongue region for ($Q=0.5Q_N$) at angular position ($\phi=270^\circ$). Changing the impeller diameter from 124mm to 132mm results in an increase in maximum pressure fluctuation by a value approximated to 15%. The static pressure increases as the angular position (around the volute) increases and the higher pressure values can be observed upstream of the leading edge of the volute tongue (stagnation point). The static pressure has a minimum value at the impeller eye and around the impeller especially at angular position about ($\phi=185^\circ$) for impeller A and ($\phi=100^\circ$) for impeller B. Decreasing radial gap has a significant effect on the distribution of turbulent kinetic energy, where the level of the turbulence intensity is increased as the impeller diameter increases.

Nomenclature

b_1	Inlet blade width	mm
b_2	Outlet blade width	mm
D_1	Impeller inlet diameter	mm
D_2	Impeller exit diameter	mm
g	Gravity acceleration	m/s^2
H_t	Theoretical head	m
N	Speed	rpm
P	Static pressure	N/m^2
P_A	Pressure Amplitude	N/m^2
P_{in}	Input power	Watt
Q	Volumetric flow rate	m^3/s
Q_N	Volumetric flow rate at nominal point	m^3/s
R	Radial position	mm
t	Blade thickness	mm
u	Velocity in x -direction	m/s
U	Tangential velocity of impeller	m/s
U_2	Peripheral velocity at impeller outlet	m/s

v	Velocity in y-direction	m/s
V	Absolute velocity	m/s
V_a	Axial velocity	m/s
V_m	Meridional velocity	m/s
V_r	Radial velocity	m/s
W	Relative velocity	m/s
x	Horizontal coordinate	m
y	Vertical coordinate	m
Z	Number of impeller blades	-
∇	Gradient	-

References

- [1] van Esch, B. P. M., Performance and Radial Loading of a Mixed-Flow Pump Under Non-Uniform Suction Flow, ASME J. Fluid Eng., 131(2009), pp. 1-7.
- [2] Chu, S., Dong, R., and Katz, J., Relationship Between Unsteady Flow, Pressure Fluctuations, and Noise in a Centrifugal Pump; Part B: Effects of Blade-Tongue Interaction, ASME J. Fluids Eng., 117(1995), pp. 30–35.
- [3] Elholm, T., Ayder, E., Van den Braembussche, R., Experimental Study of the Swirling Flow in the Volute of a Centrifugal Pump, ASME J. Fluid Eng., 114(1992), pp. 366-372.
- [4] Timushev, S.E., and Ovsyannikov, B.V., Pressure Fluctuation Numerical Simulation in a Centrifugal Pump Volute Casing, Colloque C1, supplement au Journal de Physique III, 2(1992), pp.619-622.
- [5] Kaps, A., Numerical Flow Analysis in a Centrifugal Pump for Optimization of the Casing with Regard to Hydraulic Efficiency and Bearing Forces, Phenomena and Dynamic of Rotating Machinery, 2(1996), pp.345-354.
- [6] Qin, W., and Tsukamoto, H., Theoretical Study of Pressure Fluctuations Downstream of a Diffuser Pump Impeller – Part 2: Effects of Volute, Flow Rate and Radial Gap, ASME J. Fluid Eng., 119(1997), pp.
- [7] Wang, H., and Tsukamoto, H., Fundamental Analysis on Rotor-Stator Interaction in a Diffuser Pump by Vortex Method, ASME Journal of Fluids Engineering, 122(2001), pp. 737-747.
- [8] Shi, F., and Tsukamoto, H., Numerical Study of Pressure Fluctuations Caused by Impeller-Diffuser Interaction in a Diffuser Pump Stage, ASME Journal of Fluids Engineering, 123(2001), pp. 466-477.
- [9] Dong, R., Chu, S., and Katz, J., Quantitative visualization of the flow within the volute of a centrifugal pump. Part B: results and analysis. Trans. of the ASME, 114(1992), pp. 396-403.
- [10] Adnan Ozturk, Kadir Aydin, Besir Sahin and Ali Pinarbasi, Effect of impeller-diffuser radial gap ratio in a centrifugal pump Journal of Scientific & Industrial Research, 68(2009), pp.203-213.
- [11] Cheah, K.W., Lee, T. S., and Winoto, S. H., and Zhao, Z.M., Numerical Flow Simulation in a Centrifugal Pump at Design and Off-Design Conditions, International Journal of Rotating Machinery, Article ID 83641, 2007, 8 pages.
- [12] Fabio J. Silva, Jose C. Pascoa, Joao S. Pinheiro, and Daniel J. Martins, Turbulent Flow structure Computation Inside a Pump-Pat Using an Industrial Benchmark Test Case, European Conference Computational Fluid Dynamics, Lisbon, Portugal, 2010.
- [13] Raul Barrio, Jorge Parrondo, and Eduardo Blanco, Numerical analysis of the unsteady flow in the near-tongue region in a volute-type centrifugal pump for different operating points” International Journal Computers and Fluids, 39(2010) pp. 895-870.
- [14] Houlin, LIU., Yong, WANG., Shouqi, YUAN., Minggao, TAN., and Kai, WANG., “Effects of Blade Number on Characteristics of Centrifugal Pumps” Chinese Journal Of Mechanical Engineering, 23(2010).

Effect of GAMMA Rays on some types of viscosity and optical properties for polycarbonate in chloroform at room temperature

Harith Hasoon Jasim

E-mail: eng.harithjasim@yahoo.com / Mob. 07902493885

College of Engineering / Material Dept.

Al-Mustansiriya University

Bab Al-Moudam P.O.Box 14150 / Baghdad, Iraq

ABSTRACT

Some types of viscosity for polycarbonate aqueous solution in Chloroform with concentration of 1, 1.5, 2, 2.5, 3, 3.5, 4, 4.5 and 5% were determined for two kinds of samples, first non-radiated & the second, irradiated with Co^{60} source for a rate of 508 rad/min for 20 minutes.

The results show that the values of shear, relative, specific & reduced viscosity were increased with increasing the concentration of polycarbonate in chloroform, Also the properties which had been determined in this work, increased after radiation, this could be attributed to penetration of ionizing radiation in the polymer structure & cross linking the chains.

Key words: GAMMA Rays, Polycarbonate, Viscosity.

الخلاصة

تم تعيين قيم بعض أنواع اللزوجة لبولي كاربونيت المذاب في الكلوروفورم وبتراكيز ١، ١.٥، ٢، ٢.٥، ٣، ٣.٥، ٤، ٤.٥ و ٥% قبل وبعد تشعيعها بمصدر Co^{60} وبمعدل ٥٠٨ راد لكل دقيقة ولمدة ٢٠ دقيقة. أظهرت النتائج إن قيم كل من اللزوجة القصية، اللزوجة النسبية، اللزوجة النوعية، اللزوجة المختزلة تزداد بزيادة تركيز البولي كاربونيت في الكلوروفورم. كذلك تزداد قيم الخصائص المقاسة والمحسوبة بعد التشعيع وقد يكون ذلك بسبب التشابك في التركيب الجزيئي لهذا البوليمر لاختراق أشعة كاما لبنية مولدات حالة التشابك في البنية التركيبية للبوليمر.

INTRODUCTION

Many articles consist of the effect of radiations on polycarbonate radiation especially in chloroform has been published ⁽¹⁻⁴⁾.

The aim of this work is to study some rheological and optical properties of polycarbonate in chloroform solvent at different concentrations before and after radiation by GAMMA source (Co^{60}).

There are a number of methods for determining experimentally the molecular weights of polymers. These include both the measurement of number-average and weight-average molecular weights. It will be seen that solution viscosity offers a very convenient method but it is not an absolute method and does not give one of the simple averages. The resolution of molecular lengths into fractions and therefore measurement of molecular weight distribution is also possible experimentally. Unlike small molecules, however, the molecular weight of a polymer is not one unique value. Rather, a given polymer will have a distribution of molecular weights. The distribution will depend on the way the polymer is produced. For polymers we should not speak of a molecular weight, but rather of the distribution of molecular weight, $P(M)$, or of the average molecular weight, $\bar{P}(M)$. Polymer physical properties will be functions of the molecular weight distribution function ⁽⁵⁾. The molecular weights of polymers are much larger than the small molecules usually encountered in organic chemistry. Most chain-reaction and step-reaction polymerizations produce chains with many different lengths, so polymers also differ from small molecules in that the polymer molecular weights are average values. ⁽⁶⁾

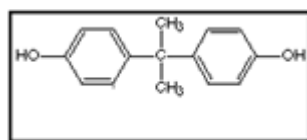
The viscometer used to measure dilute solution viscosity is usually a capillary viscometer. This viscometer uses the Poiseuille equation for laminar pressure flow in a capillary tube. Intrinsic viscosity is theoretically a primary technique, in that for the theta solvation conditions secondary standards are not necessary. In usual practice, at non-theta conditions, intrinsic viscosity relies on knowledge of the Mark-Houwink coefficients for the thermal and solvent conditions of measurement. ⁽⁵⁾

Beer-Lambert Law, more commonly known as Beer's Law, states that the optical absorbance of a chromophore in a transparent solvent varies linearly with both the sample cell path length and the chromophore concentration. Beer's Law is the simple solution to the more general description of Maxwell's far-field equations describing the interaction of light with matter. In practice, Beer's Law is accurate enough for a range of chromophores, solvents and concentrations, and is a widely used relationship in quantitative spectroscopy. Absorbance is measured in a spectrophotometer by passing a collimated beam of light at wavelength λ through a plane parallel slab of material that is normal to the beam. For liquids, the sample is held in an optically flat, transparent container called a cuvette.⁽⁷⁾

EXPERIMENTAL

Material

Polycarbonates are long-chain linear polyesters of carbonic acid and dihydric phenols,



Used in making canopies for supersonic aircraft, bubble helmets for astronauts, break-resistant windows, and bullet-resistant laminates for banks and armored cars. It is also used for computer housings where mechanical, electrical and re-resistance properties are needed. It is also used in steam-sterilizable food-processing equipment⁽⁸⁾. The properties of polypropylene are shown in Table 1.

Samples preparation

Using Chloroform (from GAINLAND CHEMICAL COMPANY), 9 different concentrations of each sample at room temperatures were prepared (1, 1.5, 2, 2.5, 3, 3.5, 4, 4.5 and 5%); the solutions were prepared by adding a known weight of the polymer to fixed volume of Chloroform. The properties of Chloroform are shown in Table 2.

Viscosity measurements

For determining the viscosities of the solutions we used (HAAKE / Rotovisco Rv-20) viscometer at room temperature to find the shear viscosity digitally.

Irradiation method

The main source of (GAMMA) rays used in this work was Co^{60} with low dose rate irradiation, about 508 rad / min for 20 minutes on a disk shape samples with a thickness about 0.5 cm, where used in order to obtain dose uniformly during the irradiation. The distance between the source and the sample was 10 cm.⁽¹¹⁾

THEORETICAL CALCULATION

Relative, specific & reduced viscosity:

The above viscosities were calculated by using the following relations⁽⁹⁾:

$$\eta_{rel} = \eta_s / \eta_w = t_s / t_w \quad (1)$$

$$\eta_{sp} = \eta_{rel} - 1 \quad (2)$$

$$\eta_{red} = \eta_{sp} / C \quad (3)$$

Where:

η_{rel} is the relative viscosity

η_s is the viscosity of solution

η_w is the viscosity of solvent

t_s & t_w are the flow time of the solution and solvent respectively

η_{sp} is the specific viscosity

C is the sample's concentration.

Intrinsic viscosity $[\eta]$:

Plotting a graph for η_{re} against concentration of all samples had been drawn; the intercept with Y - axis of this graph is $[\eta]$.

Molecular weight (M_v):

An empirical equation is used to describe the intrinsic viscosity / molecular weight relationship, the Mark-Houwink equation,

$$[\eta] = KM_v^a \quad (4)$$

Where (a) and (K) are constants for specific polymer / solvent / temperature.

The values of $|\eta|$ had been taken from table (3), and the constants (K, a) are depended on polymer type at a temperature range of 15 – 25°C⁽¹⁰⁾. The value of the M_v of this polymer was calculated from following relation⁽¹¹⁾:

$|\eta| = 4.83 \times 10^{-4} M_v^{0.82}$, the calculated values are shown in table (4).

Molar absorption coefficient (α):

To calculate the optical absorption coefficient (α) of the samples, Lambert-Beer law equation was used:

$$\log \frac{I_0}{I} = A = \alpha \cdot C \cdot L \quad (5)$$

Where

I_0 the intensity of incident beams of light for special wavelength.

I the absorbed intensity of the same beam.

α the optical absorption coefficient

A the absorbance of the same beam.

L the length of solution the light pass through, cm

If we plot A against C , and if we substitute $L=1$ cm. in equation 5 which represents the thickness of the test tube, therefore^[12]

$$\alpha = A / C \quad (6)$$

RESULTS & DISCUSSION

The result of most measured and calculated physical properties for polycarbonate as shown in most figures and tables are increased with concentration due to phenyl groups and methyl groups in its structure. These results are concurring with the results found by Robertson⁽¹³⁾ who used another solvent. The value of intrinsic viscosity and average viscosity molecular weight determined in this work (tables 3 & 5) increase after irradiation by Co^{60} source could be attributed to formation of very reactive intermediates products (excited states, ions and free radicals), which result in rearrangements and/or formation of new bonds and this agreed with the conclusion of J.H. Donnell⁽¹⁴⁾

The optical absorption coefficient (α) is calculated using equation 5 as shown in table 5. The results show that it decreased after radiating the polymer.

Low dose radiation very clear in viscosity figures (figures1 to 4), we see the approach in radiated and non-radiated curves leads to slight increase in average viscosity molecular weight that is because the degree of cross-linking depends upon the polymer and radiation dose. One of the benefits of using irradiation for cross-linking is that the degree of cross-linking can be easily controlled by the amount of dose.

Also the results of UV and visible spectrum of polymer in solution show the existence of both inter and intra-molecular hydrogen bonds, this polymer appears to be a good transparent at 220nm., therefore result suggests that weak absorption exist in the region (240-700) nm., such week absorption may be due the presence of impurity.⁽¹⁶⁾

The ionized gamma irradiation affected the refractive index of polymer (figure 5) and therefore it changes the polarization of the incident light. The difference in the polarization phase shift of the polymer depended on the dose it had been irradiated with.⁽¹⁸⁾

Irradiation in polymers destroys the initial structure by way of cross linking, free radical formation, irreversible bond cleavages etc. that results in the fragmentation of molecules and formation of saturated and unsaturated groups. All these processes introduce the so called defects inside the material that are responsible for change in the optical, electrical, mechanical and chemical properties of the material.⁽¹⁷⁾

Table 1: Properties of polycarbonate

Property	Value
Tensile Strength	0.90 - 1.32 N/mm ²
Notched Impact Strength	3.0 - 32.0 Kj/m ²
Thermal Coefficient of Expansion	100 - 140 x 10 ⁻⁶
Max. Continued Use Temperature	80 °C
Melting Point	160 °C
Glass Transition Temp. (atactic)	-20 °C
Glass Transition Temp. (isotactic)	100 °C
Density	0.906 g/cm ³

Table 2: Properties of Chloroform

Property	Value
Molecular weight	119.38
Boiling point	61.15°C
Vapor pressure	158.4 Torr at 20°C
Freezing point	-63.55°C
Refractive index	1.4458 at 20°C
Density	1.4798 g/mL at 25°C
Dielectric constant	4.81 at 20°C
Viscosity	0.57 cP at 20°C
Surface tension	27.16 dyn/cm at 20°C
Solubility in water	0.815% at 20°C

Table 3: Values of intrinsic viscosity before and after irradiation

Intrinsic viscosity(di/gm)	albumin
0.1772	before irradiation
0.2073	after irradiation

Table 4: Values of average viscosity molecular weight before and after Irradiation for polycarbonate in Chloroform

Mv Average viscosity molecular weight	polycarbonate
278.3281718	before irradiation
355.646892	after irradiation

Table 5: Molar absorption Coefficient for polycarbonate in Chloroform

Molar absorption Coefficient	Solvent
0.0271	before irradiation
0.017	after irradiation

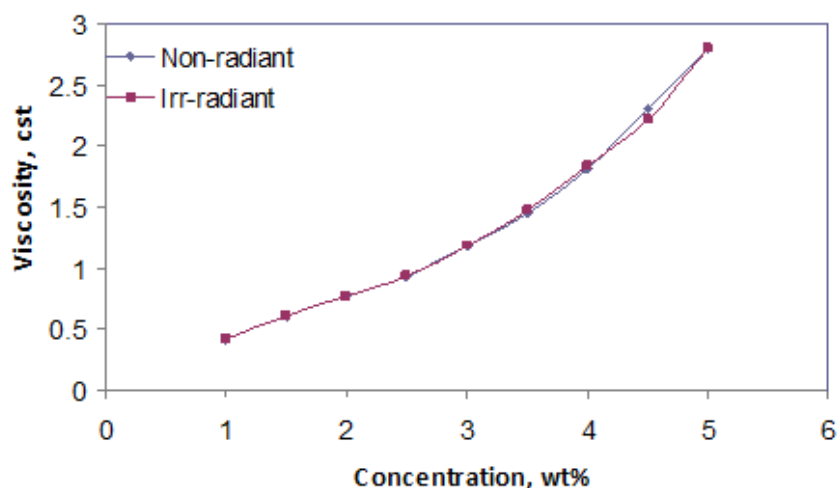


Figure 1: Shear Viscosity of polycarbonate changed with concentration.

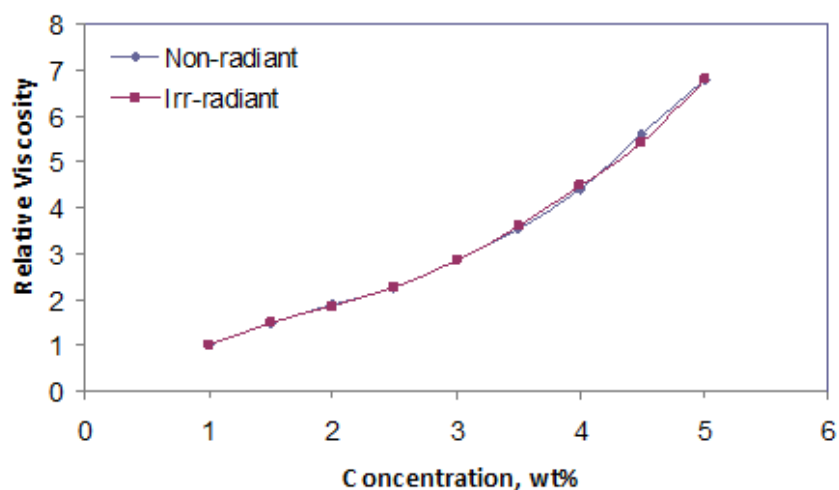


Figure 2: Relative viscosity of polycarbonate changed with concentration.

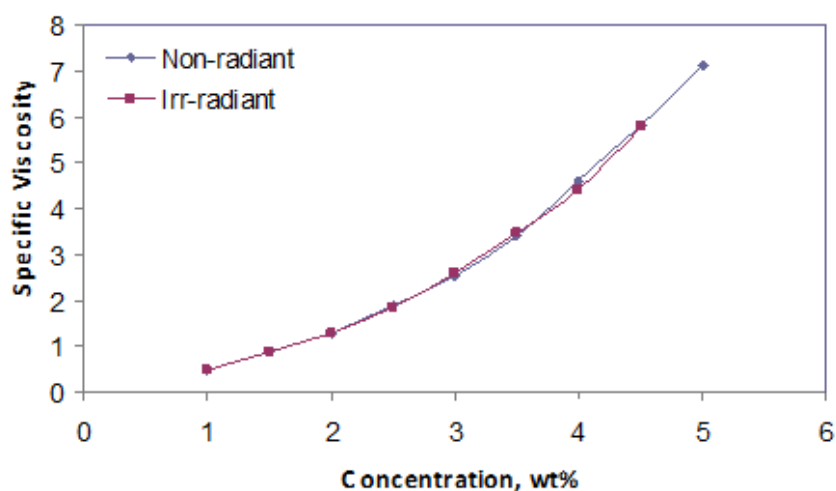


Figure 3: Specific viscosity of polycarbonate changed with concentration.

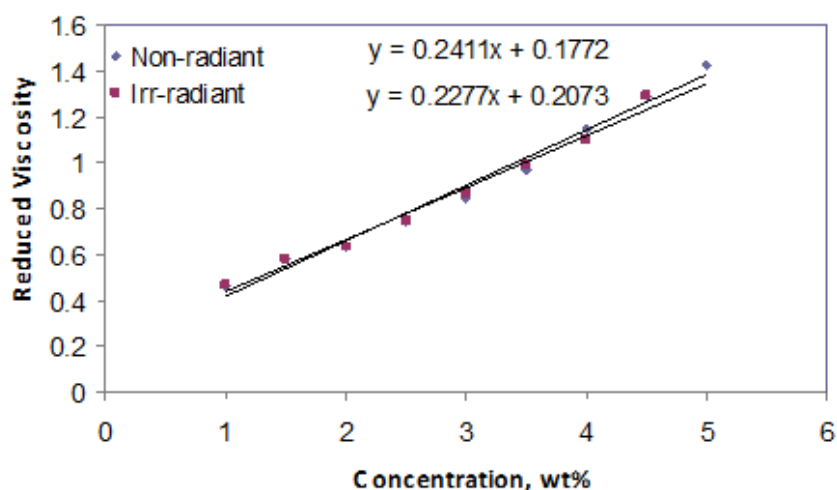


Figure 4: Reduced viscosity of polycarbonate changed with concentration.

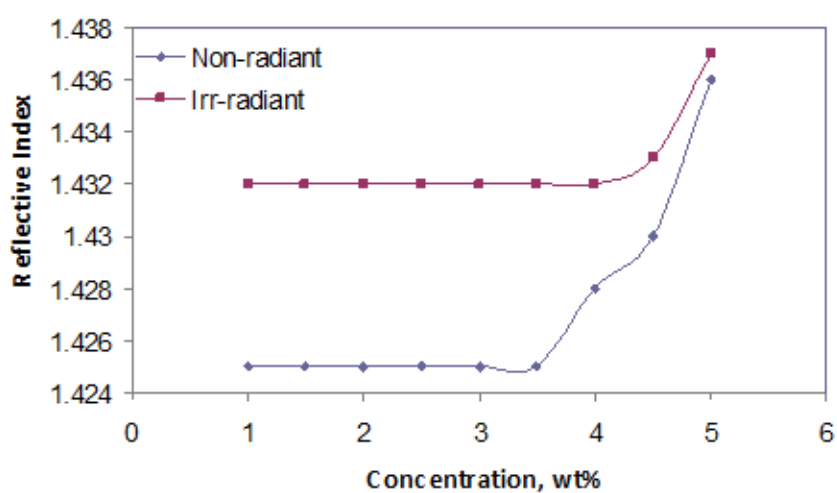


Figure 5: refractive index of polycarbonate changed with concentration

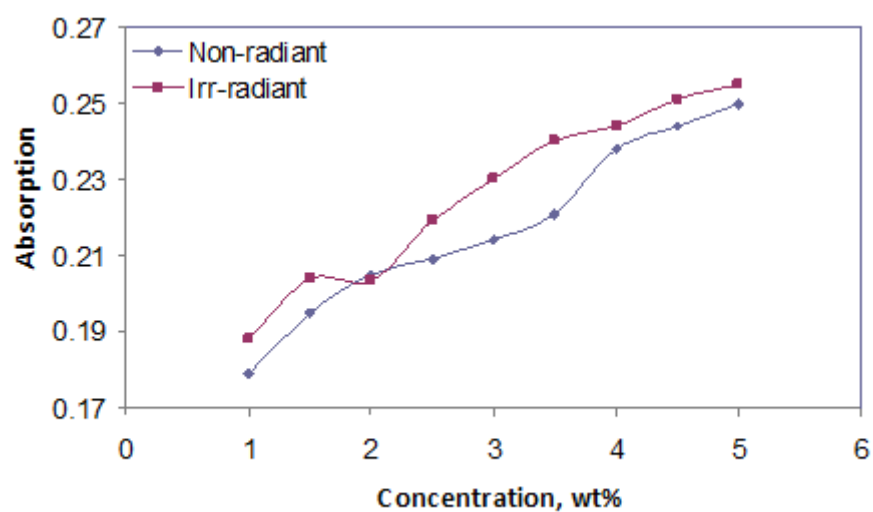


Figure 6: absorption of polycarbonate changed with concentration

CONCLUSION

1. The effect of Co^{60} source on polycarbonate yield increasing in its molecular weight as reported.
2. The free roots & ions in radiated polycarbonate help to cross linking process that happened after radiation.
3. The increasing in molecular weight of this polymer after radiation may be useful to using this polymer in some high molecular weight polymers technology.

REFERENCES

1. A. Shamshad, M. Rashid and A. Husain "High gamma dose dosimetry by polycarbonates" Chemistry Volume, September 1997, Pages 307-311.
2. G. F. Tjandraatmadja, L. S. Burn, M. C. Jollands "Evaluation of commercial polycarbonate optical properties after QUV-A radiation—the role of humidity in photodegradation", Polymer Degradation and Stability, Volume 78, Issue 3, 2002, Pages 435-448.
3. A. Yu. Orlov, V. I. Feldman "Effect of phase condition on the low-temperature radiation-induced degradation of polycarbonate as studied by spectroscopic techniques", Polymer, Volume 42, Issue 5, March 2001, Pages 1987-1993.
4. RuizhiWu, Jian-Feng Zhang, Yuwei Fan, Diana Stoute, Thomas Lallier and Xiaoming Xu "Reactive electrospinning and biodegradation of cross-linked methacrylate polycarbonate nanofibers" Biomedical Materials, Volume 6, No. 3, 2011.
5. L.H. sperling, "introduction to physical polymer science", Forth ed., John wiley & sons, Inc., Canada, 2006.
6. K.A.Flaih, "Introductory to Biochemistry", Mussel university, 2000.
7. V. Barone, " Computational Spectroscopy: Status and Perspectives", Wiley-Interscience, 2011.

8. James E. Mark "POLYMER DATA HANDBOOK" Oxford University Press, Inc. 1999.
9. Iwao Teraoka," Polymer Solutions", John Wiley & Sons, Inc. 2002.
10. P. J. Flory and F. S. Leutner, J. Poly. Sci., 3, 880 (1948).
11. W.R. Moore, M. Uddin, J, " Dilute solution properties of bisphenol A polycarbonate—I Osmotic, light scattering and viscosity measurements ",Eu. Poly. Jo., Vol. 5, Is. 1 , 2003.
12. J. D. J. Ingle and S. R. Crouch, Spectrochemical Analysis, Prentice Hall, New Jersey, 1988.
13. Robertson, Jennifer E.," Thermal Degradation Studies of Polycarbonate", PhD Dissertation, Virginia tech. USA, 2001.
14. J.H.O'donnell & D.V.sangster, Trs, K.Y.Alyamoor, "Principles of radiation chemistry" Mussel University, 1985.
15. A. M. S. Galante, L. L. Campos" The Radiation Effect of Co⁶⁰ Gamma Rays on Polycarbonate detector", Institute of Energetic and Nuclear Research, Brasil,2006.
16. S. K. Hassun, R. M. Raouf, "the effect of GAMMA radiation on some physical properties and molecular structure of aqueous solutions op PVA", Jo. Of Basic and Applied Science, Is. No.8, 2000.
17. T. Sharma, S. Aggarwal, S. Kumar, V. K. Mittal, P. C. Kalsi, V.K. Manchanda, "Effect of gamma irradiation on the optical properties of CR-39 Polymer" Jo. Mater Sc., Volume 42, No. 4, Pages 1127-1130, 2007.
18. 18-S.M.R. Aghamiri, M. Namedanian , Z. Sanjabi , " Effect of gamma irradiation on the light polarization variation of PMMA polymer ", Jo. Sc. Direct, Vol.281, Is.3, 2008.

NEURAL NETWORKS OF ENGINE FAULT DIAGNOSIS BASED ON EXHAUST GAS ANALYSIS

Rafil M. Laftah

Dean Assistant of Engineering College
Basrah University
rafil_74@yahoo.com

Qusai T. Abd-Alwahab

Educational in Engineering College
Basrah University
qusaith@yahoo.com

Jaafar M. Hamzah

Lecturer in Engineering College
Thiagar University
jaafar_2011m@yahoo.com

Abstract: This work uses the Artificial Neural Networks (ANNs) for fault diagnosis of a single cylinder four stroke gasoline generator type (Astra Korea AST11700). One normal and fourteen faulty conditions are examined experimentally to produce a realistic data set, which is to be used for the training and validation of the ANNs. The resulted data was in the form of exhaust gases and engine speed records for each case separately under different loading conditions. After the learning process is completed, the ANN becomes able to make a diagnosis about the gasoline engine condition when new data is presented. The data presented to the ANN system include a subset of engine faults which were selected and executed experimentally for this topic. These include, faults in carburetor, air filter, spark plug, valves, piston rings, etc. The results showed that the multi layer training algorithm is sufficient enough in diagnose engine faults under different loading conditions. It was found that the correlation coefficient values are 0.999 and 1 for the testing and training data, respectively. The results obtained in this investigation showed that the ANN-based fault diagnosis system is capable of fault diagnosis with high reliability.

Keywords: Artificial neural network; IC engine; Exhaust gas analysis; Fault diagnosis; Prediction

الخلاصة: يستخدم هذا العمل الشبكات العصبية الاصطناعية لتشخيص أعطال مولد كهربائي ذو محرك بأسطوانة واحدة رباعي الأشواط. لقد تم اختبار أربعة عشر نوع من الأعطال بالإضافة إلى الحالة الطبيعية عملياً لغرض إنتاج مجموعة من البيانات الشاملة والواقعية، استعملت هذه البيانات لتدريب وتحقيق الشبكة. كانت البيانات الناتجة على شكل غازات العادم وسرعة المحرك المسجلة لكل حالة على حدة في ظل ظروف تحميل مختلفة. بعد انتهاء عملية التعلم، تكون الشبكة قادرة على التشخيص عند استخدام بيانات جديدة. البيانات المدخلة إلى الشبكة العصبية الصناعية تتضمن مجموعة من أعطال المحرك التي نفذت بشكل تجريبي لهذا الغرض. ومن هذه الأعطال، خلل في نظام المكربنة، نظام ترشيح الهواء، شمعة القدح، الصمامات، وحلقات المكبس... الخ. أظهرت النتائج أن خوارزمية تدريب الرجوع العكسي هي كافية في تشخيص أعطال المحرك تحت ظروف التحميل المختلفة. وجد أن قيم معامل الارتباط هي 0.999 و 1 لبيانات الاختبار و التدريب، على التوالي. وأظهرت النتائج في هذا التحقيق أن نظام تشخيص الأخطاء المستند على الشبكات العصبية قادر على اكتشاف الخطأ والتشخيص مع موثوقية عالية.

1. Introduction

All real systems in nature – physical, biological and engineering – can malfunction and fail due to faults in their components. The chances for failures are increasing with the system's complexity. System fault can be defined as any undesirable or abnormal behavior. The complexity of engineering systems is permanently growing due to the growing of size of the systems and the degree of automation, which increases the chances for faults and aggravating their consequences for man and environment. Therefore, increased attention has to be paid to the reliability, safety and fault tolerance in the design and operation of engineering systems [1].

The cognitive approach of artificial intelligence is focusing on imitating the rational thinking of human. Artificial intelligence system such as fuzzy logic, neural networks and genetic programming had been integrated with the conventional fault diagnosis system to produce intelligent diagnostic systems [2].

2. Fault Diagnosis Methods

Fault diagnosis is the act of detecting and isolating faults present in a system. With the rising demand for safety and reliability of technical systems, driven by economical and environmental incentives, fault diagnosis has become increasingly important. One example is automotive systems that are by regulations required to have on-board diagnosis of all faults that may lead to increased emissions. In addition, fault diagnosis in automotive systems is essential to maintain high vehicle uptime, low fuel consumption, high safety, and efficient service and maintenance [3]. Fault diagnosis methods can be classified into two general categories, model-based and data driven methods. The hierarchy of fault diagnosis approaches is shown in Fig. 1.

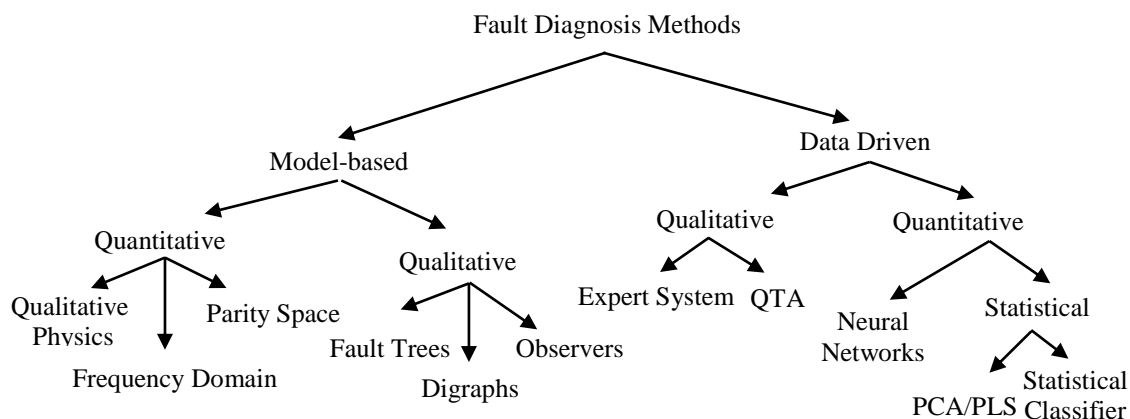


Fig. 1: Classification of Fault Diagnosis Methods [4]

3. Artificial Neural Networks

Artificial Neural Networks (ANNs) are a branch of the field known as "Artificial Intelligence" which may also consists of Fuzzy Logic (FL) and Genetic Algorithms (GA) [5]. Artificial neural networks are non-linear mapping structures based on the function of the human brain [6]. They are powerful tools for modeling, especially when the underlying data relationship is unknown. ANNs can identify and learn correlated patterns between input data sets and corresponding target values [7].

Neural networks are composed of simple elements operating in parallel. These elements are inspired by biological nervous systems. As in nature, the network function is determined largely by the connections between elements. It can train a neural network to perform a particular function by adjusting the values of the connections (weights) between elements. The weights adjusting process is usually called learning process. Commonly neural networks are adjusted, or trained, so that a particular input leads to a specific target output [8].

The block diagram of Fig. 2 shows the model of a neuron, which forms the basis for designing (artificial) neural network. Here we identify three basic elements of the neuronal model [9].

1. A set of synapses or connecting links, each of which is characterized by a weight or strength of its own. Specifically, a signal (p_i) at the input of synapse (i) connected to neuron (j) is multiplied by the synaptic weight w_{ij} .
2. An adder for summing the input signals, weighted by the respective synapses of the neuron.
3. An activation (or transfer) functions for limiting the amplitude of the output of a neuron.

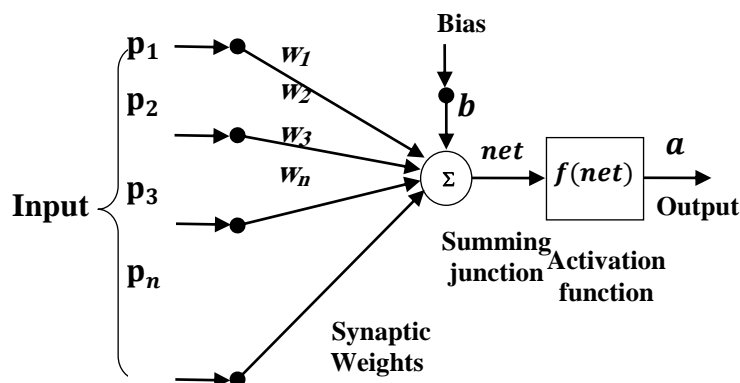


Fig. 2: Structure of a Single Artificial Neuron

3.1 Training of Multi-Layer Perceptron

The Multi-Layer Perceptron (MLP) is a nonparametric technique for performing a wide variety of estimation tasks. Error Back-Propagation is one of the most important and widely used algorithms for training multilayer perceptron's [10]. Training process of MLP networks continues until a certain number of iterations or a desired error rate is reached. The most common error approximation method used in MLP networks is mean square error (MSE) and it is defined by the following formula [11]:

$$\text{MSE} = \left(\sum_{k=1}^n \sum_{j=1}^m (t_j^k - a_j^k)^2 \right) / s.l \quad (1)$$

3.2. Error Back propagation (EBP)

MLP have been applied successfully to solve some difficult diverse problems by training them in a supervised manner with a popular algorithm known as the EBP algorithm. BP algorithm was first defined by Werbos (1974) and later improved by Rumelhart et al. (1986) [12] as a euphemism for generalized delta rule. The BP generalize delta rule is a decent method to minimize the total squared error of the output computed by the net. The Back propagation algorithm is used in layered feed-forward ANNs. This means that the artificial neurons are organized in layers, and send their signals “forward”, and then the errors are propagated backwards [13]. The training procedure consists of two main steps: Feed-forward and back-propagation. During forward pass the synaptic weights of network are all fixed. During backward pass, on the other hand, the synaptic weights are all adjusted in accordance with the error-correction rule. Specifically, actual response of the network is subtracted from a desired response to produce an *error signal*. This error signal is then propagated backward through the network, against direction of synaptic connections - hence the name “error back-propagation” [14].

3.3. Back propagation Training Algorithm

The back propagation (BP) training algorithm involves three stages the feed forward of the input training pattern, the calculation and back propagation of the associated weight error and the weight adjustments. The training algorithm (for one hidden layer) is as following [15]:

Step 1: Initialize the weights.

Step 2: While squared error is greater than a tolerance, execute steps 3 to 11.

Step 3: For each training pair, do steps 4 to 11.

Step 4: Sums the weighted input and bases and apply the activation function to compute the output of hidden layer.

$$a_j = f(\sum p_i w_{ij} + b_j) \quad (2)$$

Step 5: Sums weighted output of hidden layer and apply activation function to compute output.

$$a_k = f(\sum a_j w_{jk} + b_k) \quad (3)$$

Step 6: Compute back propagation error

$$\delta_k = (t_k - a_k) f'(\sum a_j w_{jk} + b_k) \quad (4)$$

Step 7: Calculate weight correction term

$$\Delta w_{jk}(\tau) = \eta \delta_k a_j + \mu \Delta w_{jk}(\tau - 1) \quad (5)$$

Step 8: Sums delta input for each hidden unit and calculate error term

$$\delta_j = \sum_k \delta_k a_k = \sum_k \delta_k (w_{jk} f(\sum_i p_i w_{ij} + b_j) + b_k) \quad (6)$$

Step 9: Calculate weight correction term

$$\Delta w_{ij}(\tau) = \eta \delta_j p_i + \mu \Delta w_{ij}(\tau - 1) \quad (7)$$

Step 10: Update weights

$$w_{jk}(\text{new}) = w_{jk}(\text{old}) + \Delta w_{jk} \quad (8)$$

$$w_{ij}(\text{new}) = w_{ij}(\text{old}) + \Delta w_{ij} \quad (9)$$

Step 11: Compute the mean squared error.

4. Experimental Work

The current work concerns the study of engine faults and suggesting the proper diagnosis for each fault. There are certain requirements necessary to achieve this task:

- Proper selection of test engine, in our case engine is selected due to its wide spread domestic use in Iraq.
- Selection of the suitable gas analyzer (with new factory calibration).

- Selecting set of engine faults, which will be discussed below.
- Framing the diagnosing program (ANN techniques)

The experimental procedure can be summarized in two steps. The first step is to prepare test equipments and connect the engine to the gas analyzer which is in turn connected to a personal computer. The analyzer sample gas pipe is to be connected to exhaust tail pipe. The RPM clamp counter is connected to the engine spark plug cable. All the above mentioned steps were followed according to the user manual of the gas analyzer. The second step consists of three processes:

1. Turn on the gas analyzer while the engine is running at speed of 3800 *rpm* and wait until the oil temperature reaches 80 °C .
2. Take measurements of the five exhaust concentrations plus (λ) at four loading cases: no load, one third load, two thirds load and full load (2.5 kW), this performed by loading the engine with electrical heater.
3. Repeat process 2 fifteen times: one with normal operation and fourteen with faulty operation.

Then the readings were collected and fed to the ANN as an input data. Fig. 3 shows the map of the experimental work as explained before.

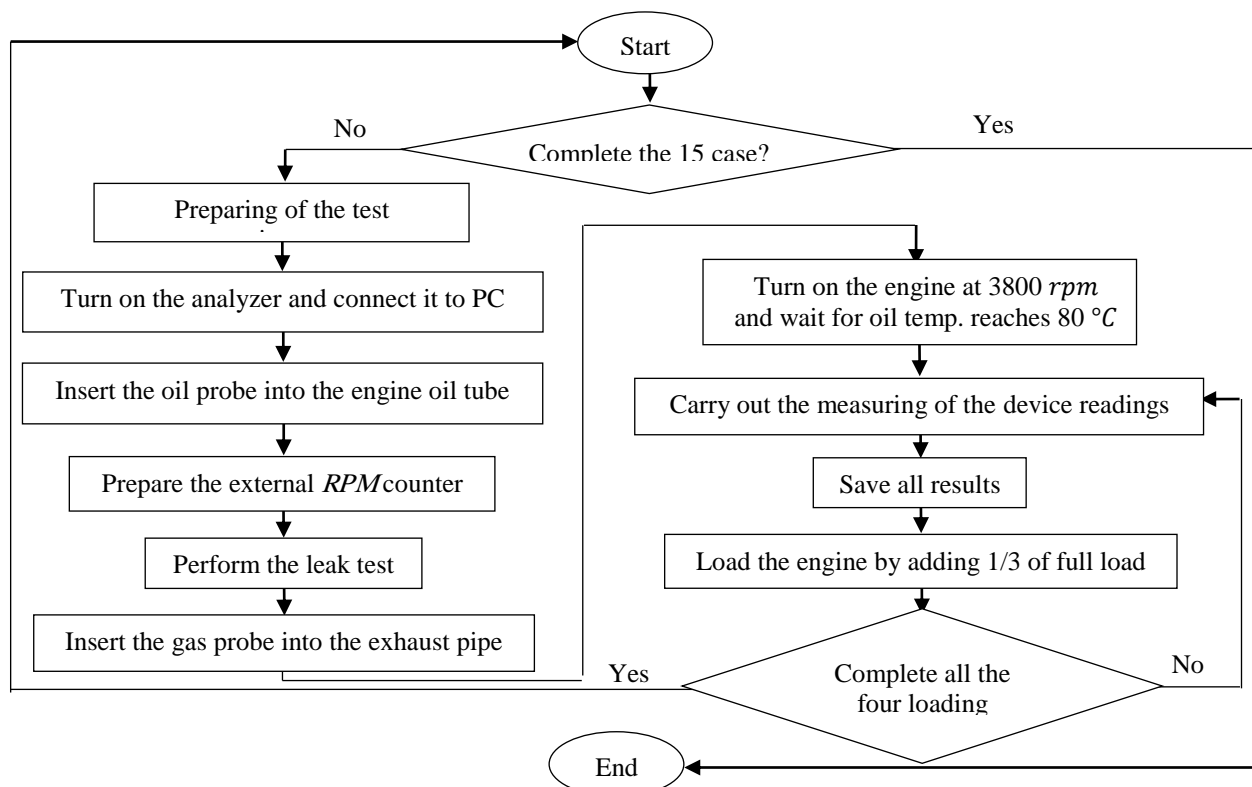


Fig. 3: Map of the Experimental Work

5. Selected Engine Faults

In order to perform engine faults diagnosis, it is required to run the engine under normal operation first and then to run it under faulty operation for each case. Fourteen engine faults were suggested. These faults were selected according to their frequent occurrence in practice. The faults can be listed hereunder with summarized description of the purpose of selecting each fault.

1. *Bad Lubricant*: Unchanging oil for time longer than specified can lead to increase engine temperature and reduce its efficiency, which leads to significant effect on engine operation.
2. *No Air Cleaner Used*: Air cleaner is very important element; it cleans the air entering the carburetor from the dust and dirt. Running of the generator without this element may be resulted in rapid engine wear [16]. This case is considered as engine fault since it affects carburetor operation, which in turn reduces the efficiency of engine operation.
3. *Dusty Air Cleaner*: Dusty air cleaner may result in lack of the air supplied to the carburetor. This in turn will give effect similar to choking of the engine. This fault affects the air/fuel ratio directly, thus, it leads to increase the emissions.
4. *Removed Evaporated Oil Tube*: Oil tube is the tube in which evaporated oil can be transferred from the overhead valve to the carburetor inlet, this process causes to lubricate the piston crown beyond the piston rings. Removing this element affects the lubricating system, and then it affects engine efficiency.
5. *Small Spark Plug Air Gap*: Spark plug gap affects directly the spark intensity. Unsuitable air gap leads to improper spark intensity, which in turn leads to incomplete combustion due to ignition misfire. By reducing air gap, the ignition will start before normal ignition time. That leads to ignition misfire and causes engine fault.
6. *Large Spark Plug Air Gap*: The increase of the spark plug gap leads to lack in spark intensity, then incomplete combustion due to ignition misfire.

Partially Blocked Carburetor Main Fuel Jet: The main jet is one of the carburetor elements, in which the fuel is transferred through it from the orifice. By making an obstruction through the orifice to make its diameter (1.4 mm), the fuel transferred for mixing with air will be reduced causing lean mixture introduced to the combustion chamber.

7. *Carburetor Main Jet Orifice Diameter is (0.7 mm)*: This case was similar to the previous, but here the orifice diameter was (0.7 mm) which making the mixture leaner than the previous case, so we can consider this case as a carburetor fault as the former but greater degree.
8. *Leak in Inlet Valve*: The leak in the both seat or face valve escape the compression mixture, with reduce engine efficiency. Also, the valve spring gives the same fault.
9. *Leak in Exhaust Valve*: This fault is considered as important situation, since it causes to lose some of the combustion chamber charge through the tailpipe, which in turn reduces the pressure in the combustion chamber. This fault is introduced by replacing the exhaust valve by an old valve subjected to remarkable erosion level.
10. *Crack in the Tailpipe*: Tailpipe crack is undesirable; it causes an offhand manner because of generated noise. This fault is introduced in this study because it could be diagnosed easily.
11. *The Gasket is ruptured*: This case will result to burn some of lubrication oil with combustion chamber charge. Then, many problems will happen due to this fault such as temperature rise, oil lacking and emission increase.
12. *Wearing of the Rings*: When the piston rings become exhausted, as it used in this case, a complex problem will happen such as oil burning, pressure leaking and unstable operation.
13. *A Problem in the Cooling System*: Cooling air is coming from the fan will spread by untying the screw which ties the plate to the engine fins body. This case reduces cooling system efficiency; therefore, which affects directly on the engine operation and emissions.

6. Results and Discussion

ANN is developed to diagnose the engine faults using exhaust gas analysis. This section describes the data selection for training and testing patterns, the topology of the constructed network, the training process and the verification of the neural network results. The total experimental data are divided into two sets: a training set and a testing set. The training set is used for computing the gradient and updating the network weights and biases to diminish the training error, and find the relationship between the input and output parameters.

The testing set is used to evaluate the generalization ability of the learning process. In this study the testing set contains approximately (15) % of total data base; however, other ratios were executed in this investigation. The parameters used in this study are shown in Table 1. The experimental values used to train the neural network as training data are those measured using exhaust gas analyzer. The total number of (300) test cases were utilized, each five readings in this data represent one loading cases and each twenty columns in this data represent four loading cases of one fault case. The training set contains (254) cases and the testing set comprises of (46) cases.

Table 1: Input and Output Parameters

<i>Item</i>		<i>Range of Parameters</i>		<i>Unit</i>
		<i>From</i>	<i>To</i>	
Input	Carbon Dioxide (CO_2)	9.04	13.47	%
	Carbon Monoxide (CO)	0.253	5.024	%
	Oxygen (O_2)	0.34	2.81	%
	Unburned hydrocarbon (HC)	4	673	ppm
	Nitrogen Oxidize NO_x	47	873	ppm
	Relative air/fuel ratio (λ)	0.856	1.124	
Output	Case type code	1	15	

The output data is one parameter assumed arbitrarily. This vector represents the case type code. Each code in this vector refers to the selected cases (normal case and faulty cases) as shown in Table 2. Therefore, the nodes in the input layer and output layer are (6) and (1), respectively.

Table 2: Case Type and Code

<i>Case Type</i>		<i>Code</i>
No Problems		1
Faulty Cases	Bad oil	2
	No air cleaner used	3
	Dusty air cleaner	4
	Removed evaporated oil tube	5
	Gap of the spark plug is small	6
	Gap of the spark plug is large	7
	Carburetor main jet is 33 % blocked	8
	Carburetor main jet is 66 % blocked	9
	Leak in inlet valve	10
	Leak in exhaust valve	11
	Crack in tailpipe	12
	Gasket is crushed	13
	Exhaustion of the piston rings	14
	A problem in cooling system	15

In this study the network is tested with one and two hidden layer configurations with an increasing number of nodes in each hidden layer(s). Different activation function arrangements are investigated. The optimal topology is determined first by using one hidden layer with activation function as hyperbolic tangent (*tansig*) function for hidden and output layers.

Different numbers of nodes from (7 to 26) are investigated and the training performance and correlation coefficient for both training and testing dataset of these topologies are shown in Figs. 4 and 5. From these figures the network with (16) nodes in the hidden layer gives best performance and correlation coefficient than other.

Then two hidden layers are used with different activation functions for both first hidden layer, second hidden layer and output layer. Different node numbers in each hidden layer from (3 to 14) nodes are used. The performance and regression of these topologies of network for both training and testing are shown in Figs. 6 and 7. From these figures the network with (9 nodes in the first and 7 nodes in the second hidden layer) gives best performance and

regression for both training and testing than other. The results show that a network with two hidden layers is significantly better than that with one hidden layer. Fig. 8 shows the comparison between the training and testing performance for the best one hidden layer network (16 nodes) and the best two hidden layer network (9,7 nodes). From this figure, it can be seen that the network (9-7) gives best performance and regression for both training and testing. The configuration of the ANN is shown in Fig. 9. The choice of the training function depends on the network application. Three types of training function are used in the neural networks modeling of the present study. Although, using *Traincgp* algorithm might be sufficient in solving many functional approximation problems, some other problems may be easier to be solved with *Traingdm* or *Trainrp* training function.

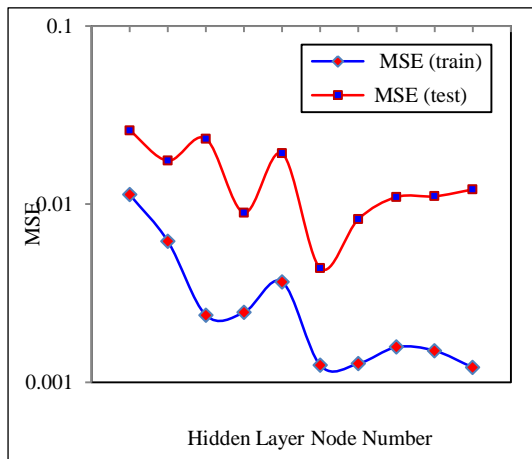
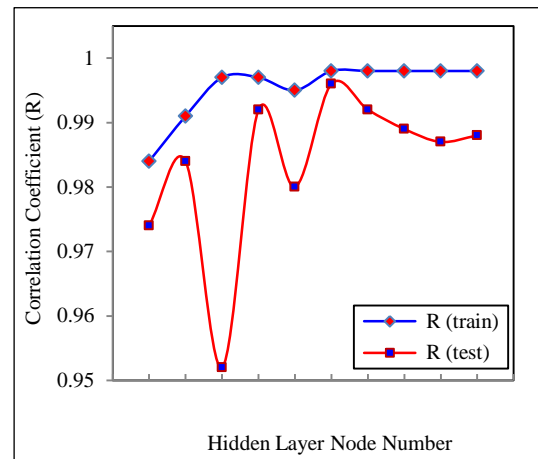
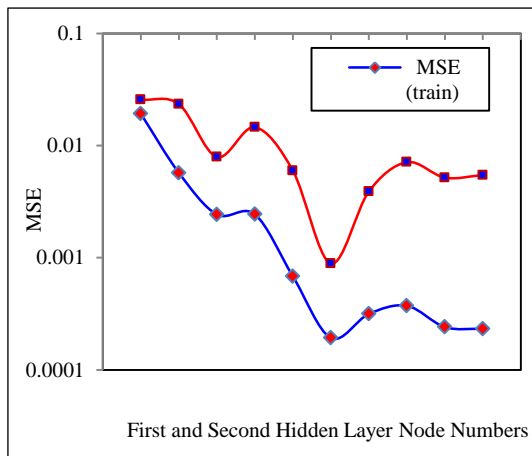
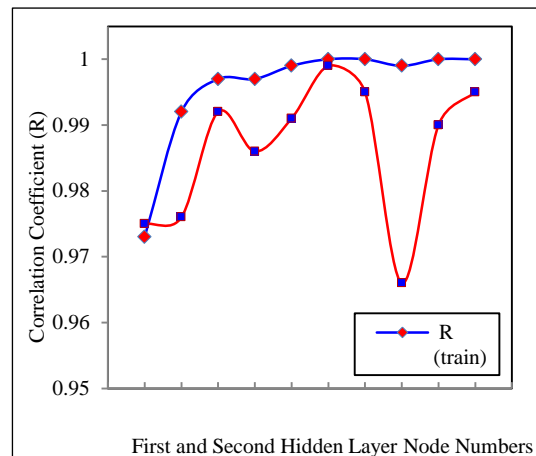
7. Proposed Network

From the above analysis, for different arrangements of neural networks it can be seen that (*Traincgp*) training function with (*tansig*) activation functions for the two hidden layers and output layer gives the best MSE and correlation coefficient for both training and testing than other. Therefore, this network can be selected as a proposed network for the present study. Table 3 and Fig. 10 show the comparison between the best different algorithms for network model. Fig. 11 shows training and testing performance of the proposed neural network.

The performance of a trained network can be measured to some extent by the errors on the training and testing sets, but it is often useful to investigate the network response in more detail. One option is to perform a regression analysis between the network response and the corresponding targets. Figs. 12 and 13 show the regression analysis between the output of neural network and the corresponding target for training and testing data respectively. In the figures, outputs are plotted versus the targets as open circles. The solid line indicates the best linear fit and the broken line indicates the perfect fit (output equals target). The values of the slope are (0.996) and (0.99) respectively, interceptions with y-axis are (0.0282) and (0.129) respectively, and correlation coefficients are (1) and (0.999) respectively. These values indicate that the mapping of neural network for the training and testing data is very good. Fig. 14 shows the graphical user interface operating mode for fault diagnosis model, it is coded using *Microsoft Visual Studio (2010)*.

Table 3: MSE and Regression of Three Different Algorithms for Network Model

<i>Training Function</i>	<i>MSE (train)</i>	<i>MSE (test)</i>	<i>R (train)</i>	<i>R (test)</i>
<i>Traindm</i>	0.00569	0.01438	0.992	0.985
<i>Traincgp</i>	0.00019	0.00088	1.000	0.999
<i>Trainrp</i>	0.00077	0.00361	0.999	0.996

**Fig. 5: Regression of Network with One Hidden Layer****Fig. 4: Performance of Network with One Hidden Layer****Fig. 6: Performance of Network with Two Hidden Layers****Fig. 7: Regression of Network with Two Hidden Layers.**

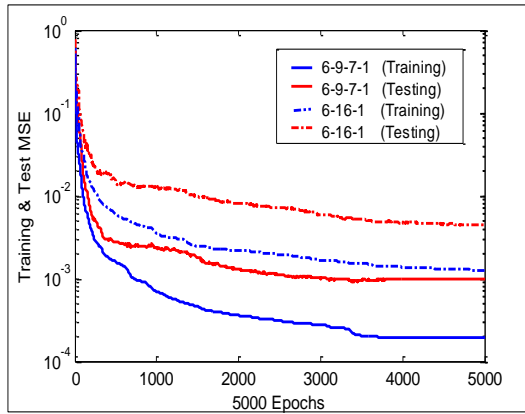


Fig. 8: Compare between One and Two Hidden Layers Performance

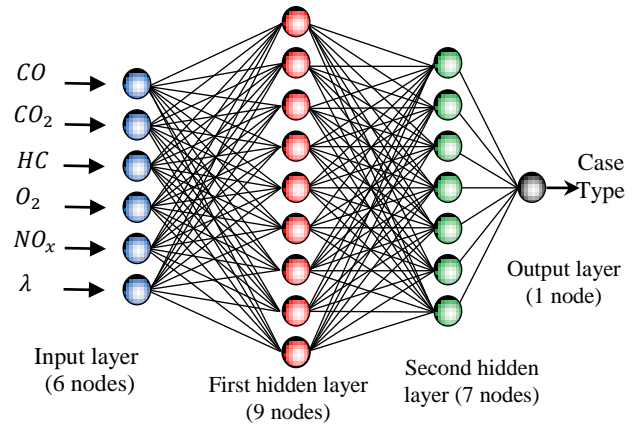


Fig. 9: Configuration of Neural Network (6-9-7-1)

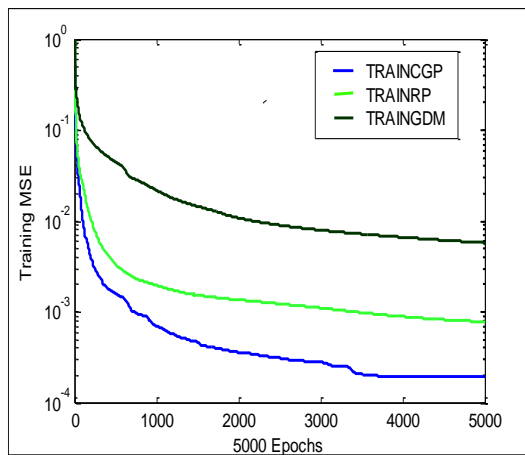


Fig. 10: Compare between the Best Three Types of Network Performance

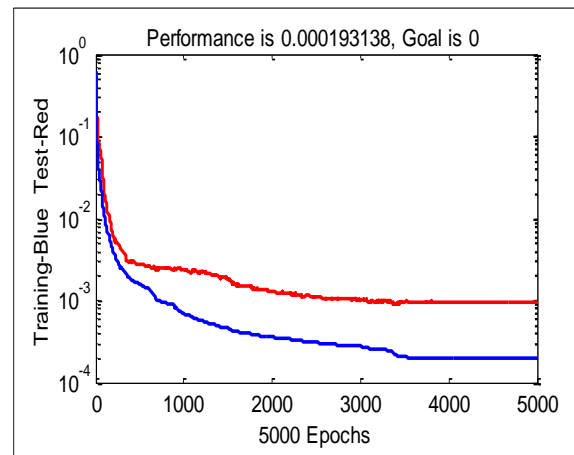


Fig. 11: Training and Testing MSE vs. Epochs of the Proposed Neural Network

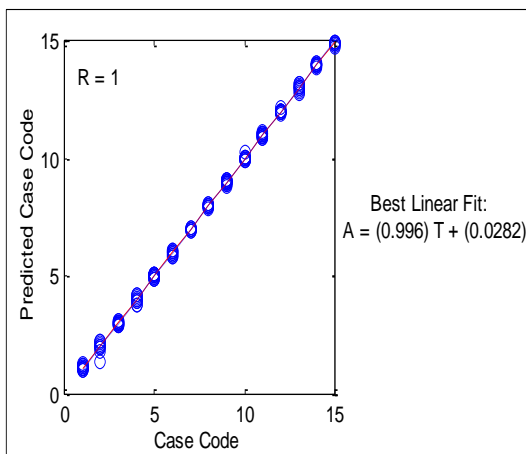


Fig. 12: Training Regression of the Proposed Network

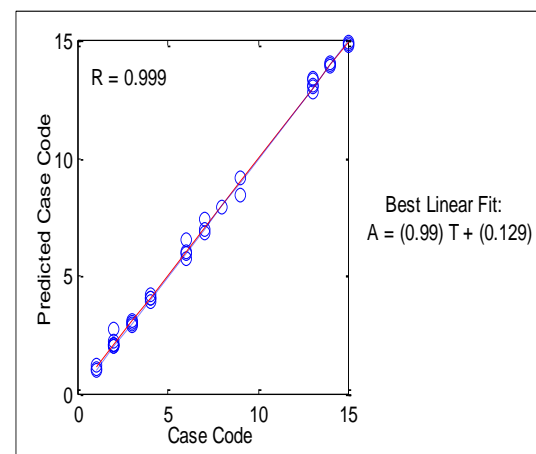


Fig. 13: Testing Regression of the Proposed Network

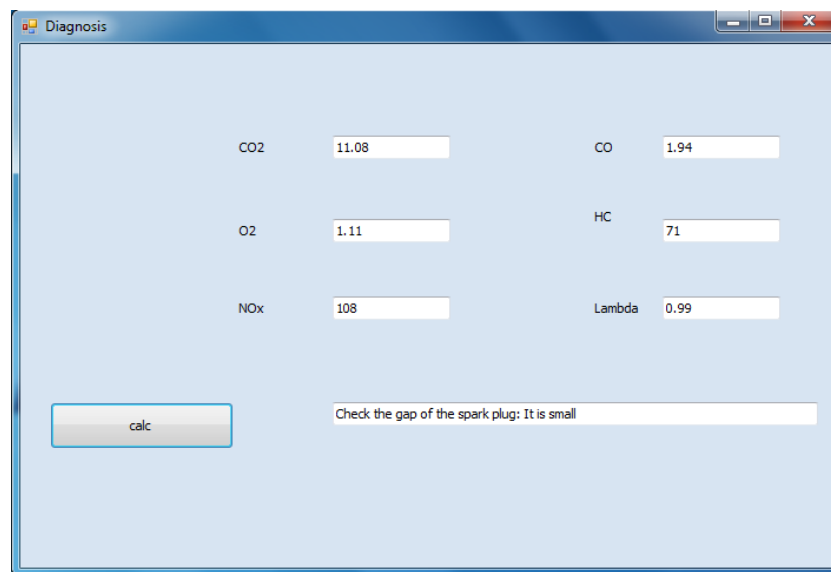


Fig. 14: Graphical User Interface Using Visual Basic Program

8. Conclusion

The most important conclusions that can be drawn from the present study are the followings:

1. Exhaust gas analysis of an Internal Combustion engine plays a significant role in fault diagnosis under various loading conditions.
2. The multilayer (two hidden layers) feed forward neural network model, rather than single hidden layer, significantly improves performance of network. The configuration (9-7) is proved to be very efficient for diagnosing different engine faults using its emissions.
3. The number of hidden layers, the number of nodes in the hidden layers, the arrangement of activation function and the type of training function had significant effects on the performance of the ANN models.
4. Type and arrangement of activation function affect the response of network. The $[tansig, tansig, tansig]$ activation function is found to give a minimum mean square error and maximum regression for the most investigated networks.
5. The conjugate gradient back propagation with Polak-Ribiere updates (*Traincgp*) algorithm gives best performance and regression for both training and testing phases better than the other training algorithms.

References

- [1] Frank, P. M. , 2002, “Handling Modeling Uncertainty in Fault Detection and Isolation systems”, Journal of Control Eng. and Applied Informatics, Vol. 4, No. 4, pp. 29-46.
- [2] Zhang, Y. M. and Li, X. R. 1998, “Detection and diagnosis of sensor and actuator failures using IMM estimator”, Journal of AES, Vol. 34, No. 4, pp.1293-1312, Oct.
- [3] Svard, C., 2009, “Residual Generation Methods for Fault Diagnosis with Automotive Applications”, Thesis No. 1406, Electrical Engineering, Linkoping University, Sweden.
- [4] Rengaswamy, R., et al, 2003, “A Review of Process Fault Detection and Diagnosis Part I: Quantitative Model-based Methods”, J. of Comp. and Chem. Eng., Vol. 27, pp. 293-311.
- [5] Gadoue, S. , 1998, “Artificial Neural Networks”, EEE 8005 - SDL Industrial Automation Lecture Notes, Newcastle University, School of Electrical, Electronic & Computing Eng.
- [6] Jha, G. K., 2007, “Artificial Neural Networks”, Journal of Indian Agricultural Research Institute, PUSA, New Delhi, 110-12, pp. 1-10.
- [7] Jha, G. K., 2007, “Artificial Neural Networks and Its Applications”, Journal of Indian Agricultural Research Institute, New Delhi, 110-012, pp. 41-49.
- [8] Demuth, H., Beale, M. and Hagan, M., 2006, “Neural Network Toolbox User’s Guide Ver5”, The Math works, Inc., Natick, MA, USA.
- [9] Haykin, S., 1999, “Neural Networks - A Comprehensive Foundation”, Second Edition, Prentice Hall, Indian Branch.
- [10] Verma, B., “Fast Training of Multilayer Perceptrons”, Proceedings of IEEE & IASTED, School of Information Technology, Griffith University, Gold Coast, Queensland, Australia.
- [11] Jain, A. K., Mao, J. and Mohiuddin, K, 1996, “Artificial Neural Network: A Tutorial”, Journal of IEEE Computer, Vol. 29, No. 2, pp. 31-44.
- [12] Gullu, M., et al, 2011, “Application of Back Propagation ANN for Modeling Local GPS/Leveling Geoid Undulations”, Geoid and GNSS Heighting, Turkey.
- [13] Rumelhart, D. and McClelland, J., 1986, “Parallel Distributed Processing”, MIT Press, Cambridge, Mass.
- [14] Jain, A. K., Mao J. and Mohiuddin K. M., 1996, “Artificial Neural Networks: A Tutorial”, Journal of IEEE, 0018-9162/96, pp. 31-44.
- [15] Hema, C. R. et al., 2007, “Motor Imagery Signal Classification for a Four State Brain Machine Interface”, International J. of Biological and Life Sci., Vol. 3, No. 1, pp. 76-81.
- [16] Astra Korea Company, “Gasoline Generator”, AST11770, Operation Manual.

List of Abbreviations and Symbols

<i>Symbol</i>	<i>Description</i>
a	Actual output
ANN	Artificial Neural Network
b	Bias value
BP	Back-Propagation
EBP	Error Back-Propagation
f	Activation function
FDI	Fault Detection and Isolation
FL	Fuzzy Logic
GA	Genetic Algorithms
MLP	Multi-Layer Perceptron
MSE	Mean Squared Error
p	Input signal
PCA	Principal Component Analysis
PLS	Partial Least Squares
pn	Normalized value of input signal
QTA	Qualitative Trend Analysis
R	Correlation coefficient
RPM	Revolution Per Minute
s	No. of training examples
t	Desired output (Target)
v	The difference between the target and the output
w	Weight value
δ	Back propagation error
λ	Stoichiometric or normalized Air to Fuel Ratio
μ	Momentum coefficient
τ	Time step
η	Learning rate parameter

List of Subscripts

<i>Symbol</i>	<i>Description</i>
i	No. of input parameters or species
j	No. of neurons of first layer
k	No. of neurons of second layer
l	No. of neurons of output layer

Perspective the Use of Thermal Energy Lost From an Engine Cooling System to Run an Absorption Refrigerator for Vehicle Air Conditioning

Asst. Prof. Dr. Abdulwadood Salman Shihab,

Technical College of Basrah
E-mail: wadsal54@yahoo.com

Abstract:

This paper is addressed to investigate the possibility of using a waste heat to drive absorption refrigeration system as an alternative system for automobile air conditioning. LiBr-water absorption refrigerator is suggested for this application. A theoretical analysis of the system has been carried out to maximize its cooling potential. This study includes also an actual experimental test to measure the available waste heat that is rejected from water cooling system of a 6-cylinder petrol engine fitted to Toyota Land Cruiser vehicle. The test was performed directly on the vehicle using out-city high way roads. It is found that the wasted energy from the engine cooling system is ranged between 10 kW for idling engine speed and 68 kW when loading. The engine cooling water temperature is ranged between 71 °C and 84 °C. The reject heat available in the cooling water system is measured and found to be adequate for producing cooling up to 34 kW, but the low level of the water temperature did not allow the refrigeration system to produce continuous cooling corresponding to engine and vehicle speeds at a refrigeration temperature of 5 to 10 °C, especially at hot weather condition.

Keywords: Alternative Vehicle Air-conditioning, Absorption Refrigerator.

المستخلص

يتناول هذا البحث التحقق من إمكانية استخدام الطاقة الحرارية المفقودة من محركات المركبات لاستخدامها كمصدر لتشغيل منظومة تبريد امتصاصية لأغراض التكييف كنظام بديل. اقترحت منظومة التبريد الامتصاصية ماء -بروميد الليثيوم لهذا التطبيق. تم انجاز تحليل نظري للمنظومة للحصول على أفضل أداء. احتوت الدراسة أيضا على تنفيذ اختبار عملي لقياس الطاقة الحرارية الفعلية المتاحة والمطروحة من منظومة تبريد محرك بنزين ذو ستة اسطوانات لسيارة نوع تويوتا لاندكروز حيث اجري الاختبار العملي على السيارة مباشرة واختبرت الطرق الخارجية لهذا الغرض. لقد وجد أن الطاقة المطروحة من منظومة تبريد محرك السيارة تتراوح بين 10 كيلووات عندما يعمل المحرك بدون تحميل إلى 68 كيلووات مع التحميل. تراوحت درجة حرارة ماء تبريد محرك السيارة بين 71 إلى 84 درجة مئوية. تم حساب الطاقة الحرارية المفقودة من مشع منظومة تبريد المحرك وظهرت إنها وافية لإنتاج التبريد بما يعادل 34 كيلووات، ولكن المستوى المنخفض لدرجة حرارة الماء قيدت عملية إنتاج التبريد بصورة مستمرة بدرجات حرارة تبريد 5 إلى 10 درجة مئوية وخاصة في الأجواء الحارة.

1- Introduction:

The air conditioning systems currently utilized in automobiles are the vapor compression systems. This type of system has many disadvantages: the refrigerant used is not environmentally friendly, the compressor is in competition with the engine coolant system, and the compressor uses a significant portion of the engine power. To date, almost all car air-conditioning systems are charged with R-134a. However, alternatives with lower global warming impact than R-134a are desirable.

It is a well-known fact that a large amount of heat energy associated with the automobiles engine cooling system and with the exhaust gases are wasted. A rough energy balance of the available energy in the combustion of fuel in a motor car engine shows that one third is converted into shaft work, two third is lost to atmosphere [1].

A waste heat driven absorption refrigeration system is one alternative to the current systems. The absorption refrigeration system (ARS) uses solutions for the absorbent-refrigerant pair that do not harm the environment. Recently, there has been increasing interest in the industrial and domestic use of the ARSs for meeting cooling and air conditioning demands as alternatives. The most widely used refrigerant and absorbent combinations in ARSs have been ammonia–water and lithium bromide–water. The lithium bromide–water pair is available for air-conditioning and chilling applications (over 4°C, because of the crystallization of water). Ammonia–water is used for cooling and low-temperature freezing applications (below 0°C) [2].

The main drawback of absorption systems for cars is the heating-up time needed to create the temperature level necessary in the boiler to produce refrigerant vapor. This system therefore needs a refrigerant storage as well as a minimum operating time of about half an hour before efficient cooling operation [3].

Akerman, 1969 [4], thermally analyzed three cycles of an automotive absorption air conditioning system that would use engine-rejected heat. The three cycles were based on using water–lithium bromide, ammonia–water and Refrigerant 22–Di methyl form amid of tetra ethylene glycol (R22–DMFTEG) as a refrigerant–absorbent pairs. He concluded that; due to the number of additional parts required, the large size of the required heat transfer surface of the heat rejection devices and the large amount of heat energy required, the absorption refrigeration system is not suitable for use in automotive air conditioning.

Wang, 1997 [5], showed that even for a relative small car-engine, such as for the Nissan1400, 15 kW of heat energy can be utilized from the exhaust gases. This heat is enough to power an aqua-ammonia absorption system to produce a refrigeration capacity of 5 kW.

The studies by Horuz (1998, 1999) [6], [7] utilized waste heat from the vehicle engine exhaust gas as the sole driving mechanism for his proposed absorption refrigeration systems, he demonstrated that a vapor absorption refrigeration system running on a diesel engine is indeed possible and he concluded that engine exhaust gas heat would provide sufficient power to drive his proposed systems during normal cruise conditions (engine speeds around 2000 rpm), but would not provide sufficient capacity at rest (idle) or at slow-moving traffic conditions. Horuz pointed out the limitations imposed by exhaust gas back pressure on the engine and the effects of corrosive exhaust gases that could condense within exhaust system components as a result of extracting heat from the exhaust gases.

Boatto et al. 2000 [8], conducted extensive measurements on the exhaust system of a 2.0-liter, four-cylinder, spark-ignition engine of mid-sized passenger cars. They concluded that an automotive absorption refrigeration system driven by exhaust heat recovery allows for considerable power recovery and seems feasible as long as provisions are made to store liquid refrigerant (water) for use during transient startups and when temporary exhaust gas power deficits occur.

Shannon, 2005 [9], concluded that the absorption refrigeration system with LiBr-Water mixture is a feasible alternative to the traditional vapor compression system for automotive case, a typical 3-liter, 4 stroke carbureted engine was used. In order for the system to run at the most favorable conditions, the outside air temperature needs to be below 38°C which can be a problem in places with extremely high temperatures. The minimum generator temperature should be around 93°C. Ideally, the system will work best if the motor is running at 115.5°C. Also the condenser temperature must be below 55.5°C. The absorption refrigeration system would work for temperatures out of the above mentioned ranges, but the efficiency drops off rather drastically.

Vicatos, 2008 [10], used energy from the exhaust gas of an internal combustion engine to power an absorption refrigeration system to air-condition an ordinary passenger car. The theoretical design is verified by a unit that is tested under both laboratory and road-test conditions. The unit was installed in a Nissan 1400 truck and the results indicated a successful prototype and encouraging prospects for future development. The low coefficient of performance (COP) value is an indication that improvements to the cycle are necessary.

Apart from the limitations imposed by exhaust gas, the present work proposes the reject heat that available in the vehicle engine cooling water system to be used as the driving thermal energy to operate LiBr-Water absorption refrigeration system for the purpose of air-conditioning the passenger compartment.

2- Theoretical analysis

An absorption system is a heat-operated refrigerator. It consists four basic components; an evaporator and an absorber which are located on the low pressure side of the system, and a generator and a condenser which are located on the high pressure side of the system.

The absorption cycle (Figure 1), can be divided into three distinct parts. *The water side* is a vapor/compression cycle through which the compressed water vapor out of the generator-separator assembly is cooled and condensed in the condenser. It is then expanded through the expansion valve and evaporated in the evaporator, producing cooling in the passenger compartment. Upon exiting the evaporator, the water vapor enters in to *the LiBr-Water side* of the device. When the water vapor comes in contact with the rich solution (rich in LiBr) in the absorber, the vapor is rapidly dissolved, or absorbed into the fluid producing heat that must be dissipated out of the absorber. The produced weak solution at the exit of the absorber then is driven by a small liquid pump toward the *desorption chamber* (vapor generator). Between the absorption and desorption chambers heat is exchanged to raise the temperature of the weak solution via preheating heat exchanger. In the desorption chamber, due to heat addition, the water is desorbed from the solution and librated as a vapor at a higher temperature. The rich solution out of the vapor generator is then cooled at the preheating heat exchanger and then back to its original temperature in the absorber.

The schematic diagram of the proposed LiBr-Water absorption refrigeration system is shown in Fig. (1). The corresponding points numbers of this figure are also presented on the pressure-temperature-concentration (P-T- ζ) diagram of LiBr-Water solution Fig.(2), and on the pressure-enthalpy (P-h) diagram of pure water as in Fig.(3).

The LiBr-Water solution properties and that of pure water at different pressures, temperatures and concentration can be obtained from property data and their correlations which are available in [11].

The proposed system is powered by the heat energy rejected from a variable speed internal combustion engine (the hot water of the engine cooling system). The amount of the rejected heat through the vehicle radiator Q_{rad} is;

$$Q_{rad} = \dot{m}_w C_p (T_{w,in} - T_{w,out}) \quad (1)$$

$T_{w,in}$, $T_{w,out}$ Are the engines cooling water temperatures at the inlet and outlet of the radiator,
 \dot{m}_w , Engine cooling water flow rate.

Referring to Fig. (1) to Fig.(3), the steady flow analysis is carried out by applying the mass and energy balance across the evaporator and the generator with the following assumptions:

- 1- Perfectly insulated components.
- 2- No superheating in the evaporator, nor sub-cooling in the condenser.
- 3- The circulating pump of the weak solution is assumed to be of a variable capacity, then the weak mixture flow rate (\dot{m}_{ws}) that is pumped to the vapor generator is:

$$\dot{m}_{ws} = G * N \quad (2)$$

G = variable chosen based on the temperature level through the generator such that it satisfies the generator energy balance, equations (5) and (11).

N = Engine speed (rpm).

- 4- Assuming that the generator temperature ($T_g = T_4 = T_7$) is 5°C less than the engine hot water temperature (the minimum temperature difference between two fluids exchanging heat energy or “pinch point”) [12];

$$T_4 = T_{w,in} - 5 \quad (3)$$

And the weak solution can be preheated through the preheating heat exchanger to a temperature (T_3) with a pinch point of 5°C (below the generator temperature) ;

$$T_3 = T_4 - 5 \quad (4)$$

- 5- It is assumed that the generator can absorb at least 50% of the available radiated heat energy;

$$Q_g = 0.5 Q_{rad} \quad (5)$$

The effectiveness (ϵ) of the preheating heat exchanger is assumed to be 0.5.

When the heat exchanger cost is an important consideration, most heat exchangers are designed in the approximate value of $\epsilon \leq 60\%$, [13]

$$\epsilon = \frac{T_g - T_5}{T_g - T_3} \quad (6)$$

Considering the control volume of the generator and applying mass balances, then the strong solution mass flow rate \dot{m}_{ss} is;

$$\dot{m}_{ss} = \dot{m}_{ws} - \dot{m}_v \quad (7)$$

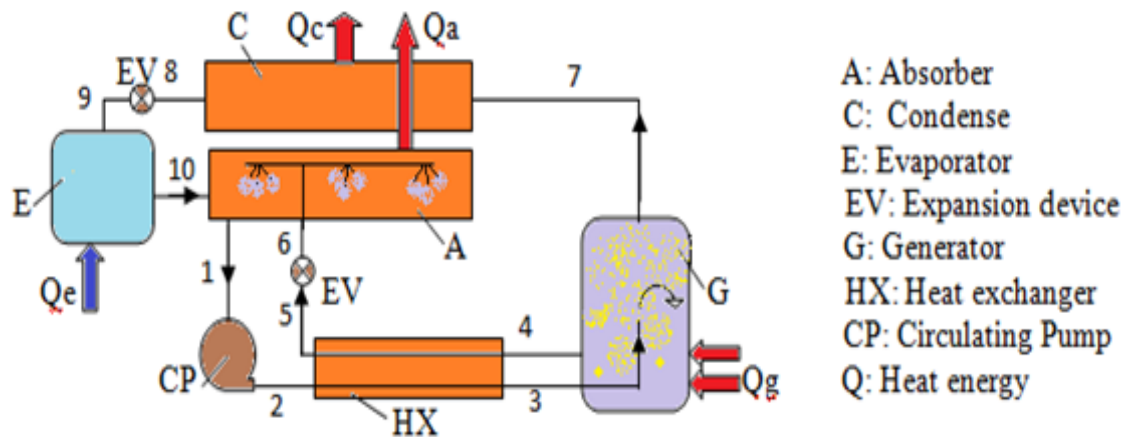


Fig. (1). The schematic diagram of the proposed LiBr-Water absorption refrigeration system

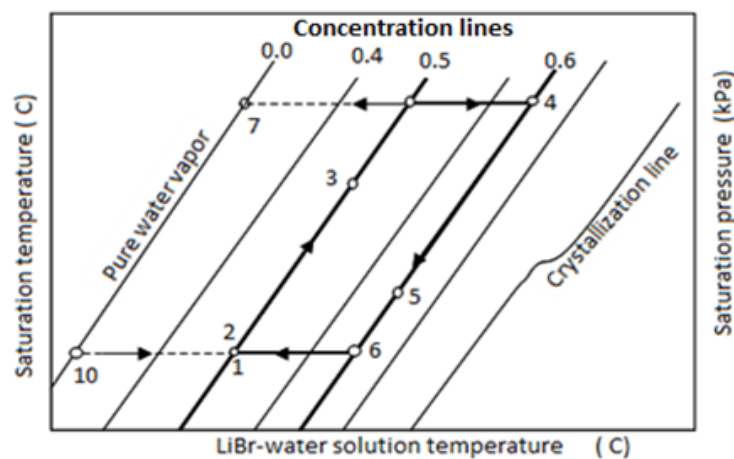


Fig. (2). Pressure-Temperature-Concentration diagram of the Proposed cycle (Dühring Chart)

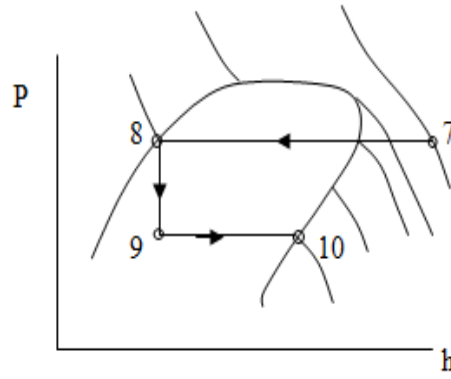


Fig. (3). the pressure-enthalpy (P-h) diagram of pure water

For the employed solution, the mass fraction (ξ) (LiBr concentration) is defined as the ratio of mass of anhydrous lithium bromide to the total mass of solution.

Applying mass balance for LiBr through the generator, the vapor mass flow rate \dot{m}_v can be evaluated as;

$$\dot{m}_v = \dot{m}_{ws} \frac{\xi_{ss} - \xi_{ws}}{\xi_{ss}} \quad (8)$$

ξ_{ss} , ξ_{ws} are the strong and weak solution concentrations which are functions of temperature and pressure at the generator and the absorber respectively.

$$\xi_{ss} = \xi(T_g, P_c), \quad \xi_{ws} = \xi(T_a, P_e) \quad (9)$$

The dominated high pressure at the generator (P_g) is as that of the condensing pressure (P_c) and the dominated low pressure at the absorber (P_a) is as that of the evaporator pressure (P_e);

$$P_g = P_c, \quad P_a = P_e \quad (10)$$

Applying energy balance through the vapor generator, the gained heat energy (Q_g) by the solution in the generator is as follows;

$$Q_g = \dot{m}_{ss} h_4 + \dot{m}_v h_7 - \dot{m}_{ws} h_3 \quad (11)$$

The cooling capacity of the system is a given by;

$$Q_e = \dot{m}_v (h_{10} - h_9) \quad (12)$$

Where h is the enthalpy at each corresponding point of the system cycle.

The coefficient of performance of the refrigeration cycle becomes:

$$COP = \frac{Q_e}{Q_g} \quad (13)$$

3- Experimental Test

This test is to measure the heat energy available within the engine cooling water system. This energy is rejected to the atmosphere via radiator. The water flow rate and its temperature vary considerably with the engine and vehicle speed.

Two sets of tests has to be done; one for the stationary vehicle (Idling speed), and the second for cruising condition (with engine road loading), at varying speed.

The tested vehicle is Toyota Land Cruiser car fitted with six cylinders petrol engine. The heat energy radiated out of the circulating cooling water of the engine Q_{rad} , is due to the temperature difference between the cooling water temperatures at the exit from the engine block $T_{w,out}$ (at the inlet to the radiator), and at the inlet to the engine block $T_{w,in}$ (at the outlet from the radiator).

The parameters to be measured are therefore; engine speed, vehicle road speed, cooling water temperatures at the inlet and outlet of the engine block, cooling water mass flow rate and the ambient temperature. These parameters are measured as in the following:

- a- Engine speed:** The fitted engine speed indicator (Engine speedometer) which is an electrical measuring device indicates the engine rpm by making use of the electrical pulses occurring at the ignition coil. When the vehicle is on the road, the vehicle speed can also be found simply by direct reading on the vehicle speedometer.
- b- Temperature measurements:** Calibrated Chromel-Alumel thermocouple wires are used to measure the water temperatures.
- c- Cooling water mass flow rate:** The water circulating pump used to circulate the engine cooling water is belt driven. Therefore, its pumping capacity is a function of engine speed and is independent of the idling or road load conditions. A venturi-meter is used to calibrate the pump in the laboratory using a suitable water flow circuit. The pump is placed in its position in the vehicle while it is still belt driven by the engine.

4- Results and discussion

5-1 Experimental results

Fig. (4) Shows the relations of the cooling water temperatures at inlet and outlet of the engine block and their difference, with engine speed for idling speed. The average hot water temperature out of the engine block is 71 °C at 500 rpm engine speed and 88 °C at 1050 rpm. The obtained correlation function for temperature difference is given by:

$$\Delta T_{w,idl} = 0.0061 * N + 3.6268 \text{ }^{\circ}\text{C} \quad (14)$$

Fig. (5) Shows the same relations as in Fig. (4) But for the condition when the vehicle is on the road load (Cruising condition). The average hot water temperature out of the engine block is 77 °C at 1000 rpm engine speed (40 km/hr Vehicle speed) and 84 °C at 2000 rpm (80 km/hr Vehicle speed). The obtained correlation function for temperature difference is given by:

$$\Delta T_{w,cr} = 0.002 * N + 5.87 \text{ }^{\circ}\text{C} \quad (15)$$

Fig. (6) Shows the results of the engine cooling water flow rate (\dot{m}_w) at different engine speed (N). The relation appears to be fairly linear. The obtained correlation function for these readings is:

$$\dot{m}_w = 0.001 * N - 0.1243 \text{ kg/s} \quad (16)$$

Fig. (7) Shows the calculated radiated heat energy (equation 1) at the vehicle radiator for both conditions, the idling and road load engine speeds. This amount of heat is ranged between minimum values of 10.5 kW at low idling speed to 68 kW at 2000 rpm cruising speed (80 km/hr).

5-2 Refrigeration system analysis results.

The present thermodynamic analytical model of LiBr-water absorption refrigeration system has been validated by comparing some of its results with the similar study that was done by Shanoon [9]. It can be seen from Table 1. that, the results of present model for reference data that were use by Shannon show the same general behavior for idling and road load speed.

**Table 1. Comparing the result of the present model (A) with reference [9]
(B) At $T_c = 54^\circ\text{C}$, $T_e = 7.2^\circ\text{C}$, $T_a = 37.8^\circ\text{C}$, for idling speed of 1000 RPM
And road load speed of 2000 rpm.**

	Speed, rpm.	T_g , $^\circ\text{C}$	Q_e , kW	Q_g , kW	Q_c , kW	COP
A	1000	92.2	4.92	11.	5.326	0.447
	2000	92.2	13.08	27.	13.98	0.484
B	1000	93.3	4.8	10.8	5.23	0.444
	2000	93.3	13.1	27.1	14.12	0.483

The governing equations of the proposed refrigeration system are solved to obtain the refrigeration system behavior at idling and road speeds with different operating conditions. The operating variable that affect the system performance are the condenser, absorber and the evaporator temperatures. The generator temperature is limited and is corresponding to the energy source temperature. The condenser and absorber temperatures are assumed to be the same as both, the condenser and the absorber are of air cooled heat exchangers type. This temperature is ranged to be from 35°C to 45°C . The evaporator temperature is ranged from 5°C to 21°C .

Due to the limited temperature of the energy source, increasing the solution flow rate through the vapor generator restrains the vapor production, so that the solution flow rate should be controlled to ensure quite temperature level of the flowing solution in the generator to liberate vapor according to the dominated pressure. It is also assumed that only 50% of the emitted heat energy that described in equation (1) can be absorbed by the working solution at the generator. Hence, the working solution circulating pump for this purpose should be of variable capacity (equation 2), such that the value of G is chosen by iteration to conform the evaporation requirements in the generator.

Figures (8) to (13) show the refrigeration system cooling capacity and its coefficient of performance at different condensing and evaporating temperature when the vehicle engine operates with no road load (idling condition).

Fig. (8) Illustrates that at a condenser-absorber temperature of 35°C , cooling can be produced at any evaporating temperature above 5°C even at low idling engine speed (500 rpm).

Most of the usual gasoline vehicles operate at 500 rpm engine speed or slightly more, but when using air conditioning system it needed to becomes more up to 1000 rpm.

Hence as shown in Fig.(8) an adequate cooling can be obtained (10-15 kW) with reasonably low evaporating temperature, 5 to 8 °C, the corresponding coefficient of performance in relation to 0.86 is illustrated in Fig.(9), that is when the engine rotate at 800 to 1000 rpm and a condenser-absorber temperature is of 35 °C. At higher evaporator temperature more cooling capacity with higher coefficient of performance can be obtained, that is because more vapor can be produced at higher evaporation temperature as the quantity $(\xi_{ss} - \xi_{ws})$ becomes more which is correspond to the amount of librated vapor (refrigerant).

Figs. (10) And (11) show how much the refrigeration performance is affected by the action of increasing the condenser-absorber temperature to 40°C.

Cooling can be produced at an evaporating temperature of 5 °C but at an engine speed more than 900 rpm, the effective cooling of about 6 kW is obtained at 970 rpm at which the coefficient of performance is 0.4.

To produce cooling at 8°C, the engine speed should be more than 850 rpm with an effective cooling capacity of 6 kW at 860 rpm with coefficient of performance of 0.45.

Further increase of the condenser-absorber temperature up to 45 °C lead to worse refrigeration performance as shown in Figs. (12) and (13). Cooling can never be produced at an evaporator temperature less than 14 °C even at an engine speed more than 1000 rpm.

It is evident that T_c and T_a have significant impact on the refrigeration system performance, that is due to the higher temperature level demands at the generator when increasing T_c , and the value of $(\xi_{ss} - \xi_{ws})$ becomes less at higher T_a .

Figures (14) to (18) show the refrigeration system cooling capacity and its coefficient of performance at different condensing-absorption and evaporating temperatures when the vehicle engine operates with road load (cruising condition).

Fig.(14) illustrates that at a condenser-absorber temperature of 35 °C, cooling can be produced at any evaporating temperature, 5 °C and more even at low vehicle engine speed of 40 km/hr (500 rpm engine speed). An adequate cooling can be obtained (11-13 kW) with an evaporating temperature of 5-14 °C, the corresponding coefficient of performance is in relation to 0.8 to 0.9 respectively as shown in Fig.(15).

The cooling capacity increases with vehicle speed due to an increase in the energy source temperature and so the vapor generation temperature. The cooling capacity decreases slightly with reducing the evaporator temperature.

The impact of reducing the evaporator temperature is obviously appointed on the coefficient of performance but this performance index interns improved with the vehicle

speed. At higher evaporator temperature more cooling capacity with higher coefficient of performance is obtained, that is because of more amount of librated vapor (refrigerant) as $(\xi_{ss} - \xi_{ws})$ becomes more.

Figs. (16) And (17) show how much the refrigeration performance is affected by the action of increasing the condenser-absorber temperature to 40°C. Cooling can be produced at an evaporating temperature of 8 °C but with vehicle speed more than 68 km/hr (1700 rpm engine speed). To produce cooling at 10°C, the vehicle speed should be not less than 52 km/hr (1300 rpm engine speed). At 40°C, continuous cooling at all vehicle road load speed can't be obtained at less than 12 °C evaporating temperature which is reasonably still acceptable for air conditioning with high cooling capacity. At this temperature the cooling capacity is ranged from 7 kW at 40 km/hr vehicle speed to 33 kW at 80 km/hr vehicle speed. The corresponding coefficient of performance is 0.47 to 0.84 respectively.

Further increase of the condenser-absorber temperature up to 45 °C leads to too worse refrigeration performance as shown in Figs. (19) and (20). Continuous cooling at all vehicle speeds can never be produced at an evaporator temperature less than 21°C. The cooling capacity at this temperature is ranged between 5.5 kW with COP of 0.38 to 33.5 kW with COP of 0.86 at vehicle speed of 40 km/hr and 80 km/hr respectively.

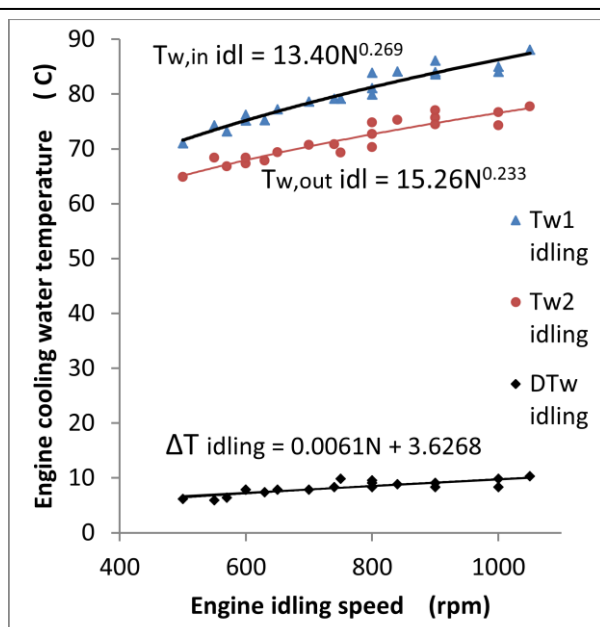


Fig. (4). The measured cooling water temperature at the inlet and outlet of the radiator verses engine idling speed.

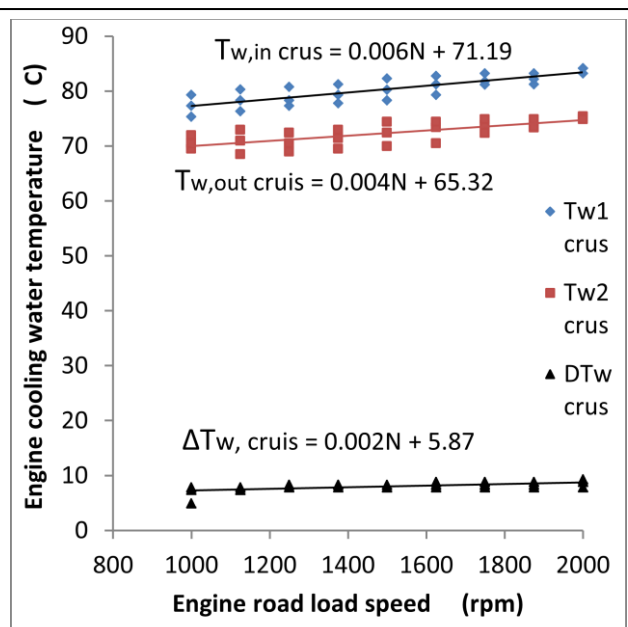


Fig. (5). The measured cooling water temperature at the inlet and outlet of the radiator verses engine road load speed.

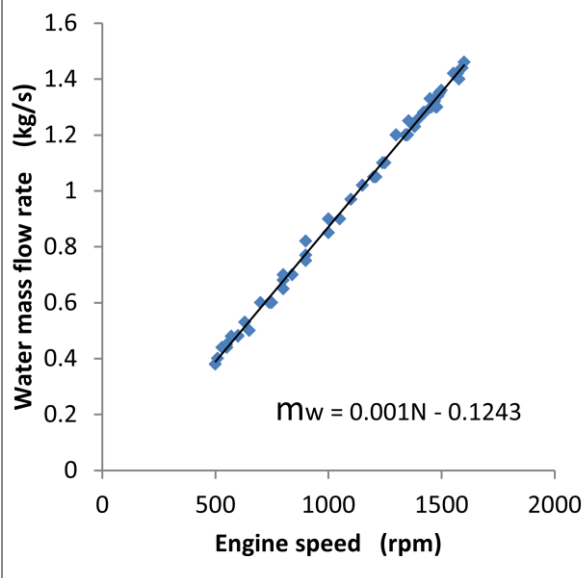


Fig. (6). The engine cooling water mass flow rate verses engine speed.

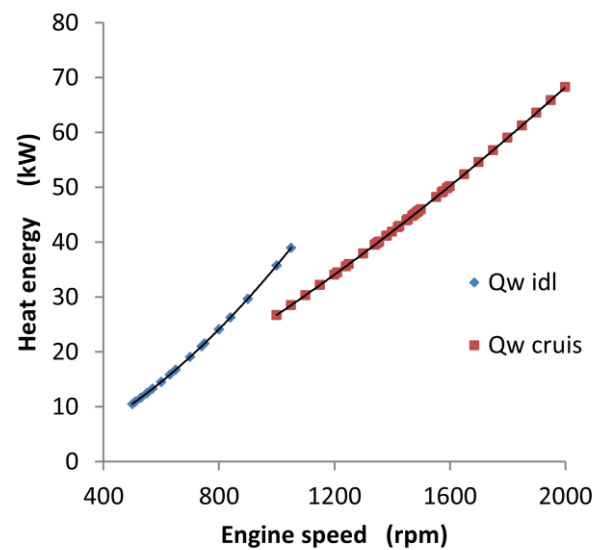


Fig. (7). The available heat energy that radiated from the engine cooling system to the surrounding for both idling and road load engine speed.

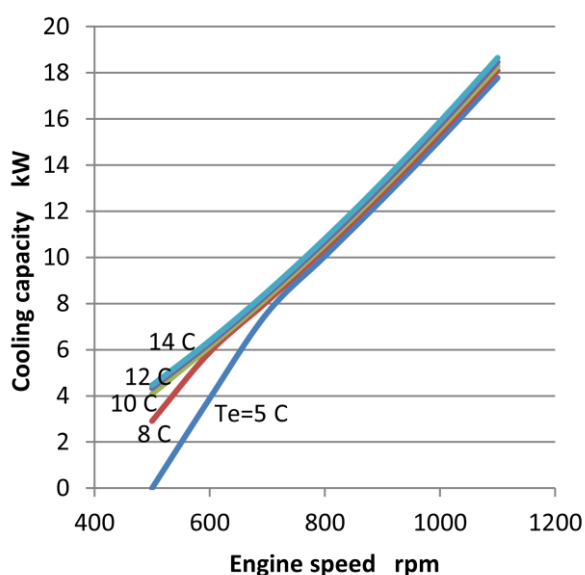


Fig. (8). Cooling capacity verses engine idling speed at $T_c=T_a=35$ C and different evaporating temperatures.

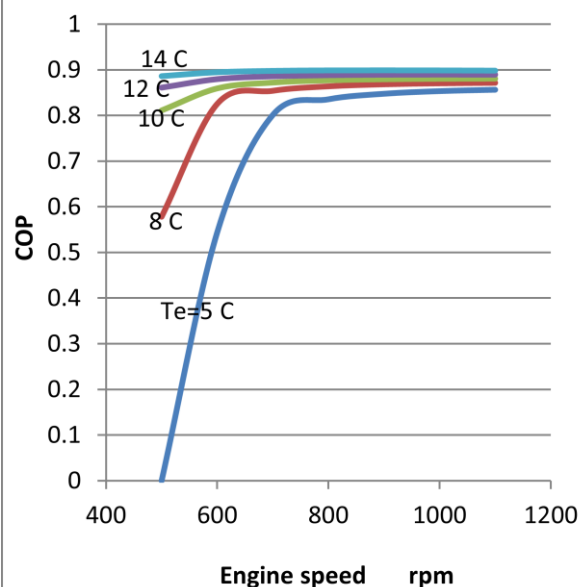


Fig. (9). Coefficient of performance verses engine idling speed at $T_c=T_a=35$ C and different evaporating temperatures.

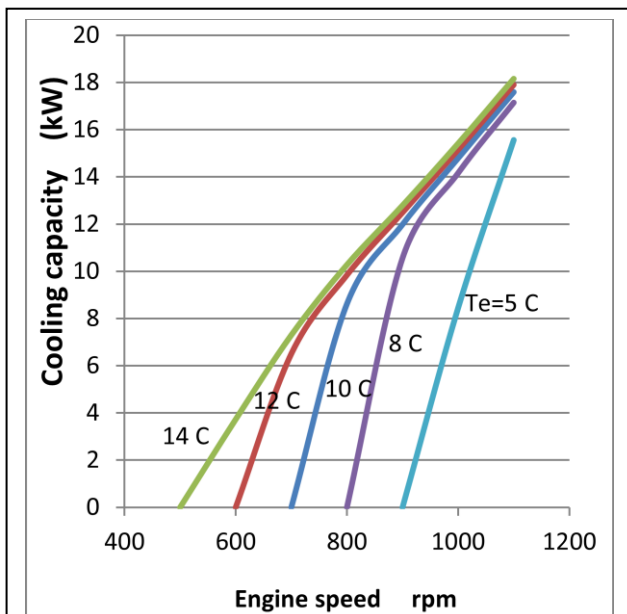


Fig. (10). Cooling capacity versus idling engine speed at $T_c=T_a=40$ C and different evaporating temperatures.

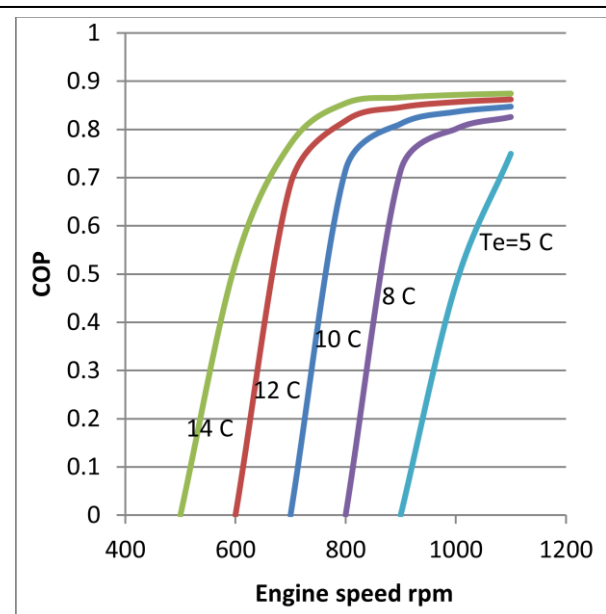


Fig. (11). Coefficient of performance versus idling engine speed at $T_c=T_a=40$ C and different evaporating temperatures.

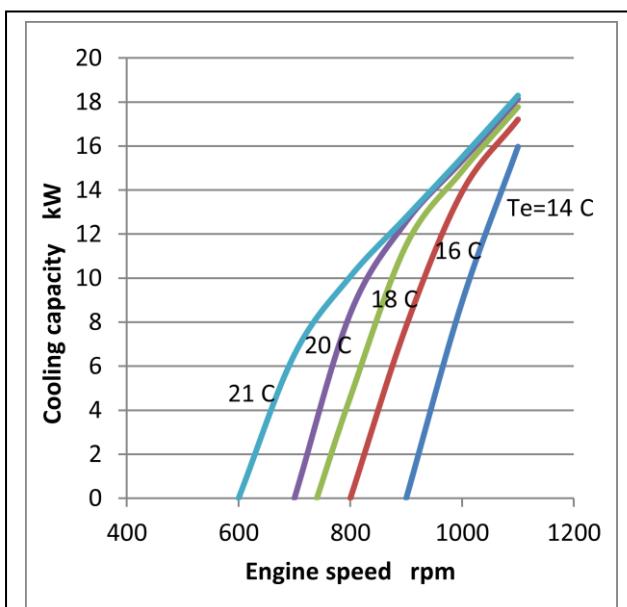


Fig. (12). Cooling capacity versus idling engine speed at $T_c=T_a=40$ C and different evaporating temperatures.

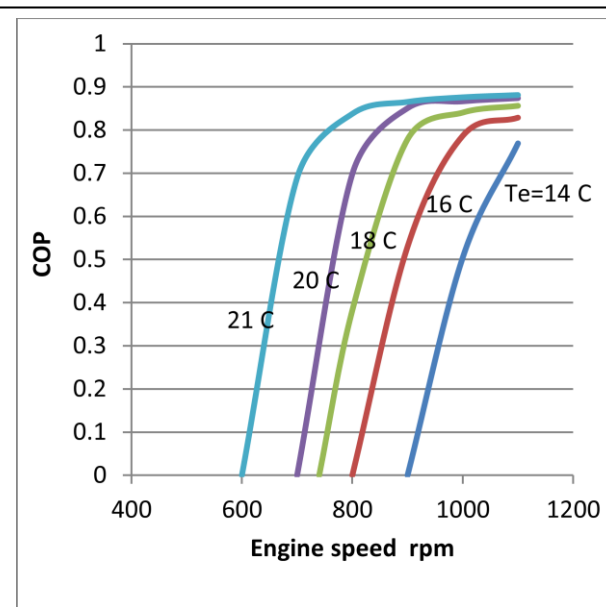


Fig. (13). Coefficient of performance versus idling engine speed at $T_c=T_a=45$ C and different evaporating temperatures.

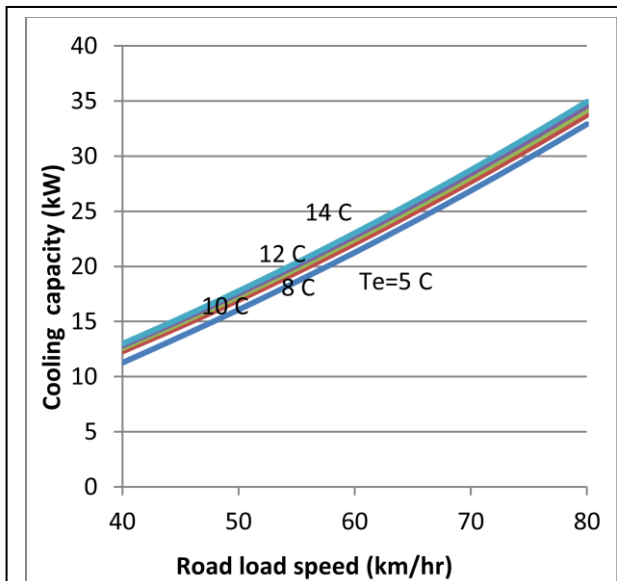


Fig. (14). Cooling capacity verses vehicle road load speed at $T_c=T_a=35$ C and different evaporating temperatures.

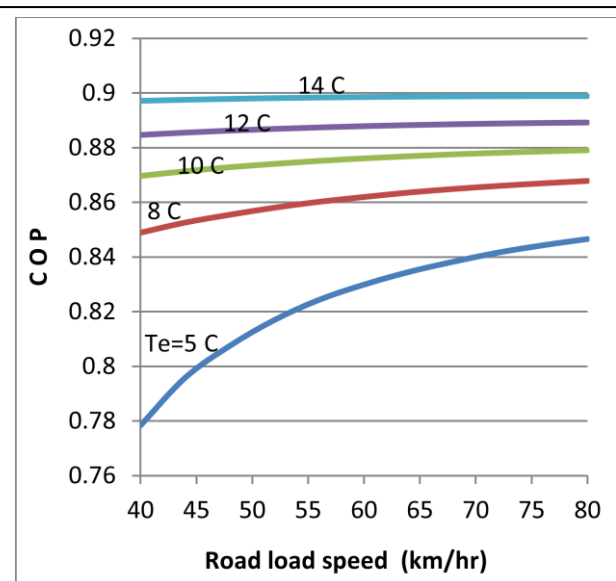


Fig. (15). Coefficient of performance verses vehicle road load speed at $T_c=T_a=35$ C and different evaporating temperatures.

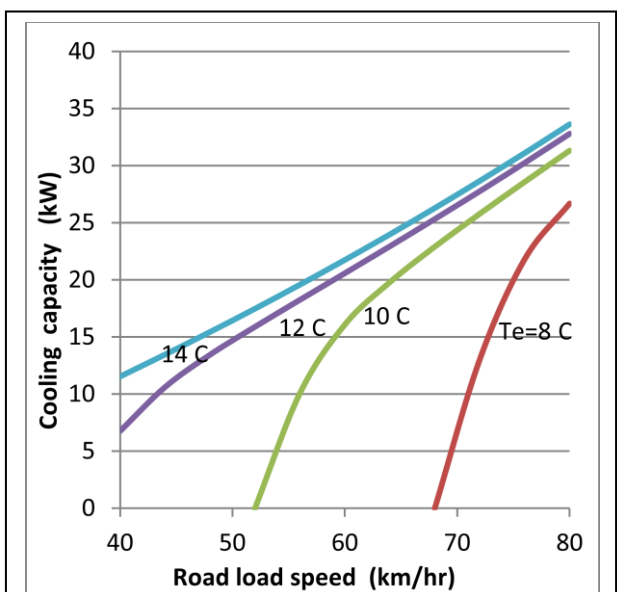


Fig. (16). Cooling capacity verses vehicle road load speed at $T_c=T_a=40$ C and different evaporating temperatures.

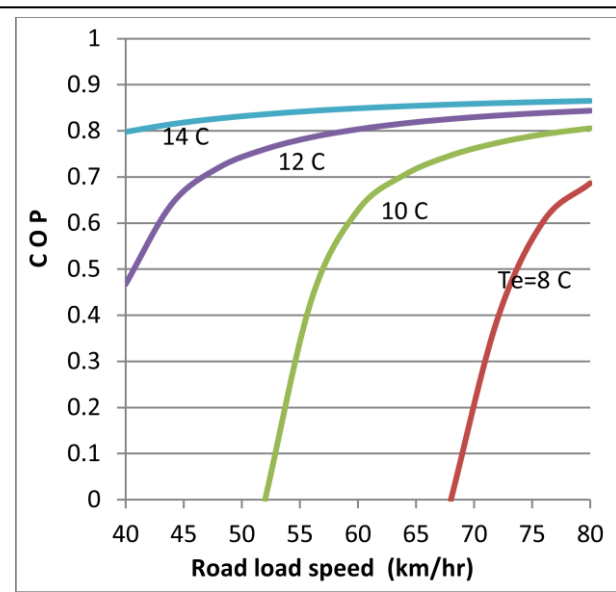


Fig. (17). Coefficient of performance verses vehicle road load speed at $T_c=T_a=40$ C and different evaporating temperatures.

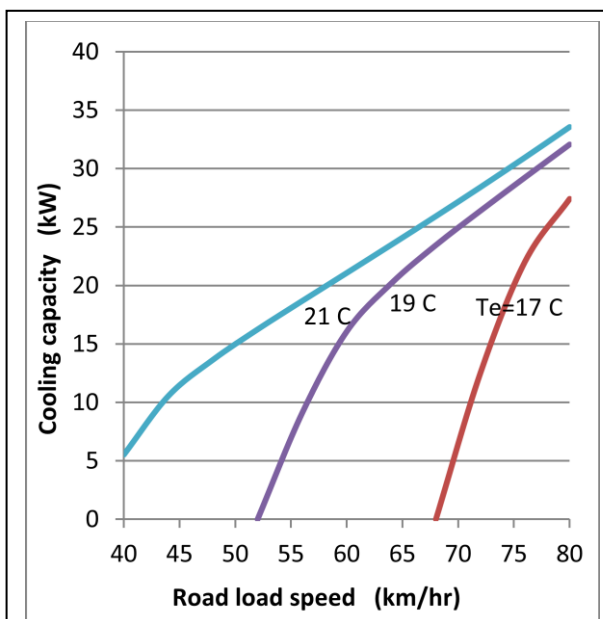


Fig. (18). Cooling capacity verses vehicle road load speed at $T_c=T_a=45$ °C and different evaporating temperatures.

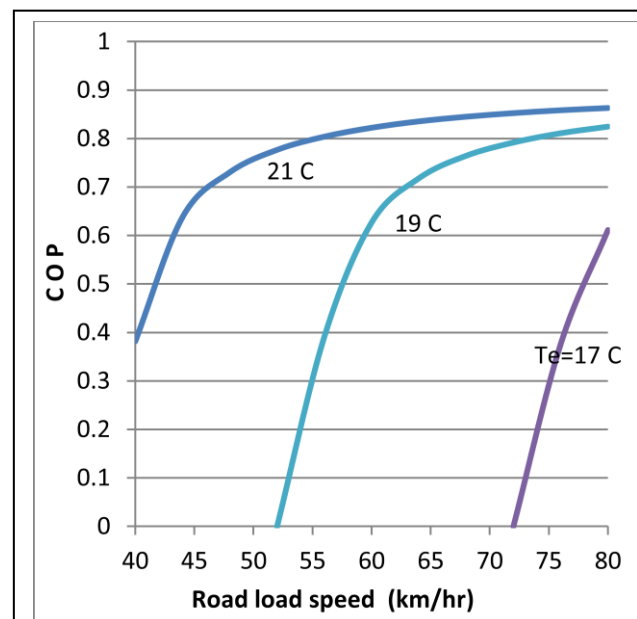


Fig. (19). Coefficient of performance verses vehicle road load speed at $T_c=T_a=45$ °C and different evaporating temperatures.

5- Conclusion

Demonstrating the above discussed figures of LiBr-Water refrigerator performance which is driven by the wasted energy of a vehicle cooling water system, it can be concluded that;

- 1- At idling speed, cooling can be produced at any engine speed but with different evaporating temperatures depending on the condenser-absorber temperature.
- 2- Continuous cooling of 9 to 16 kW at idling speed can be produced with condenser-absorber temperatures of 35 to 45 °C with an evaporating temperature of 10 °C or more when operating the engine at 1000 rpm. The COP is ranged between 0.5 to 0.87.
- 3- At road load speed, continuous cooling (11-13 kW) at all vehicle speeds and an evaporating temperature of 5-14°C, can be produced at low condenser-absorber temperature (35°C), and it is never be produced at an evaporator temperature less than 12 °C when the condenser-absorber temperature 40 °C and not less than 21°C when the condenser-absorber temperature is 45 °C and more which reasonably not suitable to achieve human comfort during hot days.

6- Recommendation

For the case of inadequate temperature level of the engine cooling water, it is recommended to preheat it by making use of fraction of the exhaust gas wasted energy through an indirect contact heat exchanger.

7- References

- [1] Greene A.B. and Lucas G.G. 1969 “The Testing of Internal Combustion Engines”, The English Universities Press.
- [2] Ibrahim Dinc, Mehmet Kanoğlu, 2010 “Refrigeration Systems and applications”. Second Edition, John Wiley & Sons, Ltd.
- [3] Boatto, P., Boccaletti, C., Cerri, G., Malvicino C, 2000 “Internal combustion engine waste heat potential for an automotive absorption system of air conditioning Part 1: tests on the exhaust system of a spark-ignition engine” *Proceedings of the Institute of Mechanical Engineers, Mississippi State*, Vol. 214, No. 8.
- [4] Akerman J. R., 1969 “Automotive air conditioning system with absorption refrigeration”. SAE Publication No.7100037, Chicago.
- [5] Wang S., 1997 “Motor vehicle Air-conditioning utilizing the exhaust gas to power an absorption refrigeration cycle”, MSc thesis, University of Cape Town South Africa.
- [6] Horuz, 1998 “Alternative road transport refrigeration,” *Turkish Journal of Engineering & Environmental Sciences*, Vol. 22, No. 3, pp. 211-222.
- [7] Horuz. I., 1999 “Vapor absorption refrigeration in road transport vehicles,” *Journal of Energy Engineering*, Vol. 125, No. 2, pp. 48-58.
- [8] Boatto, P., Boccaletti, C., Cerri, G., Malvicino, C., 2000 “Internal combustion engine waste heat potential for an automotive absorption system of air conditioning Part 2: the automotive absorption system,” *Proceedings of the Institute of Mechanical Engineers, Mississippi, State* Vol. 214, No. 8, , pp. 983-989.
- [9] Shannon Marie McLaughlin, 2005, “An Alternative Refrigeration System for Automotive Applications”; M.Sc thesis in Mechanical Engineering, Department of Mechanical Engineering Mississippi State.
- [10] G Vicatos, J Gryzagoridis, S Wang. 2008 “A car air-conditioning system based on an absorption refrigeration cycle using energy from exhaust gas of an internal combustion engine”, *Journal of Energy in Southern Africa*, Vol 19 No 4. November.

- [11] ASHRAE, 1998 “Refrigeration Handbook”, American Society of Heating, Refrigeration and Air-Conditioning Engineers.
- [12] Andrew Delano, 1998 “Design analysis of the Einstein refrigeration cycle”, PhD thesis, Georgia Institute of Technology.
- [13] Ramesh K. Shah, Dusan P. Sekulic, 2003 “Fundamentals of heat exchanger design”, Jone Wiley & Sons, Inc. New York

Nomenclature

<i>Symbols</i>	<i>Definition</i>	<i>Units</i>	<i>Symbols</i>	<i>Definition</i>	<i>Units</i>
A	Absorber		\bar{G}	Variable	
C	Condenser		HX	Heat Exchanger	
CP	Circulating pump		\dot{m}	Mass flow rate	Kg/s
C_p	Specific heat	kJ/kg.K	N	Engine speed	rpm
E	Evaporator		P	Pressure	Pa
EV	Expansion valve		\dot{Q}	Rate of heat energy	kW
G	Generator		T	Temperature	°C
ϵ	Heat Exchanger effectiveness		ξ	LiBr concentration in solution	

Subscripts

a	Absorber		rad	Radiation	
c	Condenser		ss	Strong solution	
e	Evaporator		v	Vapor	
g	Generator		w	water	
in	Inlet		ws	Weak solution	
out	Outlet				

Abbreviations

COP	Coefficient of performance	DMFTEG	Di methyl form amid of tetra ethylene glycol
LiBr	Lithium Bromide	R22	Refrigerant 22

Experimental Study on Effect of Changing Welding Current on Mechanical and Metallurgical Properties of Seam Welding Joint for Low Carbon Steel AISI 1005 (0.8 mm)

Ammar Azeez Mahdi AL-Yasari

Welding Department - Technical College Baghdad

Abstract

The aim of this work is to study the effect of changing welding current on the mechanical and metallurgical properties and choose the best welding current depend on result of study. The present work is an experimental study on effect of changing welding current on properties of seam welding joint for low carbon steel AISI 1005. Experiments results shows with increase welding current, hardness number will increase, also differentness in hardness number between weld nugget and HAZ (Heat Affected Zone) will increase and border of HAZ become bigger. Best mechanical results was achieved when welding current increased this doesn't mean that the highest current will become the suitable one, because the higher current will cause burin through in metal sheets and will cause leakage in products (liquid or gas storage tank), also will effect on grain size and microstructure due to changes in cooling rate, also the final shape of joints its important because most application of this type of weld is weight-goods industries (for civil using), so when use high welding current the final shape of joint will deform. Depended on above the best welding current rang is between $17 \leq I < 19$ K Amp.

Keywords: Mechanical and Metallurgical Properties of weldment, Seam welding.

الخلاصة

يهدف البحث الى دراسة تأثير تغير تيار اللحام على الخواص الميكانيكية والميتالورجية لوصلات اللحام النقطي المستمر للحديد واطىء الكربون، واختيار افضل تيار معتمداً على النتائج، حيث اظهرت النتائج العملية انه كلما زاد تيار اللحام زاد رقم الصلادة للملحومة وزادة مقاومة الشد اي تحسنت الخواص الميكانيكية ولاكن هذا لايعني ان افضل تيار يستخدم هو الأعلى قيمة لانه قد يؤدي الى انصهار بعض مناطق اللحام مما يؤدي العيب في المنتج لأن اغلب استخدامات هذا النوع من اللحام يكون في الخزانات، كما ان تطبيقات هذا اللحام تكون ظاهرة للعيان في اغلب التطبيقات المدنية لذلك يكون الشكل النهائي للمنتج ضروري وبناءاً على معطيات الخواص المجهريية والميكانيكية كما اوصت الجمعية الأمريكية للحام كانت افضل نتائج هي باستخدام تيار لحام يتراوح بين ١٧ و ١٩ كيلو امبير.

Introduction

Seam welding involves the joining of two or more pieces of sheet metal in localized areas where melting and coalescence of a small volume of material occurs from heating caused by resistance to the passage of an electric current. A common example is the gastight or liquid tight [1]. This study tries to choose the best welding current that improve joint mechanical and metallurgical properties, without deflect its final shape because some of these joint will be clear to show in the final products.

1- Theoretical parts

Resistance Seam Welding (RSEW) is a process in which heat caused by resistance to the flow of electric current in the work metal is combined with pressure to produce a welded seam. This seam consisting of a series of overlapping spot welds is normally gastight or liquid tight .Two rotating circular electrodes (electrode wheels) or one circular and one bar-type electrode are used for transmitting the current to the work metal . When two electrode wheels are used, one or both wheels are driven either by means of a gear driven shaft or friction drive that contacts the peripheral surface of the electrode wheel.

The series of spot welds is made without retracting the electrode wheels or releasing the electrode force between spots although the electrode wheels may advance either continuously or intermittently. The magnitude of the current, the duration of current flow, the electrode force, and the speed of work piece or electrode travel are all related and must be properly chosen and controlled to produce a satisfactory resistance seam welded joint. The principles described in the article “Resistance Spot Welding” (RSW) in this volume are applicable also to RSEW. [1]

1-2 Seam Welding Cycle

The process sequences of seam welding are explaining bellow there are five definite stages with time:

- 1- Squeeze time: - The time elapsed between the initial application of the electrode force on the work piece and first application of current in making seam weld.
- 2- Weld time (weld interval):- the time period in which welding current is applied to the work during making a single-impulse.
- 3- Heat time:- The time that the current flows during any one impulse .
- 4- Cool time: - The time interval between successive heat times.
- 5- Hold time: - The time period during which force is applied to the work after current ceases to flow.[2]

2- Experimental works:

According AWS (American Welding Society) resistance welding hand book there are three tests should be done to make sure that the suitable settings are be used there are [1-3] :

1. Tensile-shear test
2. Micro hardness test
3. Microstructure test

The main steps of the experimental works conducted in this study are;

- 1- Measuring the mechanical properties and failure mechanism for base metal and resistance seam weld. This includes:
 - (a) Measuring the ultimate tensile strength and breaking load for base metal and resistance seam weld specimens.
 - (b) Measuring the micro hardness number to determine the limits of HAZ, and the difference in the hardness number between the base metal and welding zone.
- 2- Studying the microstructure of all welding zones (base metal, welding nugget and heat affected zone) to describe nugget size, grain size and arrangement.

The nominal chemical composition and nominal mechanical properties of cold rolled AISI 1005 low carbon steel sheet (0.8mm) is shown in Table 1 and Table 2, respectively.

Table (1) Nominal chemical composition of low carbon steel AISI 1005

Material type	C %	Mn %	Si %	P %	S %
Plain carbon steel	0.09	0.20-0.4	0.017	0.04	0.05

Table (2) Nominal mechanical properties of low carbon steel AISI 1005

Mechanical properties Material type	Tensile strength (MPa)	Yield Strength (MPa)	Modulus of elasticity (GPa)	Strain mm / mm	HV
low carbon steel AISI 1006	325	177	200	0.25	119

2-1 The Tension-Shear Test

This test consists of pulling in tension, a test specimen obtained by lapping to strips of metal and joining them by a single weld.

The ultimate strength of the specimen and the manner of failure whether by shear of the weld metal, or by tear of the parent metal, and whether a ductile or brittle fracture is obtained, should be recorded. Specimens in same thickness and dimension selected were from the same Carbon steel sheet at the same roll direction, for lap- Tension shear test. The specimen dimensions are (25.4 mm) in width and (101.6 mm) in length according AWS Resistance Welding Hand Book [1] [4]. It is recommended that the grips of the testing machine be offset to avoid bending at the grips. As show in fig (2).



Fig (2) seam welding joints

2-2 Micro Hardness Test

According ISO standard metallic materials hardness test HV1 (1) Kg force load was applied to surface of specimen to achieve accurate result. Fig (3) shows a sketch explaining micro hardness locations, results have been taken along straight line starting at center of seam-weld through HAZ until reaching to unaffected base metal (results become same), these results have been taken at each 0.5 mm.[3]

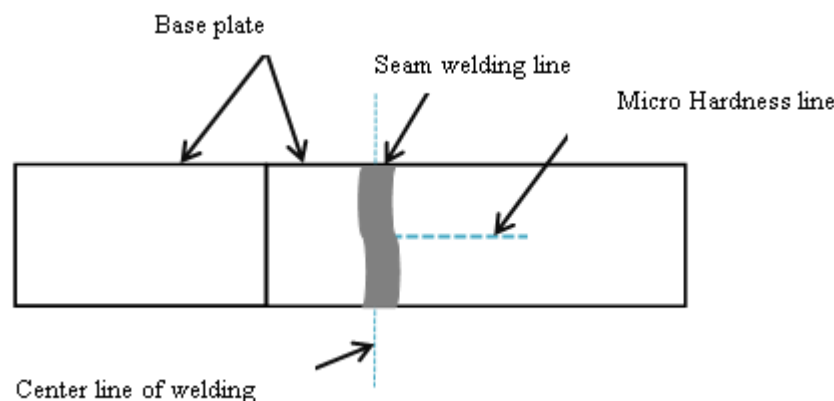


Fig (3) sketch show micro hardness line

2-3 Microstructure Testing

To show the microstructure changes and grains arrangement, and also to describe welding zone after welding process was completed, also to find the formed phases in the weld nugget and heat affected zone, the microstructure test was carried out.

3- Result and discussions

3-1 The Tension-Shear Test results

Figures (4) through (7) show the load displacement curves as a result of tensile shear test for different seam welding currents.

Fig. (4) shows load displacement curve for 13 K amp welded joint, maximum load was 1830 N with 0.42 mm the fracture take place at welding metal, weld was clean, full smooth (without any concave or convex), the weldment was free from burn through and electrodes end dose not effected by welding.

Fig.(5) represented load displacement curve for 15 K Amp, 6000 N was the maximum load with 23 mm displacement and the tearing by 45° happen at the base metal, the joint was clean less smoothly than the previous one (low concave or convex), the weldment was free from burn through and electrodes end dose not effected by welding

Fig (6), shows load displacement curve for 17 K Amp maximum load was 6350 N at 23 mm also the tearing by 45° is happen at the base metal, the weld still clean has low concave and convex, more homogenous and electrodes dose not effect, the weldment was free from burn through

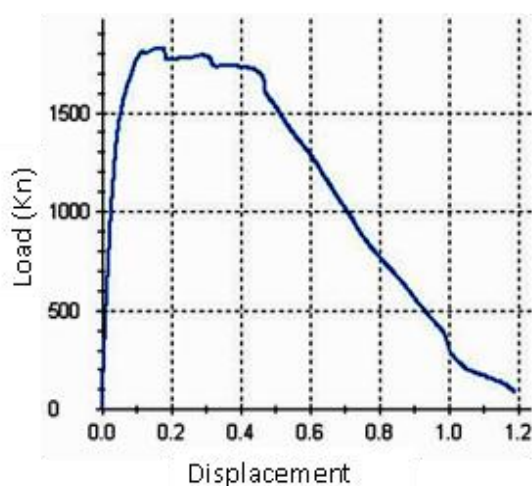


Fig (4) load displacement curve for 13 K amp welded joint

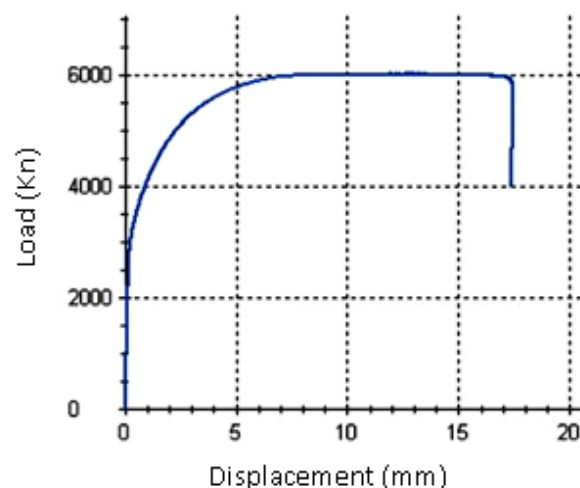
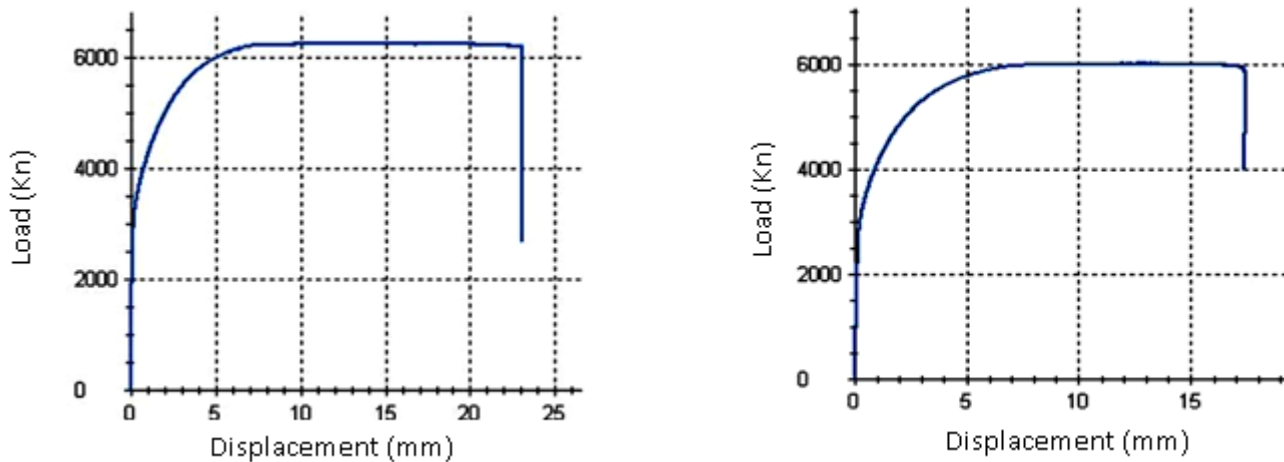


Fig (5) load displacement curve for 15 K amp welded joint

At (19 Kamp) load reached to (6000 N) with displacement (18mm) and the tearing by 45° is happen at the base metal fig.(7).



3-2 Micro Hardness Test results

As explained in a previous chapter on the procedure of test, the measuring starts from center and along straight line outside nugget. It is obvious that the lowest hardness number (for welding zone) registered is in nugget center, the number of hardness gradually increases until it reaches its highest value in HAZ these differentness in hardness number due to the difference in cooling rate between nugget and HAZ which mainly affected in grain size. Fig(8), shows all hardness curves of all welded specimens, by careful look to this curve it's found: first HAZ width have direct relation with current increase, second the difference in hardness number between weld nugget and HAZ increase with increase of welding current this is normal because the cooling rate will be different in each time, and third all curve meet at 0.5 mm from center.[4-5]

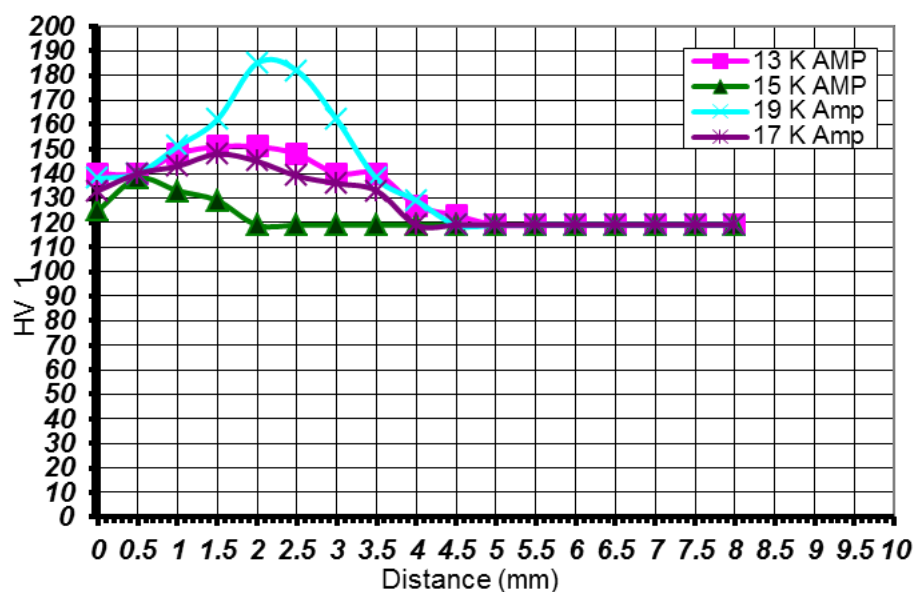
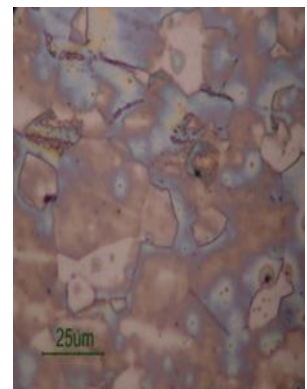
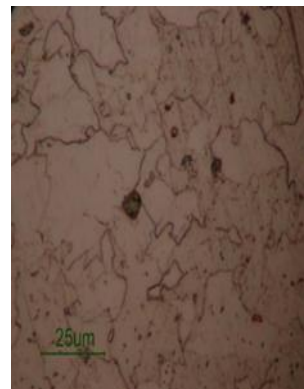
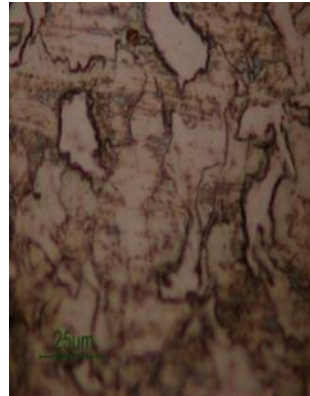
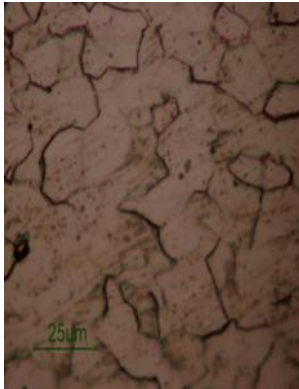


Fig (8), micro hardness test result

3-3 Microstructure Test Results

Figures (9) through (12) show the microstructure for different welding currents joints, this figure aim to show changes in grain size and arrangement with welding current. [6]



**Fig (9) microstructure
for 13 K Amp
welded joint**

**Fig (10) microstructure
for 15 K Amp
welded joint**

**Fig (11) microstructure
for 17 K Amp
welded joint**

**Fig (12) microstructure
for 19 K Amp
welded joint**

First look for four microstructure photos its difficult make a distinction among grain size because there is direct water cooling during welding this made process is like quenching, but still some differentness, grain size appear somewhat bigger when welding current raised and became more homogenous specially for 17 K Amp.

4- Conclusions

1. The best welding current for AISI 1005 (0.8 mm) was 17 Kamp.
2. When welding current increase strength of welded joint increase to, until reach to 19 Kamp the metal become burn through.
3. The width of HAZ is between 3 to 3.5 mm and the difference between in the hardness number of weld nugget and HAZ become large when welding current increase.

No large difference in grains size when using different welding current but still there is relationships between them grain size appear somewhat bigger when welding current raised.

5- References

- 1- Resistance welding theory and use, American Welding Society 1956.
- 2- Bienvenu, Join “An Investigation of Resistance Welding Performance of Advanced High-Strength Steels” auto / steel partnership 2000
- 3- C. L. Tsai, D. W. Dickinson, C. Y. Kim, and M. D. Garnett “Mechanical Behaviors of Resistance Spot Welds During Pry- checking Test” Welding Journal, American Welding Society, JUNE 2006
- 4- M. Zhou,s. J Hu and H. Zhang “Critical Specimen Size for Tensile-Shear Testing of Steel Sheets”, Welding Research Supplement, 1997
- 5- W. L. Chuko, and J. E. Gould, “Development of Appropriate Resistance Welding Practice for Transformation-Hardened Steels” Supplement to Welding Journal, January, 2002

Implementation of Artificial Neural Network and Random Iteration Algorithm Uses in Medical Images

Dr. Maha Abdul Ameer Kadhum

Foundation of Technical Education
Technical Instructors Training Institute
Lecturer

Dr. Entidhar Mhawes Zghair

Foundation of Technical Education
Technical Instructors Training Institute
Lecturer

Abstract

This research present a multiply connected neural network designed to estimate the fractal dimension (Df) using the Random Iteration Algorithm (IFSP). Fractal analysis is a powerful shape recognition tool and has been applied to many pattern recognition problems. Additionally, the one of the most adaptive Random Iteration Algorithm (IFSP) methods for estimating (Df). The architecture presented separates the calculation of (Df) into two sections, a data sampling section and a linear regression section. The data sampling section provides the ability to dyadic ally sample the data. The linear regression section simply calculates the slope of the best line through the sampling results. Instructional program was designed and built according to Knirk and Gustafson Design model, as one of the instructional design model in order to comprehension of the integrated ideas and concepts related to research .

Keywords: Neural Network, Random Algorithm, Medical Images

الخلاصة

يقوم هذا البحث بدراسة شبكة عصبية متعددة الارتباطات صممت لحساب البعد الكسوري باستخدام طريقة الدالة المكررة العشوائية. التحليل الكسوري هو اداة تعريف او تمييز بشكل فعال وله تطبيقات عديدة بمسائل التعريف النسقي بالاضافة الى ذلك ، طريقة الدالة المكررة العشوائية هي واحدة من الطرق الشائعة لحساب البعد الكسوري . تم فصل حساب البعد الكسوري الى قسمين قسم عينة البيانات وقسم التراجع الخطي . قسم البيانات العينية يجهز للقابلية لتجزئة البيانات العينية. قسم التراجع الخطي ببساطة يقوم بحساب المنحني لاحسن خط موجود في نتائج العينات .برنامج تعليمي تم تصميمه وبناءه نسبة الى نموذج تصميم (Knirk and Gustafson) كواحد من النماذج التعليمية المصممة حتى يتم استيعاب الأفكار المتكاملة و المعطيات المتعلقة بالبحث .

1- Introduction

The concept of fractal has given rise to a new system of geometry that has a significant impact, not only on mathematics but also on such diverse fields as biomedicine, Physics, chemistry, physiology, geology, meteorology, material science and fluid mechanics. A distinctive feature of most fractals are "self-similarity" but it must be noted that not all fractals have self-similarity or at least not exactly satisfying this property, because self-similar object is one whose component parts resemble the whole [1] .

2- Image Metric Space

A metric is a function that measures the distance between two things. For example, the things can be two points on the real line, and the metric can be the absolute value of their difference. The reason for using the word "metric" rather than "difference" or "distance" is to make it more general. There are metrics that measure the distance between two images, the distance between two sets, etc. [2].

A metric space (X, d) is a space or a set of points, say X , together with real valued function $d: X \times X \rightarrow \mathbb{R}$. which measures the distance between pairs of points $(x$ and $y)$ in X . suppose that the function d has the following properties:

$$\left. \begin{array}{l} \text{a. } d(x, y) > 0 \\ \text{b. } d(x, y) = 0 \text{ if } x=y \\ \text{c. } d(x, y) = d(y, x) \\ \text{d. } d(x, z) \leq d(x, y) + d(y, z) \end{array} \right\} \quad \forall x, y \in X$$

Such a function d is called a metric on the space X . The set X may represent a set of points, or a set of images.

In order to discuss image compression, the image should be represented as a mathematical function, $z = f(x, y)$. The graph of this function is generated by taking an image and plotting the grey level of each pixel at position (x, y) as a height (with white being the highest and black is the lowest height). Thus, when referring to an image, the function $f(x, y)$ gives the grey level at each point (x, y) [3].

3- Random Iteration Algorithm

It is more powerful tool than deterministic algorithm, the IFS is the iterated function system with probabilities (IFSP)[4]. It is a sort of random iteration algorithm, IFS is constructed by associating a probability value to each of the affine transformations according to its "importance" relative to other affine transformations. An IFSP is an IFS $W = \{w_1, w_2, \dots, w_n\}$ with probabilities $P = \{p_1, p_2, \dots, p_n\}$, such that $p_i > 0$ for all $i = 1, 2, \dots, n$,

$$\sum_{i=1}^n p_i = 1 \quad \dots\dots\dots(1)$$

It is possible to construct fractals using equal probabilities. However, to be efficient and to cover the space as quickly as possible, the best procedure is to set the value of each probability to be proportional to the volume of its corresponding transformation. The volume of a transformation is defined as the volume of the absolute value of the determinant of the deformation matrix. That is, the default probability should be [5]:

$$P_i = \frac{|det A_i|}{\sum_{j=1}^n |det A_j|} = \frac{|a_i d_i - b_i c_i|}{\sum_{j=1}^n |a_j d_j - b_j c_j|} \quad \dots\dots\dots(2)$$

For $i = 1, 2, \dots, n$

Process of encoding an arbitrary IFSP using random iteration method. It is the process of rendering a fractal from its IFSP. The steps of the algorithm can be given as follow [6]:

1. Initialize $x = 0, y = 0$ (Starting point).
2. Choose arbitrary k to be one of the numbers $1, 2, \dots, n$, with probability P_k
3. Apply the transformation w_k on the point (x, y) to obtain the point (x', y') .
4. Plot the point (x', y') .
5. Set $x = x'$ and $y = y'$.
6. Goto step 2.

The process mentioned above are illustrated by the flowchart shown in Figure (1)

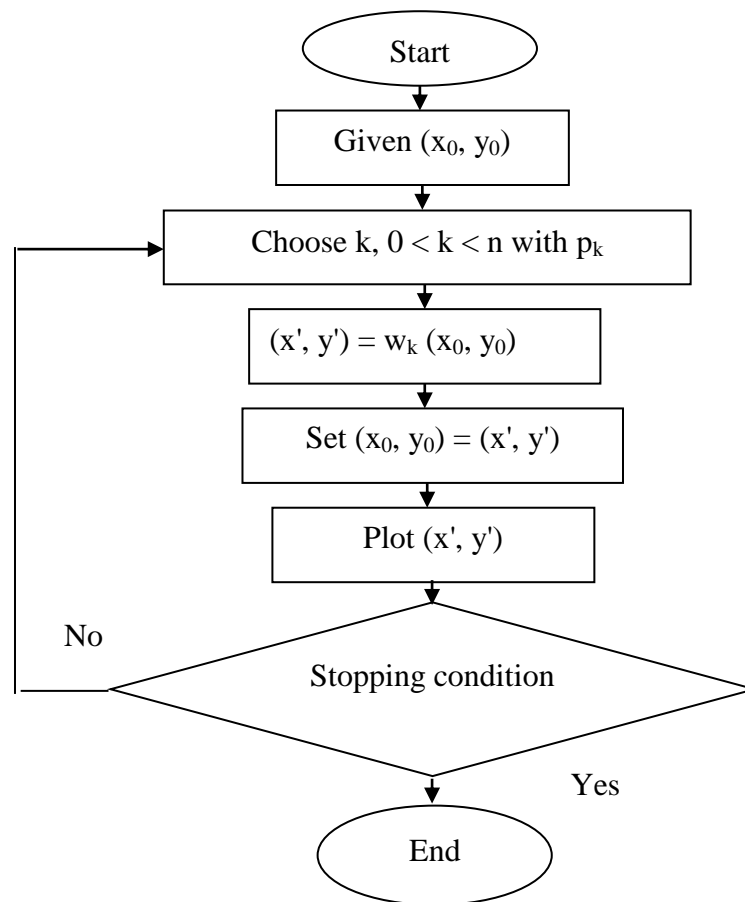


Figure (1) Flowchart of the image generation using random IFS

Linear regression is used to find the best fitting line as shown in fig(2)

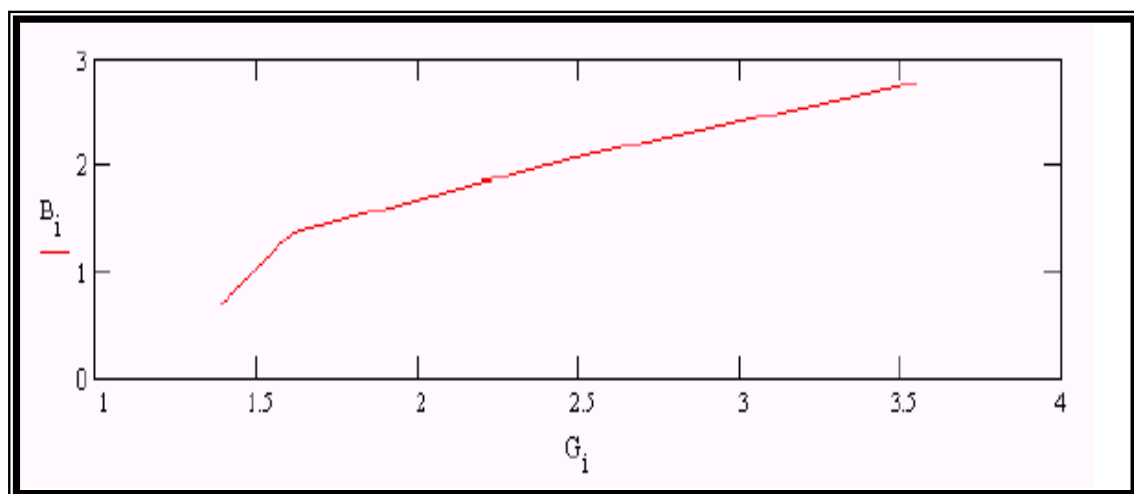


Fig (2) Log-log plot of data.

D_f is the slope of this line. We used a grid size half the size of the previous grid. Other implementations use grid sizes of 3x3 pixels, then 5x5 pixels, then 7x7 pixels, and so on. Hence, the box counting method (BCM) (and most other digitally implemented methods) are only estimates of D_f (dB), where B_i number of box length and G_i maximum of box length [7].

4- Fractals in biomedicine

It is not surprising that the methods of fractal mathematics, which allow quantification of structure or pattern across many spatial or temporal scales, could be useful in many biomedical applications including:

- Biosignal analysis, pattern recognition.
- Radiological and ultrasonographic image analysis)[8].
- Cellular morphometry, nuclei (chromatin) organization, gene expression.
- Physiological and pathological states of brain and nervous system.
- Circulatory system, lungs and pulmonary system.
- Analysis of connective tissue, epithelial-stromal tissue interface, tissue-remodeling.
- Biological design, angiogenesis, evolutionary patterns, morphogenesis, spatio-temporal
- Tree structures, vessel branching.
- Structure, complexity and chaos in tumors.
- Membranes and cell organelles during growth and death (apoptosis, necrosis).
- Aging, immunological response, autoimmune and chronic diseases.
- Complexity, self-organization and chaos in metabolic and signaling pathways.
- Structure of biopolymers (proteins, nucleic acids).

5- Artificial Neural Network (ANN)

ANN is an information –processing system that certain performance characteristics in common with biological neural network One of the main advantages of the ANN is that they infer solutions from data without prior knowledge of the regularities in the data , they extract the regularities empirically [9] ,fig (3)shown the ANN

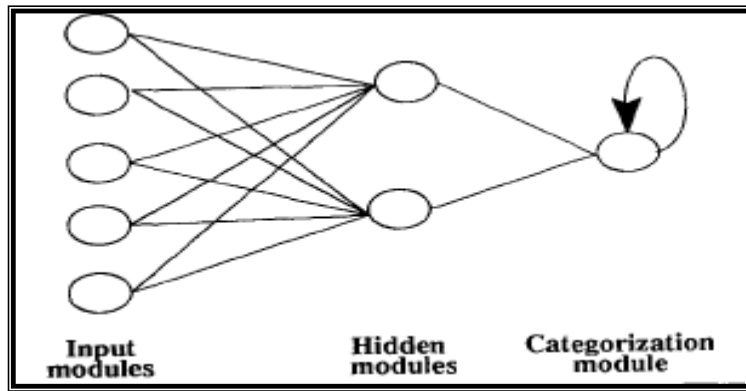


Fig (3) shown the ANN[10]

6- Learning Rule Using Maximum Entropy Estimation

We now present a brief review of maximum entropy estimation [11]. Given a finite set S of n elements, let $p = \{p_0, p_1, p_2, \dots, p_n\}$ represent the probability distribution for S , where p_i is the probability of occurrence of the i th element in S . We define the entropy H of p as:

$$H(p) = \sum_{i=0}^n p_i \log(p_i) \dots\dots\dots (3)$$

Now, let f_k be a set of c functions on S , and m_k be the set of values of the means of these functions. Maximum entropy estimation is simply the problem of finding a probability distribution p on S such that the distribution has the specified mean values m_k and $H(p)$ is maximized. p is a constrained maximization problem. In fact, using the gradient of the entropy, ∇H , we can solve it, where

$$\nabla H = \sum_{i=0}^n -(\log(p_0) + 1), -(\log(p_1) + 1), \dots -(\log(p_n) + 1))^T \dots\dots\dots (4)$$

Now, we have the knowledge to build our gradient ascent learning algorithm [12].

7- Instructional Design Model

The IDM quality of knowledge transferred from an instructor to a learner. IDM starts by analyzing the learning needs and goals and it is followed by the development (of a delivery system to meet learning goals). Testing and evaluation of learning materials and learning activities an organized productive frame and laws depended on educational theories. The model is constructed on the bases of the occurrence of a problem. There are several models for educational design. But all have common features, which are: -

- ◆ The analysis of a real problem which represents the educational demand.
- ◆ Definition of the aims and the strategy of every problem [13].

The flowchart model used in Fig below shows the five phases with their basic steps listed below them.

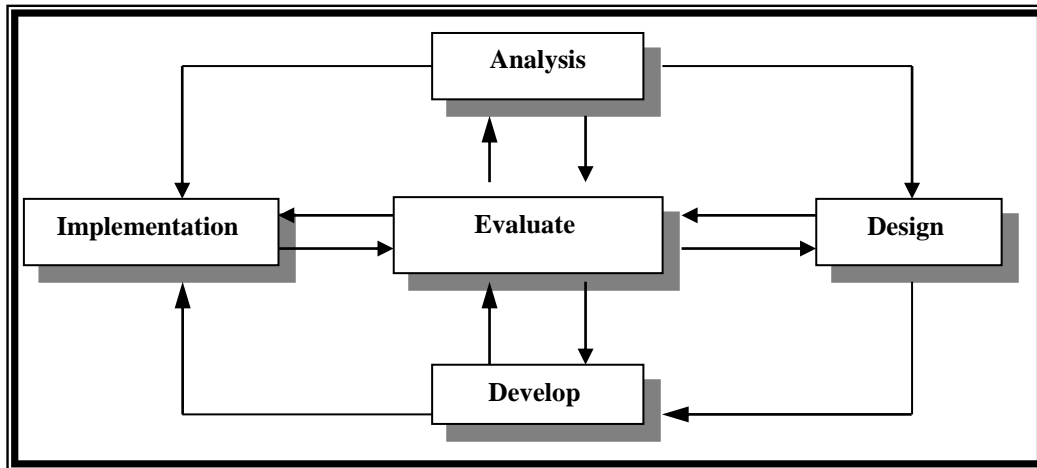


Fig (4) Flowchart model

8- Research procedure

The research use Matlab implementation the program to estimate the fractal dimension and neural network. The network consists of two independently trained stages. Both stages are in fact back propagation neural networks with one hidden layer. It is used to recognize blood cell images Fig (4) Multistage back propagation neural network

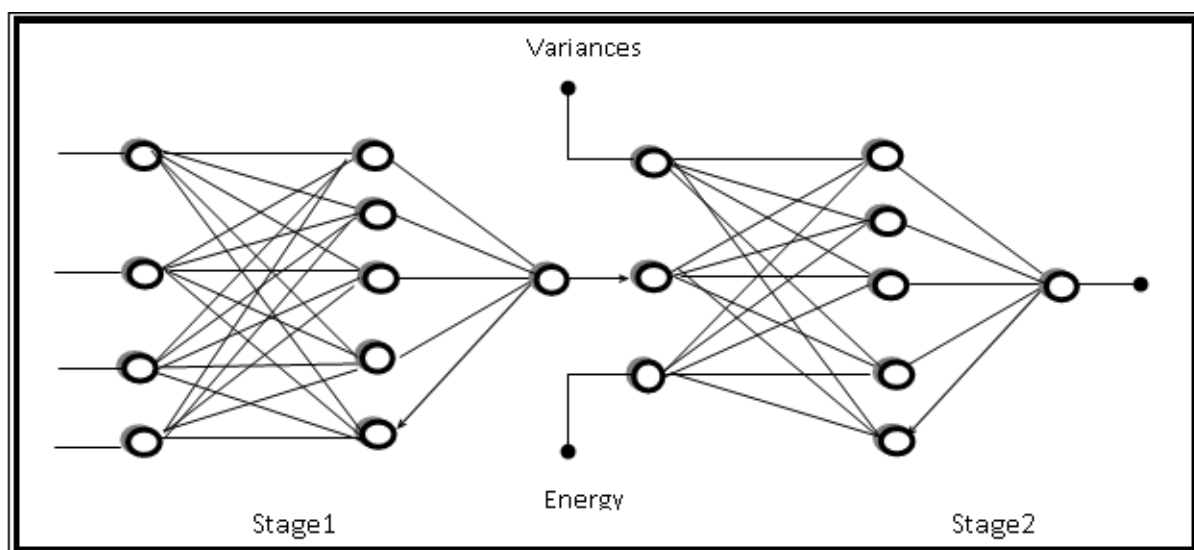


Fig (4) Multistage back propagation neural network for classifying images

The first stage, called the detail network, takes as its inputs all information bits of the region of interest. In their initial experiment by use a 16-bit region of interest. Thus, they had 16 input units. They state that they achieved best results with five hidden units in the hidden layer. Finally, one output unit is used representing the two classes of malignant and benign. The second stage takes three inputs, the output from the first stage and two calculated features. These features are both calculated from the region of interest extracted from the microscope. The first feature is the variance and is obtained by the following

$$v = \sqrt{\frac{1}{n^2} \sum_{i=0}^n \sum_{j=0}^n xi, j - \mu^2} \quad \dots\dots\dots (5)$$

Where xi,j are the inputs and are their average. This feature contains the same information as the standard deviation used in section, average is defined as:

$$\mu = \sqrt{\frac{1}{n^2} \sum_{i=0}^n \sum_{j=0}^n xi, j} \quad \dots\dots\dots (6)$$

Where xi,j is as before. The second feature is the energy and is defined by:

$$e = \sqrt{\frac{1}{n^2} \sum_{i=0}^n \sum_{j=0}^n xi, j} \quad \dots\dots\dots (7)$$

Where Xi,j is as before. These two features combined with the output from stage one form the inputs for stage two. As in stage one, stage two contains five hidden units. Its single output unit represents the final classification of the network: malignant or benign. Each stage is sequentially trained. Initially, the first stage is trained with the training data. Then, its output, along with the two calculated features, will be used as input to train the second stage. The training data consists of blood cell images of 16 x 16 pixels the data sampling section is designed to sample the data in a dyatic manner depending on the value of N_i . There are two types of nodes in this section: an input node, which segments the inputs (to 1 or 0); and a data processing node, which determines the sample rate. The neural activation function for the data processing nodes is:

$$O_j = [N_i * \sum nodes] + [(1 - N_i) * \max(nods)] \dots \dots \dots (8)$$

Immediate left are treated as a single entity (via the maximum function). This is shown in the fig (4), [10]. Given the activation function and its dependence on N_i a network becomes possible that provides parallel dyatic sampling .fig (5) shown the sample of medical image and histogram for these images

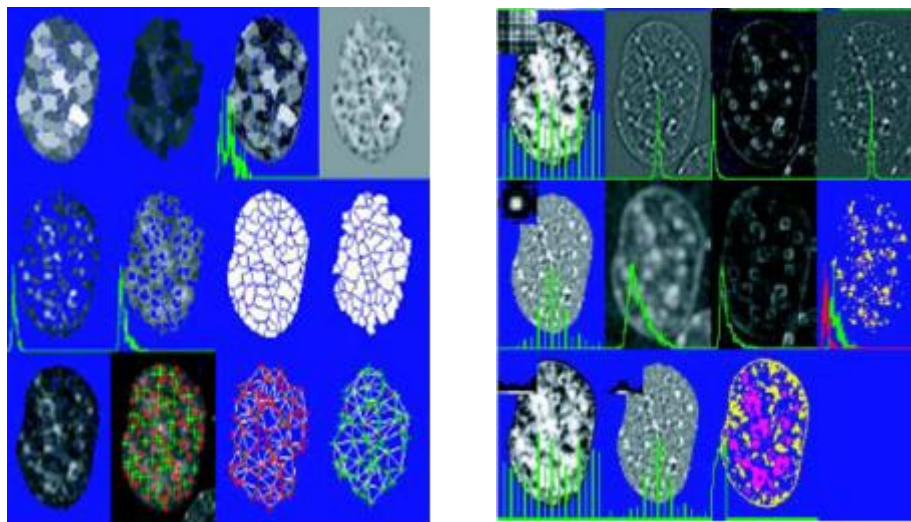


Fig (5) sample of image samples of images and histogram

In keeping with the all-neural network architecture, we also developed a neural network to compute the linear regression of the data generated by the sampling section and have the best of fractal dimension value by apply the equation (2) also designing and constructing an instructional computer program by using Knirk and Gustafson model to introduce the basic concepts for the fractal and neural according to is shown in fig(6). Twenty sub-images were selected from each microscope and where tagged, the Knirk and Gustafson Design Model is a three stage process which includes problem determination, design and development. The problem determination stage involves identifying the problem and setting instructional goals. The design stage includes developing objectives and specifying strategies. Finally, in the development stage, materials are developed. final evaluation is made on the basis of constructing special questionnaire for the learners to find out the opinions of 20-learners.

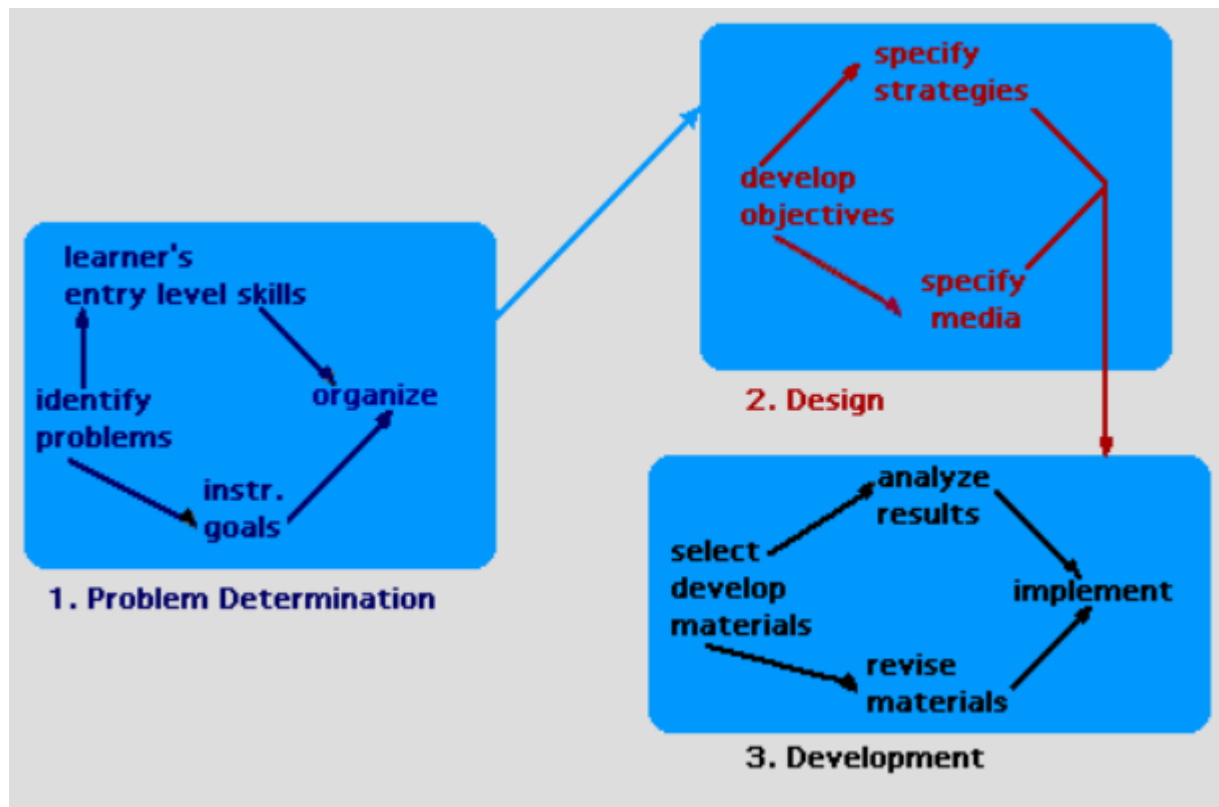


Fig (6) The Knirk and Gustafson Design Model [11].

9-Experimental Results

We utilize the fractal dimension of the perimeter surface of cell sections as a new observable to characterize cells of different types. We propose that it is possible to distinguish from healthy cells with the aid of this new approach. Their goal was to achieve the upper bound of the reported accuracy of the method of visual inspection of fine needle aspirates. We computed 30 features from each image. These features are: area, radius, perimeter, symmetry, number and size of concavities, fractal dimension (of the boundary), compactness, smoothness (local variation of radial segments), and texture (variance of gray levels inside the boundary). For each of these ten features, the calculated mean value, extreme value, and standard error, totaling 30. Experimental results show that:

- 1- The multi-stage network resulted in a sensitivity of 100%. Unfortunately, the authors forgot to mention their achieved specificity. It is meaningless to mention one without the other. One could easily build a network that has 100% sensitivity. Simply, make the network always classify inputs as malignant, fig (7) show the value of fractal dimension for images uses in research.

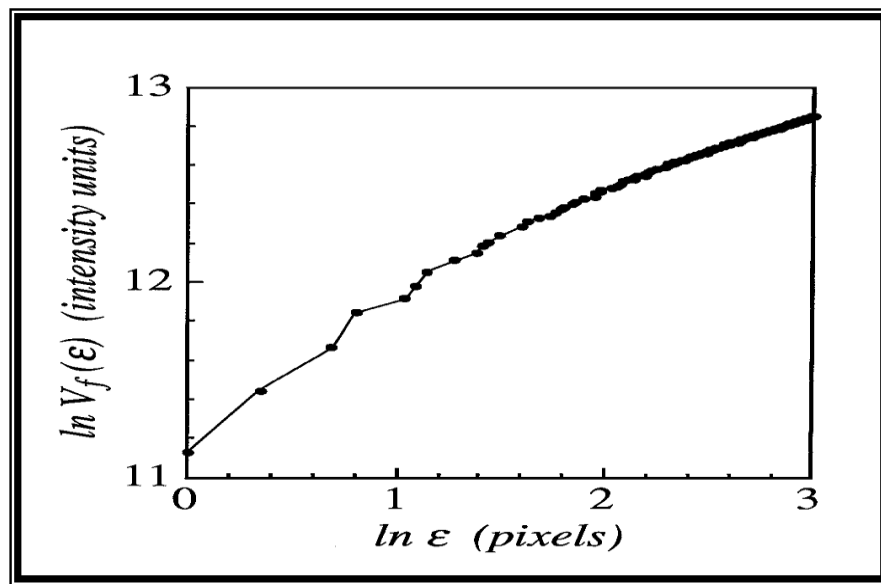


Fig (7) show the value of fractal dimension

- 2- We compare between the single-stage and multi-stage networks close, clearly the multi-stage network is an improvement over the single-stage network. Claims that using calculated features from a microscope image, instead of using the actual information bits of the image, as presented a multi-stage network that takes advantage of both the calculated features and the information bits, both approaches remain inconclusive in their experimental results 100% accuracy and 100% sensitivity respectively. These cases formed the training set used to train the system. As opposed to the other papers discussed earlier in this survey, one was built for each subset of one, two, three and four features (from the thirty calculated features). The remaining combinations that performed well on the testing set were then retrained using 10-fold cross-validation in order to estimate its real-world performance. One neural network diagnosis tool achieves 80% predicted accuracy and 100% observed accuracy.
- 3- The designed instructional program helps in saving time and efforts of the learner when studying the subject of fractal geometry and neural network application in medical images.

10- Conclusion

From discussing the results we conclude the following :

- 1- Multiply connected neural network designed to estimate the fractal dimension (D_f) using the Random Iteration Algorithm (IFSP).
- 2- The architecture presented is composed of two sections, a data sampling section and a linear regression section. The data sampling section employs two types of nodes: an input node, which segments the inputs (to 1 or 0); and a data processing node, which determines the data sample rate. The data processing nodes use a neural activation function that, depending on the value of N_i . The linear regression section computes the slope of the line through the results generated by the data sampling section.
- 3- The architecture presented scales well and can demodified to process 1-D or 2-D data. While the neural network presented does generate an estimation of D_f using the (IFSP), Several of the activation functions are not biologically plausible.
- 4- Instructional program tend to achieve the principals of teaching and learning through translating them into reality, so that by these principals, it buildup the skill of knowledge through providing experience to learn the fractal and neural network application.

11-Reference

- [1]- H. J. Reitboeck and J. Altman, "A Model for Size- and Rotation-Invariant Pattern Processing in the Visual System", Biological Cybernetics, Vol. 51, pp. 113-121, 1984.
- [2]- A. D. Culhane and Zane, "A Neural Network Approach to Discrete Hartley and Fourier Transforms", IEEE Transactions on Circuit and Systems, Vol. 36, No. 5, pp. 695-702, 1998.
- [3]- B. B. Mandelbrot, "The fractal geometry of nature", Freeman, San Francisco, (1993).
- [4]- B. B. Mandelbrot and J. W. Van Ness, "Fractional Brownian motions, fractional noises and applications", SIAM Review 10(40), pp. 422-437, 1998.
- [5]- K. J. Falconer, Chapter 2: " Hausdorff measure and dimension, In Fractal Geometry Mathematical Foundations and Applications", Thomson Press Ltd., 1998.
- [6]- D. Comis, "Fractals Abridge to the future for soil science", Agricultural Research Magazine 46(4), pp. 10-13, 1998.
- [7]- S. Davies and P. Hall, "Fractal analysis of surface roughness by using spatial data", Journal of The Royal Statistical Society Series, B Statistical Methodology 61(1), pp.3-29, 2002.
- [8]- N. Mihara, K. Kuriyama, S. Kido, C. Kuroda, T. Johkoh, H. Naito, and H. Nakamura, "The usefulness of fractal geometry for the diagnosis of small peripheral lung tumors", Nippon Igaku Hoshasen Gakkai Zasshi 58(4), pp. 148-151, 1998.
- [9]- W. N. Street, "A neural network model for prognostic prediction", Proceedings of the Fifteenth International Conference on Machine Learning, Madison, Wisconsin, Morgan Kaufmann, 2000.
- [10] M. L. Rossen, "Representational Issues in a Neural Network Model of Syllable Recognition", <http://www.ivsl.org/pdf/2012>.
- [11]- R. Esteller and Holand ., "Fractal Dimension characterizes seizure onset in epileptic patients", IEEE International Conference on Acoustics, Speech, and Signal Processing, Arizona, 1999.
- [12]- Wilson, B., "The Future of Instructional Design and Technology", <http://www.jnd.org/books.html>, 2006, p.1-7.
- [13]- Kemp, J., "Design and Implementation", <http://www.Student.seas.gwu.edu/~sbroxton/ISD/GIFSJK-design>, 2009.

Effect of the Axial Heat Conduction in Parallel Flow Rectangular Microchannel Heat Exchanger

MSc. Hayder Mohammed Hasan

Shatra Technical Institute, Machines and Equipments department

ABSTRACT

The axial heat conduction in parallel flow microchannel heat exchanger with rectangular ducts was numerically investigated, for laminar, 3-D, incompressible, and steady state flow of water. The governing equations, continuity, Navier-Stokes equations (momentum equations), and the energy equations for the hot and cold fluids were solved by using SIMPLE algorithm with finite volume method and FORTRAN code to obtain the temperature distribution for the two fluids and the separating wall between them. The results play an important role of the axial heat conduction on the effectiveness in parallel flow microchannel heat exchanger and the factors affecting the axial heat conduction are; Reynolds number Re , thermal conductivity ratio K_r , aspect ratio α and channel volume. Increasing of Re , K_r , α and channel volume each separately leads to increase the axial heat conduction and vice versa.

Keywords: Micro channel, heat exchanger, parallel flow, numerical solution, axial heat conduction and effectiveness.

الخلاصة

عددياً تمت دراسة تأثير التوصيل الحراري المحوري في مبادل حراري مايكروبي ذي قنوات مستطيلة الشكل لجريان متوازي طبقي ثلاثي الأبعاد للماء وفي حالة الاستقرار ولا انضغاطي. تم حل المعادلات الحاكمة للجريان وهي معادلة الاستمرارية (equation) (continuity) ومعادلات الزخم (momentum equations) ومعادلة الطاقة (energy) equations باستخدام طريقة (SIMPLE method) وقد تم تحويل المعادلات الحاكمة إلى الشكل العددي باستخدام طريقة الحجم المحددة (finite-volume method) وباستخدام لغة فورتران (FORTRAN). بهذه الطريقة تم إيجاد التوزيع لدرجات حرارة المائع والجدار الذي يفصل بينهما. من خلال ملاحظة النتائج المستحصلة من الحل العددي، تبين بأن هنالك تأثير مهم للتوصيل الحراري المحوري على الفعالية في المبادل المايكروبي كما إن هنالك مجموعة من العوامل التي تؤثر عليه وهي، عدد رينولدز (Re) ونسبة الموصلية الحرارية (thermal conductivity ratio K_r) والنسبة الباعية (aspect ratio α) وحجم القنوات. عند زيادة Re و K_r و α وحجم القنوات كل على حدة يزداد التوصيل الحراري المحوري، والعكس صحيح.

NOMENCLACHRE***English symbols***

c	specific heat J/(kgK)
C_c	heat capacity of cold fluid ... W/K
C_h	heat capacity of hot fluid ... W/K
C_{min}	minimum heat capacity W/K
C_p	specific heat at constant pressure J/(kgK)
D_h	hydraulic diameter m
H	channel height m
$H_{H.E}$	exchanger height m
k	thermal conductivity W/mK
L	channel length m
\dot{m}	mass flow rate kg/s
p	pressure Pa
q	heat transfer rate W
T	temperature K
t_s	separating wall thickness m
u	fluid x -component velocity . . m/s
v	fluid y -component velocity . . m/s
w	fluid z -component velocity ... m/s
W_{ch}	channel width m
$W_{H.E}$	exchanger width m
x	axial coordinate m
y	horizontal coordinate m
z	vertical coordinate m

Greek symbols

ε	heat exchanger effectiveness
μ	dynamic viscosity Pa.s
ρ	density kg/m ³

Dimensionless groups

$K_r = k_s / k_f$	thermal conductivity ratio
$Re = \rho u_{h,in} D_h / \mu$	Reynolds number
$Pr = \frac{\mu C_p}{k_f}$	prandtl number
$Pe = Re Pr$	Peclet number
$\alpha = H/W$	aspect ratio

Subscripts

c	cold fluid
h	hot fluid
f	fluid
in	inlet
max	maximum value
min	minimum value
out	outlet
s	solid
u	unit
w	water

Superscripts

*	Dimensionless value
---	---------------------

1. INTRODUCTION

The fluid flow in microchannels becomes an attractive area of research during the last few years. This is due to the new applications of the microchannel flow in micro pumps, micro turbines, micro heat exchangers and other micro components. Advantages of compact structure and high heat transfer performance make the microscale heat exchangers showing a

nice foreground on microelectronics, micro devices fabrication, bioengineering, micro electromechanical system (MEMS), and so on. Thus, is becoming more popular, both for commercial purposes and in scientific research [1]. Microchannel heat exchangers can be broadly classified as fluidic devices that employ channels of hydraulic diameter smaller than 1 mm [2]. Knudsen number is a measure of the degree of the rarefaction which is defined as the ratio of mean free path to the characteristic length scale of the system $Kn = \lambda/L_c$ where, λ is the mean free path and L_c is the characteristic length such as channel equivalent diameter. The flow regimes could be classified as: continuum regime when ($Kn < 0.001$), slip flow regime ($0.001 < Kn < 0.1$), transient regime ($0.1 < Kn < 10$) and free molecular regime ($Kn > 10$). In order to simulate the no slip flow regime, the Knudsen number is $Kn < 0.001$. In conventional heat exchanger the solid thickness is small comparatively with the hydraulic diameter; therefore the axial heat conduction may be neglected. This means that the performance of the heat exchanger is primarily depending upon the flow in the ducts (fluid properties and mass flow rate). For microchannel heat exchanger, the solid thickness is large comparatively with the hydraulic diameter, therefore the axial heat conduction in the separating wall (solid) is important and the microchannel heat exchanger effectiveness may decrease due to the effect of axial heat conduction. The present study is deal with effect of the axial heat conduction in microchannel heat exchanger.

To understand the flow through microchannels, many researchers have been investigaty experimentally, analytically and numerically in last decade. For example, Al bakhit et al. [3] numerically investigated the flow and heat transfer in parallel flow microchannel heat exchangers. They used a hybrid approach, in which the nonlinear momentum equations for one or two channels were solved using CFD codes. The velocity field was an input into a user developed code for solving the energy equation and they studied heat transfer for thermally developing laminar flow in two parallel rectangular channels which represent some kind of heat exchangers. From the results, it is found that in the entrance region the developing velocity profiles lead to higher values of overall heat transfer coefficient. Al-Nimr et al. [4] numerically investigated the hydrodynamics and thermal behaviors of the laminar, 2-D, fully developed, slip flow inside an insulated parallel-plate microchannel heat exchanger. They showed that both the velocity slip and the temperature jump at the walls increase with increasing Knudsen number. Yin and Bau [5] studied flow between infinite parallel plates and circular pipes to study the effect of axial heat conduction on the performance of microchannel

heat exchangers. They used a fully developed velocity field and analytically they solved for temperature fields in the channel and solid wall. They found that, the axial conduction plays an important role at the entrance region. Stief et al. [6] numerically investigated the effect of solid thermal conductivity in micro heat exchangers. They showed that the reduction of conductivity of the wall material can improve the heat transfer efficiency of the exchanger due to influence of axial heat conduction in the separation wall. Also, they concluded that increasing heat capacity ratio leads to a reduction in effectiveness for all Knudsen number. Al-bakhit and Fakheri [7] numerically investigated the laminar, parallel flow microchannel heat exchanger with rectangular ducts for developing and fully developing velocity profiles with thermally developing flow in both cases. They showed that the overall heat transfer coefficient is rapidly changed for $x/D_h Pe$ (Graetz number) below 0.03, and therefore the assumption of constant overall heat transfer coefficient is not valid if the Graetz number based on the heat exchanger length is of the order of 0.03. Also, the accurate results can be obtained by solving thermally developing energy equation using fully developed velocity profiles. Mushtaq I. Hasan [8] made numerical investigation to study the counter flow microchannel heat exchanger with different channel geometries and working fluids. He studied the effect of axial heat conduction on the performance of counter flow microchannel heat exchanger with square shaped channel and he found that the existing of axial heat conduction lead to reduce the heat exchanger effectiveness.

2. ANALYSIS

Schematic structure of a parallel flow microchannel heat exchanger with square channels is shown in figures 1 and 2 illustrated in with of channels details with rectangular profiles.

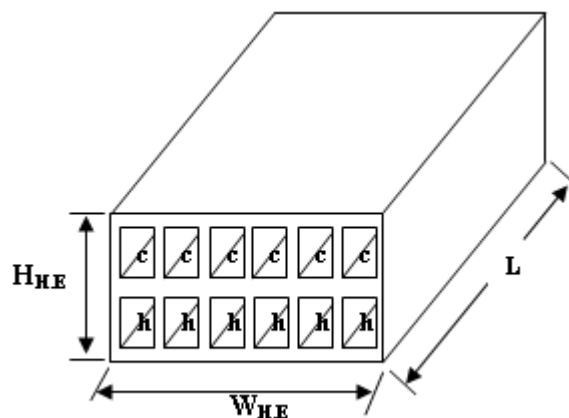


Figure 1 Schematic model of microchannel heat exchanger under concentration.

To study the entire parallel flow microchannel heat exchanger numerically, it is complicated and needs huge CPU time. Due to the symmetry between channels, the individual heat exchange unit is considered consists of two channels (hot and cold) with separating wall as shown in figure 2. Heat is transferred from hot fluid to cold fluid through the thick wall separating between them and this heat exchange unit represents a complete exchanger and gives an adequate indication about its performance.

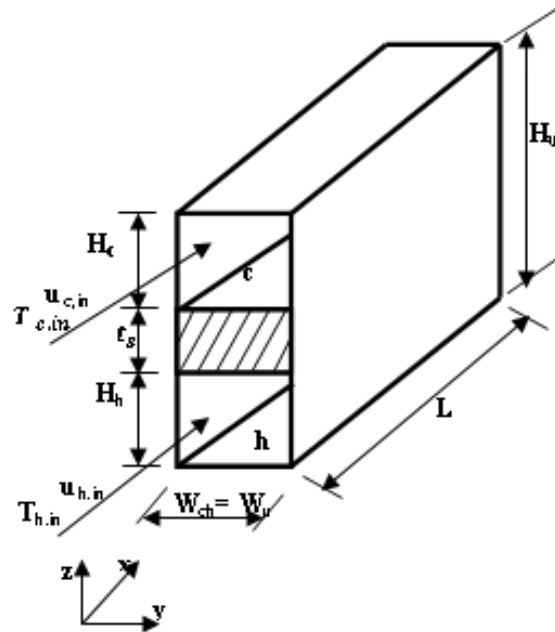


Figure 2 Three-dimensional sketch of the parallel flow heat exchanger unit.

However, the governing equations for the present model are based on the following physical and geometrical assumptions [9]:

- The flow is laminar and steady.
- The Knudsen number is small enough, so that the fluid is regard as continuous medium (no slip).
- The fluids are incompressible, Newtonian, with constant properties; in this case the water is used as working fluid.
- There is no heat transfer to/from the ambient medium.
- The energy dissipation is negligible.
- The pressure gradient is in axial direction only.
- Three dimensional of the flow and heat transfer.

The governing equations and its boundary conditions in Cartesian coordinates and nondimensionalized using the following variables according to [3]

$$x^* = \frac{x}{D_h}, \quad y^* = \frac{y}{D_h}, \quad z^* = \frac{z}{D_h}, \quad t_s^* = \frac{t_s}{D_h}, \quad W_{ch}^* = \frac{W_{ch}}{D_h}, \quad H_i^* = \frac{H_i}{D_h}, \quad u_i^* = \frac{u_i}{u_{h,in}}, \quad v_i^* = \frac{v_i}{u_{h,in}},$$

$$w_i^* = \frac{w_i}{u_{h,in}}, \quad p_i^* = \frac{p_i}{\rho u_{h,in}^2}, \quad T_i^* = \frac{T_i - T_{c,in}}{T_{h,in} - T_{c,in}} \text{ and } T_s^* = \frac{T_s - T_{c,in}}{T_{h,in} - T_{c,in}}$$

Continuity equation

$$\frac{\partial u_i^*}{\partial x^*} + \frac{\partial v_i^*}{\partial y^*} + \frac{\partial w_i^*}{\partial z^*} = 0 \quad (1)$$

x-momentum equation

$$u_i^* \frac{\partial u_i^*}{\partial x^*} + v_i^* \frac{\partial u_i^*}{\partial y^*} + w_i^* \frac{\partial u_i^*}{\partial z^*} = -\frac{dp_i^*}{dx^*} + \frac{1}{Re_i} \left(\frac{\partial^2 u_i^*}{\partial x^{*2}} + \frac{\partial^2 u_i^*}{\partial y^{*2}} + \frac{\partial^2 u_i^*}{\partial z^{*2}} \right) \quad (2)$$

y-momentum equation

$$u_i^* \frac{\partial v_i^*}{\partial x^*} + v_i^* \frac{\partial v_i^*}{\partial y^*} + w_i^* \frac{\partial v_i^*}{\partial z^*} = \frac{1}{Re_i} \left(\frac{\partial^2 v_i^*}{\partial x^{*2}} + \frac{\partial^2 v_i^*}{\partial y^{*2}} + \frac{\partial^2 v_i^*}{\partial z^{*2}} \right) \quad (3)$$

z- momentum equation

$$u_i^* \frac{\partial w_i^*}{\partial x^*} + v_i^* \frac{\partial w_i^*}{\partial y^*} + w_i^* \frac{\partial w_i^*}{\partial z^*} = \frac{1}{Re_i} \left(\frac{\partial^2 w_i^*}{\partial x^{*2}} + \frac{\partial^2 w_i^*}{\partial y^{*2}} + \frac{\partial^2 w_i^*}{\partial z^{*2}} \right) \quad (4)$$

energy equation for fluid

$$u_i^* \frac{\partial T_i^*}{\partial x^*} + v_i^* \frac{\partial T_i^*}{\partial y^*} + w_i^* \frac{\partial T_i^*}{\partial z^*} = \frac{1}{Pe_i} \left(\frac{\partial^2 T_i^*}{\partial x^{*2}} + \frac{\partial^2 T_i^*}{\partial y^{*2}} + \frac{\partial^2 T_i^*}{\partial z^{*2}} \right) \quad (5)$$

where i is represented the subscript h or c which refer to the lower and upper (hot and cold) channels respectively. The diffusion equation for solid becomes

$$\frac{\partial^2 T_s^*}{\partial x^{*2}} + \frac{\partial^2 T_s^*}{\partial y^{*2}} + \frac{\partial^2 T_s^*}{\partial z^{*2}} = 0 \quad (6)$$

The dimensionless boundary conditions are:

For lower channels (hot fluid) ($0 \leq z^* \leq H_h^*$)

At $x^* = 0$, $0 \leq y^* \leq W_{ch}^*$

$$u_{h,in}^* = 1, v^* = 0, w^* = 0, T_h^* = 1$$

$$p_{h,in}^* = \frac{p_{h,in}}{\rho u_{h,in}^2}$$

At $x^* = \frac{L}{D_h}$, $0 \leq y^* \leq W_{ch}^*$

$$\frac{\partial u^*}{\partial x^*} = \frac{\partial v^*}{\partial x^*} = \frac{\partial w^*}{\partial x^*} = \frac{\partial T_h^*}{\partial x^*} = 0$$

At $y^* = 0$, $0 \leq x^* \leq L^*$

$$u^* = v^* = w^* = \frac{\partial T_h^*}{\partial y^*} = 0$$

At $y^* = W_{ch}^*$, $0 \leq x^* \leq L^*$

$$u^* = v^* = w^* = \frac{\partial T_h^*}{\partial y^*} = 0$$

$$\text{At } z^* = 0, 0 \leq x^* \leq L^*, 0 \leq y^* \leq W_{ch}^*$$

$$u^* = v^* = w^* = \frac{\partial T_h^*}{\partial z^*} = 0$$

Fluid-solid interface

$$\text{At } z^* = H_h^*, 0 \leq x^* \leq L^*, 0 \leq y^* \leq W_{ch}^*$$

$$u^* = v^* = w^* = 0$$

$$\frac{\partial T_h^*}{\partial z^*} = K_r \frac{\partial T_s^*}{\partial z^*}$$

For upper channel (cold fluid) ($H_h^* + t_s^* \leq z^* \leq H_u^*$)

$$\text{At } x^* = 0, 0 \leq y^* \leq W_{ch}^*$$

$$u_{c,in}^* = \frac{u_{c,in}}{u_{h,in}}, v^* = w^* = T_c^* = 0$$

$$p_{c,in}^* = \frac{p_{c,in}}{\rho u_{h,in}^2}$$

$$\text{At } x^* = \frac{L}{D_h}, 0 \leq y^* \leq W_{ch}^*$$

$$\frac{\partial u^*}{\partial x^*} = \frac{\partial v^*}{\partial x^*} = \frac{\partial w^*}{\partial x^*} = \frac{\partial T_c^*}{\partial x^*} = 0$$

$$\text{At } y^* = 0, 0 \leq x^* \leq L^*$$

$$u^* = v^* = w^* = \frac{\partial T_c^*}{\partial y^*} = 0$$

$$\text{At } y^* = W_{ch}^*, 0 \leq x^* \leq L^*$$

$$u^* = v^* = w^* = \frac{\partial T_c^*}{\partial y^*} = 0$$

$$\text{At } z^* = H_u^*, 0 \leq x^* \leq L^*, 0 \leq y^* \leq W_{ch}^*$$

$$u^* = v^* = w^* = \frac{\partial T_c^*}{\partial z^*} = 0$$

Fluid-solid interface

$$\text{At } z^* = H_h^* + t_s^*, 0 \leq x^* \leq L^*, 0 \leq y^* \leq W_{ch}^*$$

$$u^* = v^* = w^* = 0$$

$$\frac{\partial T_c^*}{\partial z^*} = K_r \frac{\partial T_s^*}{\partial z^*}$$

Solid wall boundary conditions ($H_h^* \leq z^* \leq H_h^* + t_s^*$)

At $x^* = 0$, $0 \leq y^* \leq W_{ch}^*$

$$\frac{\partial T_s^*}{\partial x^*} = 0$$

At $x^* = \frac{L}{D_h}$, $0 \leq y^* \leq W_{ch}^*$

$$\frac{\partial T_s^*}{\partial x^*} = 0$$

At $y^* = 0$, $0 \leq x^* \leq L^*$

$$\frac{\partial T_s^*}{\partial y^*} = 0$$

At $y^* = W_{ch}^*$, $0 \leq x^* \leq L^*$

$$\frac{\partial T_s^*}{\partial y^*} = 0$$

At $z^* = H_h^*$, $0 \leq x^* \leq L^*$, $0 \leq y^* \leq W_{ch}^*$

$$\frac{\partial T_h^*}{\partial z^*} = K_r \frac{\partial T_s^*}{\partial z^*}$$

At $z^* = H_h^* + t_s^*$, $0 \leq x^* \leq L^*$, $0 \leq y^* \leq W_{ch}^*$

$$\frac{\partial T_c^*}{\partial z^*} = K_r \frac{\partial T_s^*}{\partial z^*}$$

By solving the above governing equations using FORTRAN code the temperature distribution is determined in the hot, cold fluid and solid domains. From these distributions one can determine the axial heat conduction and exchanger effectiveness.

Heat exchanger effectiveness is the ratio of actual heat transfer to the maximum possible heat that can be transferred [10]:

$$\varepsilon = \frac{q}{q_{max,possible}} \quad (7)$$

where

$$q_{max} = C_{min}(T_{h,in} - T_{c,in}) \quad (8)$$

and

$$q = C_c (T_{c,out} - T_{c,in}) = C_h (T_{h,in} - T_{h,out}) \quad (9)$$

where $C_h = m_h c_h$ and $C_c = m_c c_c$

then the effectiveness is

$$\varepsilon = \frac{C_c(T_{c,out}-T_{c,in})}{C_{min}(T_{h,in}-T_{c,in})} = \frac{C_h(T_{h,in}-T_{h,out})}{C_{min}(T_{h,in}-T_{c,in})} \quad (10)$$

For the axial heat conduction in section x is

$$q_x'' = \left(k_s \frac{\bar{T}_{s,i} - \bar{T}_{s,i+1}}{\Delta x} \right)_x \quad (11)$$

Where, $\bar{T}_{s,i}$ is the average solid temperature, $\bar{T}_{s,i+1}$ at the next section and Δ the distance between the two sections as shown in figure 3.

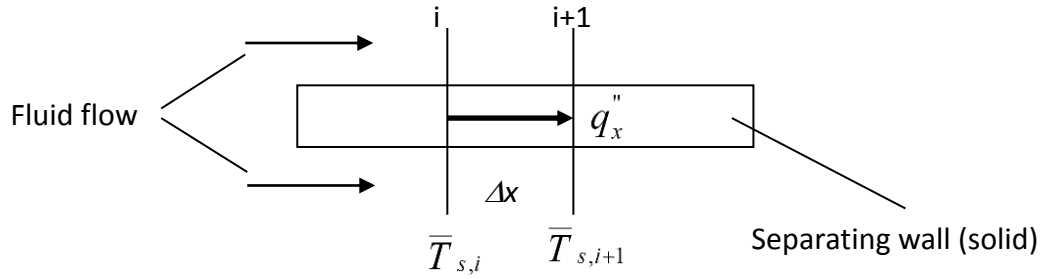


Figure 3 Schematic of separating wall.

3. NUMERICAL SOLUTION

Finite-volume method adopted which is applied to the integral form of the governing equations over the control volume (cell) as shown in figure 4. A cell containing node **P** has four neighbouring nodes identified as west, east, south and north nodes (**W**, **E**, **S**, **N**). The notation, **w**, **e**, **s** and **n** are used to refer to the west, east, south and north cell faces respectively. The methods which depend on this technique such central differencing scheme, upwind differencing scheme, hybrid differencing scheme and others. However, the present work is adopted on the hybrid differencing scheme with staggered grids arrangement to solve pressure-velocity coupling which associated with present problem and SIMPLE algorithm is used as listed in [11].

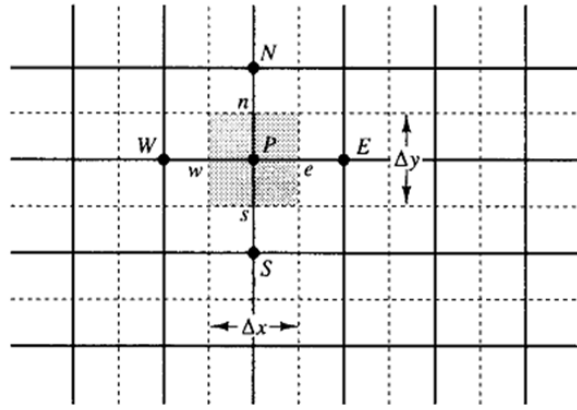


Figure 4 A cells in two-dimensional and neighbouring nodes taken from [11].

SIMPLE algorithm is implicit method are preferred for steady state and slow transient flows, because they have less stringent time steps restrictions as compared the explicit schemes. Many solutions methods for steady incompressible flows use a pressure (or pressure - correction) equation to solve pressure-velocity coupling [12]. Discretized u -component equation (2) is written in the following form [11]

$$a_{(i,J,K)}^* u_{i(J,K)}^* = \sum a_{nb}^* u_{i(nb)}^* + (p_{i(I-1)}^* - p_{i(I)}^*) A_x^* \quad (12)$$

where, $\sum a_{nb}^* u_{i(nb)}^*$ is the summation of neighboring components for u -component and the subscript i refer to cold or hot fluid. The values of coefficients $a_{(i,J,K)}^*$ and a_{nb}^* in equation (12) are calculated by using the hybrid method. However, to initiate the SIMPLE calculation process a pressure field p_i^* is guessed. Discretised momentum equation (2) is solved using the guessed pressure field to yield velocity component u_i^{**} as follows [11]

$$a_{(i,J,K)}^* u_{i(J,K)}^{**} = \sum a_{nb}^* u_{i(nb)}^{**} + (p_{i(I-1)}^{**} - p_{i(I)}^{**}) A_x^* \quad (13)$$

Now we defined the correction p_i^* as the difference between the correct pressure field p_i^* and the guessed pressure field p_i^{**} , so that

$$p_i^* = p_i^{**} + p_i^* \quad (14)$$

Similarly we defined velocity correction u_i^* to relate the correct velocity u_i^* to the guessed velocity solution u_i^{**}

$$u_i^* = u_i^{**} + u_i^* \quad (15)$$

Subtraction of equation (13) from equation (12) gives

$$a_{(i,J,K)}^* (u_{i(J,K)}^* - u_{i(J,K)}^{**}) = \sum a_{nb}^* (u_{i(nb)}^* - u_{i(nb)}^{**}) + [(p_{i(I-1)}^* - p_{i(I-1)}^{**}) - (p_{i(I)}^* - p_{i(I)}^{**})] A_x^* \quad (16)$$

Using correction formulae (14) and (15), the equation (16) may be rewritten as follows

$$a_{(i,J,K)}^* u_{i(J,K)}^* = \sum a_{nb}^* u_{i(nb)}^* + (p_{i(I-1)}^* - p_{i(I)}^*) A_x^* \quad (17)$$

At this point an approximation is introduced: $\sum a_{nb}^* u_{i(nb)}^*$ is dropped to simplify equation (17) for velocity correction. Omission of that term is the main approximation of the SIMPLE [11]. We obtain

$$u_{i(J,K)}^* = d_{(i,J,K)}^* (p_{i(I-1)}^* - p_{i(I)}^*) \quad (18)$$

where $d_{(i,J,K)}^* = A_x^* / a_{(i,J,K)}^*$. Equation (18) describe the correction to be applied to u -component through equation (15), which gives

$$u_{i(J,K)}^* = u_{i(J,K)}^* + d_{(i,J,K)}^* (p_{i(I-1)}^* - p_{i(I)}^*) \quad (19)$$

Similar expression exist for $u_{i(i+1,J,K)}^*$ [11]

$$u_{i(i+1,J,K)}^* = u_{i(i+1,J,K)}^* + d_{(i+1,J,K)}^* (p_{i(I)}^* - p_{i(I+1)}^*) \quad (20)$$

where $d_{(i+1,J,K)}^* = A_x^* / a_{(i+1,J,K)}^*$.

The SIMPLE algorithm gives a method of calculating pressure and velocity. The method is iterative and when other scalars like present problem are coupled to the momentum equations, the calculations needs to be done sequentially [11]. The sequence of operations in a FORTRAN procedure which employs the SIMPLE algorithm is given in figure 5.

In figure 5, the correct pressure field p_i^* and correct velocity field u_i^* , v_i^* and w_i^* for two channels are obtained separately. There is no coupling between the two channels for these variables as shown in the steps 1, 2 and 3. The previous steps represent the solution for pressure-velocity coupling problem (pressure-correction method). While, the last step represent the solution for convection-conduction conjugate heat transfer problem (simultaneously solution for the temperatures), where

$$b_{(I,J,K)}^* = (u_{(i,J,K)}^* - u_{(i+1,J,K)}^*) A_x^* + (v_{(I,j,K)}^* - v_{(I,j+1,K)}^*) A_y^* + (w_{(I,J,k)}^* - w_{(I,J,k+1)}^*) A_z^* \quad (21)$$

the A_x^* , A_y^* and A_z^* represents the control volume face area in x , y and z directions.

The pressure field p_i^* is obtained by solving the pressure correction p_i^* equation. It is common practice to fix the absolute pressure at one inlet node and set the pressure correction to zero ($p_i^* = 0$) at that node. Having specified a reference value, the absolute pressure field inside the domain can now be obtained [11].

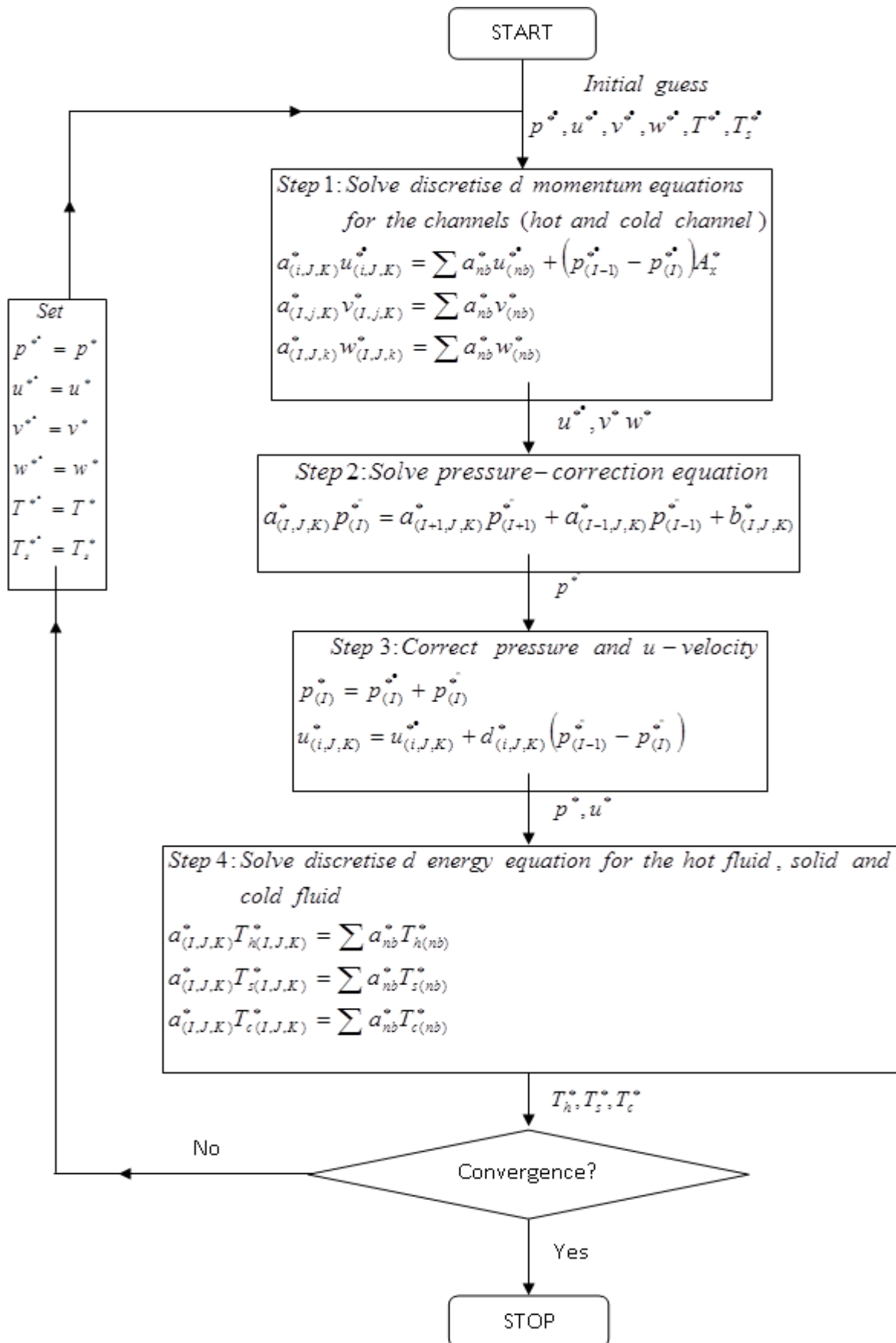


Figure 5 The SIMPLE algorithm.

4. RESULTS

In this section, the results about the influences of Reynolds number Re , thermal conductivity ratio Kr , aspect ratio α and channel volume on the local and average axial heat conduction (q_x'' and $q_{average}''$) and the effectiveness to average axial heat conduction ratio $\varepsilon/q_{average}''$ in parallel flow rectangular microchannel heat exchanger for different conditions is studied. Study the ratio $\varepsilon/q_{average}''$ to indicate the effect of axial conduction on the exchanger effectiveness, but before that it's necessary to study the $q_{average}''$ and ε each separately.

In order to verify the accuracy of present numerical model, a comparison is made between the results of present model for rectangular microchannel heat exchanger and that in literature. Figure 6 represents a comparison for dimensionless mean temperature for hot and cold fluids in rectangular microchannel heat exchanger for present numerical model and that of [7]. The dimensionless mean temperature $T_m^* = \frac{T_i - T_{c,in}}{T_{h,in} - T_{c,in}}$ is presented in this figure for the hot and cold fluids in rectangular microchannel heat exchanger against the dimensionless axial distance $x^+ = \frac{x}{D_h Re Pr}$ at $Re=100$, $Pr=0.7$ and $\frac{k_w D_h}{k_s t_s}=100$. The figure indicates for both results that dimensionless mean temperature converge to each other toward fully developed region, this refer to that the heat is transferred from hot to cold fluid. Also, the figure shows that there is a good agreement between the present numerical results and the results of [7], the maximum percentage error was $\pm 2.01\%$.

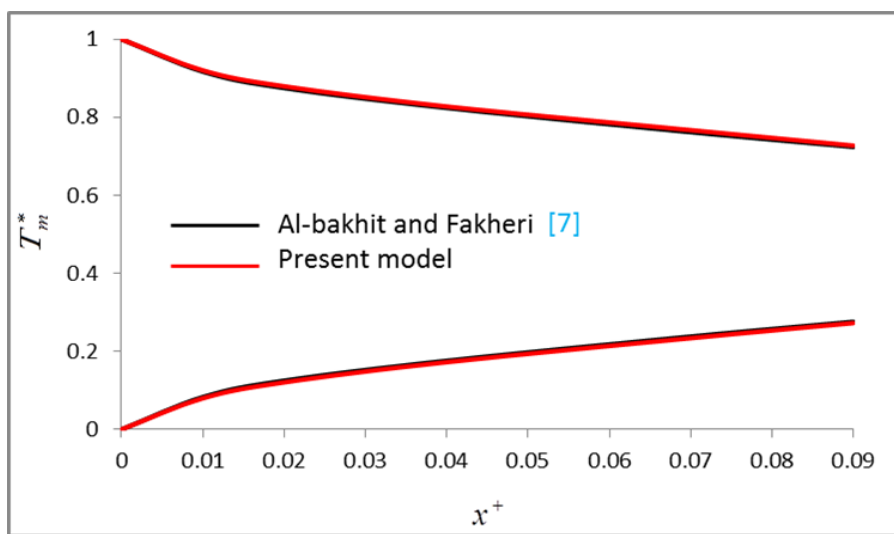


Figure 6 Comparison of the dimensionless mean temperature of the hot and cold fluids.

Figure 7 shows the longitudinal variation of the axial heat conduction q_x'' with axial distance x for different thermal conductivity ratios K_r at $t_s=50\mu\text{m}$, $\text{Re}=200$ and $\alpha=1$. For all thermal conductivity ratios, the figure indicates that the q_x'' is high in entrance region and decrease toward fully developed region due to the effect of entrance. Also, the figure shows that the q_x'' increases with K_r , due to that the heat transferred from hot fluid to cold fluid increase with increase K_r .

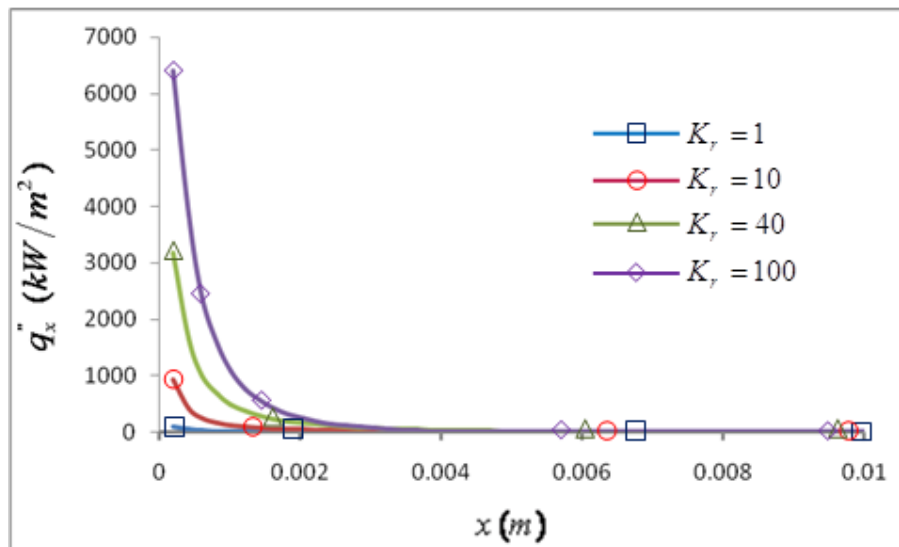


Figure 7 Longitudinal variation of the axial heat conduction with axial distance x for different values of K_r .

Figure 8 shows the variation of longitudinal axial heat conduction in the separating wall q_x'' with axial distance x for different Reynolds numbers at $K_r=1$, $t_s=50\mu\text{m}$ and $\alpha=1$. This figure shows that the q_x'' for all Reynolds number is high in the entrance region, due to the effect entrance region since maximum heat transfer accrued in the entrance region and as a result maximum value of axial heat conduction is also created in this region. As the heat transfer process increased with increasing Re and so, the fraction of axial conduction increased. Also, as q_x'' increased with Re , the heat transferred from hot fluid to cold fluid decrease and both fluids and separating wall are still conserve heat and there is no sufficient time for heat exchange at high Re .

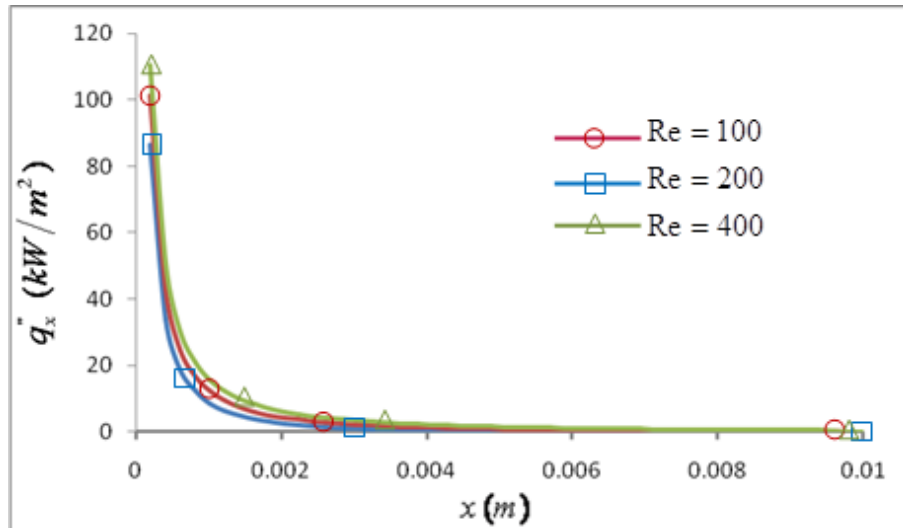


Figure 8 Longitudinal variation of the axial heat conduction with axial distance x for different Reynolds numbers.

Figure 9 illustrates the variation of average axial heat conduction $q_{average}''$ with Reynolds number Re for different aspect ratios at $K_r=1$ and $t_s=50\mu m$. For all α , the $q_{average}''$ increases with Re for the raised reason is the same in pervious figure. Also, $q_{average}''$ decrease when α decrease, this is refer to the cowing of heat transferred between both fluids overcome on the axial conduction in small α and vice versa.

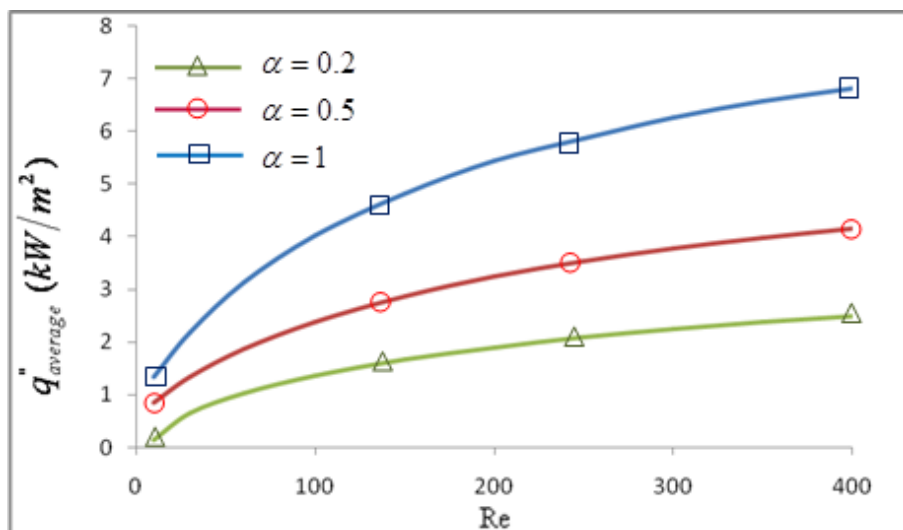


Figure 9 Variation of the average axial heat conduction with Reynolds number for different aspect ratios.

Figure 10 shows the variation of the average axial heat conduction $q''_{average}$ with aspect ratio α for different Reynolds numbers at $K_r=1$ and $t_s=50\mu\text{m}$. For all Re, $q''_{average}$ increases with α , this is because any increasing of fluid in the channel leads to increasing the heat remaining in the fluids and separating wall and then the $q''_{average}$ increase. As illustrated in previous figures $q''_{average}$ increase with Re.

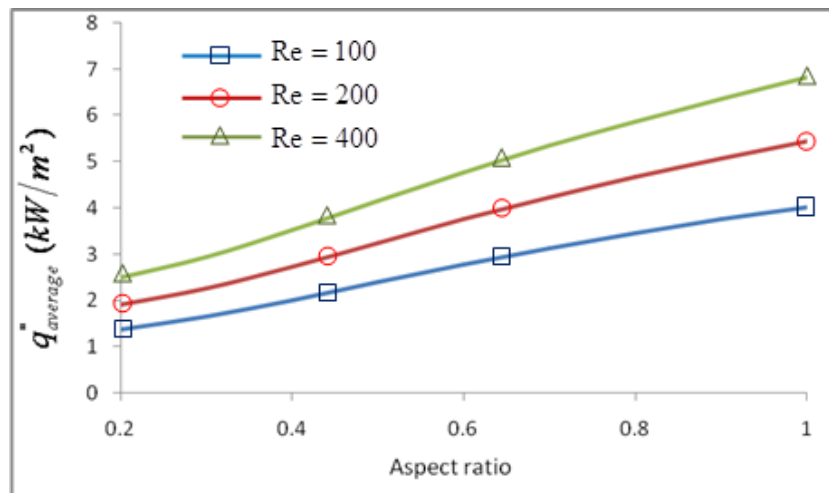


Figure 10 Variation of the average axial heat conduction with aspect ratio for different Reynolds.

Figure 11 shows the variation of the average axial heat conduction $q''_{average}$ with thermal conductivity ratio K_r for different Reynolds numbers at $t_s=50\mu\text{m}$ and $\alpha=1$ and. For all Re, $q''_{average}$ increases with K_r , this is because that more heat transferred between the two fluids through the separating wall at high K_r , and this lead to increase the axial heat conduction.

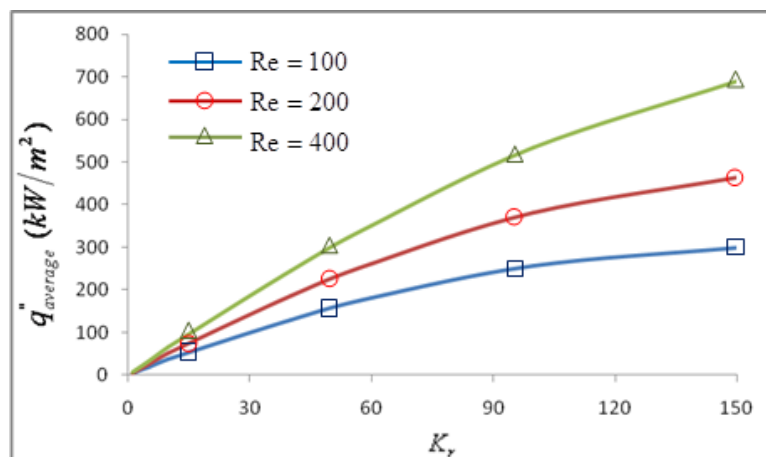


Figure 11 Variation of the average axial heat conduction with thermal conductivity ratio for different Reynolds numbers.

Figure 12 shows the variation of the average axial heat conduction $q''_{average}$ in axial direction with aspect ratio α for different thermal conductivity ratios at $Re=200$ and $t_s=50\mu m$. For all K_r , the $q''_{average}$ increases with α (due to increasing of fluid in the channel lead to increasing the heat remaining in the fluids and separating wall). Also, $q''_{average}$ increases with K_r because the heat transferred through the separating wall increases.

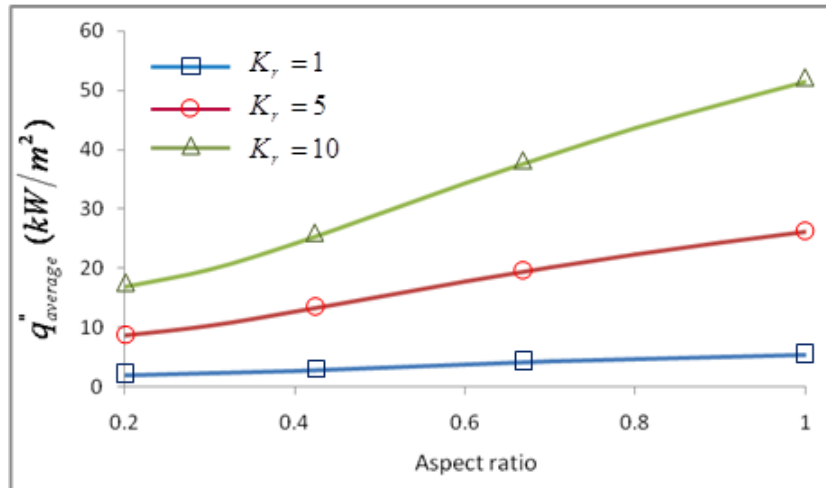


Figure 12 Variation of the average axial heat conduction with aspect ratio for different thermal conductivity ratios.

Figure 13 clarifies the variation of the average heat conduction in axial direction $q''_{average}$ with channel volume for different Reynolds number at $K_r=1$ and $t_s=50\mu m$. For all Re , $q''_{average}$ increases with channel volume in which lead to increasing the heat remaining in the fluid and separating wall and then the $q''_{average}$ increase.

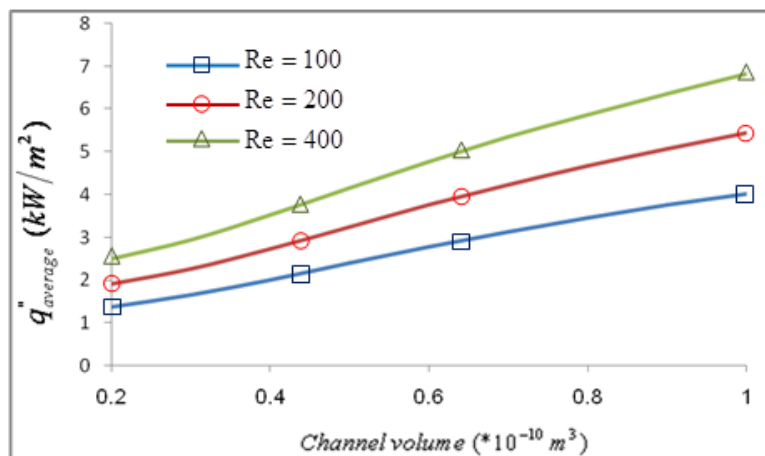


Figure 13 Variation of the average axial heat conduction with channel volume for different Reynolds numbers.

Figure 14 shows the variation of the average heat conduction in axial direction $q''_{average}$ with channel volume for different thermal conductivity ratios at $Re=200$ and $t_s=50\mu m$. For all K_r , $q''_{average}$ increases with channel volume. Also, $q''_{average}$ increase with K_r in which heat transferred between the two fluids through the separating wall increases.

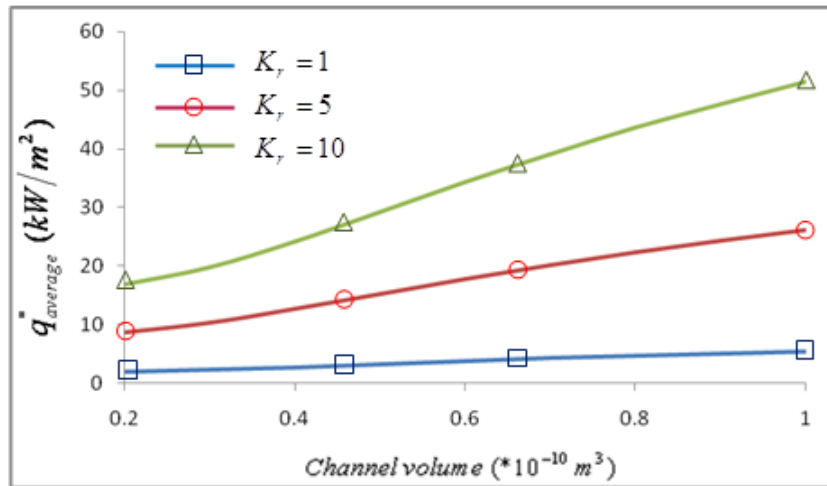


Figure 14 Variation of the average axial heat conduction with channel volume for different thermal conductivity ratios.

Figure 15 illustrates the variation of the microchannel heat exchanger effectiveness ε with Reynolds number for different aspect ratios at $K_r=1$ and $t_s=50\mu m$. The effectiveness decrease with Re for all α , this is due to that the amount fluid increases when Re increase and then ΔT decrease. On other hand, the axial conduction in the solid also increases with Re as before. The effectiveness at low Re is seems to be converge to each other but the difference increase at high Re , this refer to low Re (there is sufficient time to heat exchange and the effect of axial conduction is small in all cases and vice versa). On other hand, ε is increased at low α , and at $\alpha=0.2$ gives best ε because the axial conduction decrease and heat transferred increase.

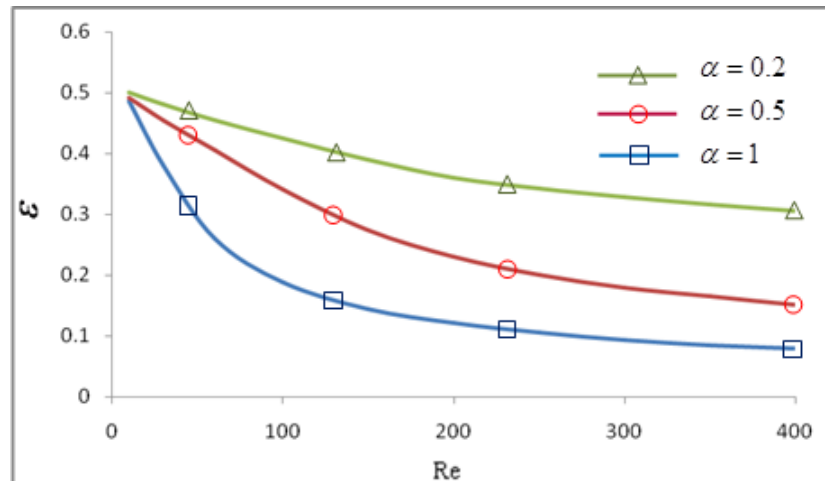


Figure 15 Variation of the microchannel heat exchanger effectiveness with Reynolds number for different aspect ratios.

Figure 16 illustrates the variation of microchannel heat exchanger effectiveness ε with thermal conductivity ratio K_r at $\alpha=1$ and $t_s=50\mu\text{m}$ for different Reynolds numbers. For all Re, the effectiveness increases with increase K_r and more heat transferred from hot to cold fluid in spite of the axial conduction, also increases with K_r , but the heat transfer overcome on it. Also, the figure indicates that the ε is higher at $\text{Re}=100$.

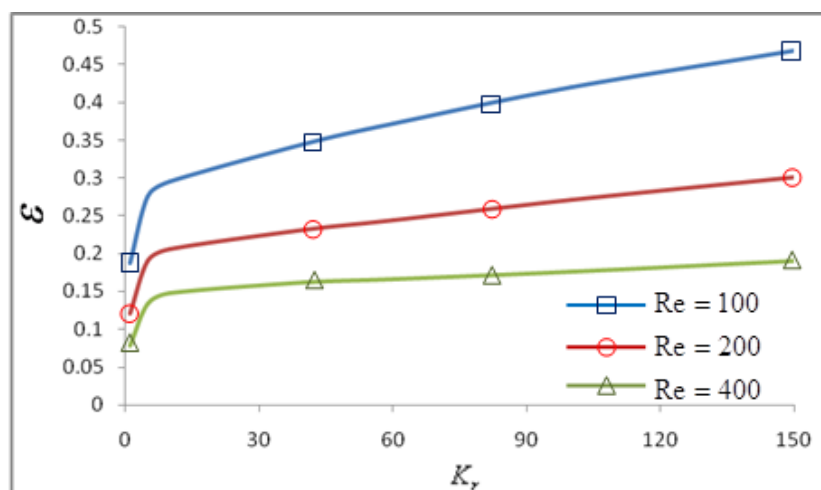


Figure 16 Variation of the heat exchanger effectiveness with thermal conductivity ratios for different Reynolds numbers.

Figure 17 shows the variation of the microchannel heat exchanger effectiveness ε with aspect ratio α for different Reynolds numbers at $K_r=1$ and $t_s=50\mu\text{m}$. For all Re, the figure clarifies that the effectiveness decreases with α . This is due to the amount of fluid increases when α increase and then ΔT decrease. On other hand, the axial conduction in the solid also increases with α as shown before. Also, the figure shows that, the effectiveness at Re=100 is more than the others for same reason.

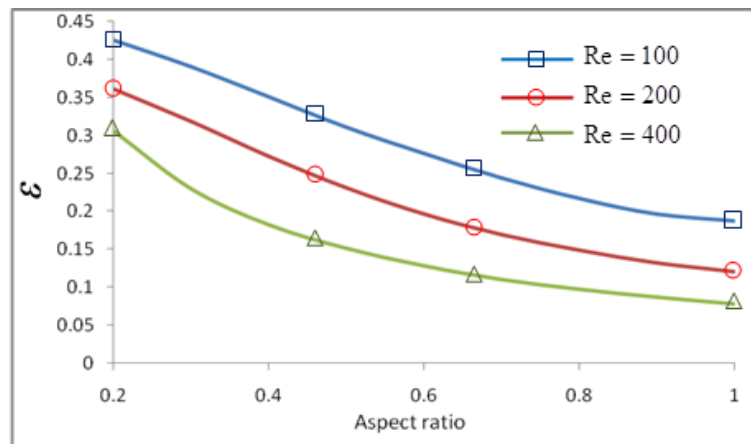


Figure 17 Variation of the heat exchanger effectiveness with aspect ratio for different Reynolds numbers.

Figure 18 illustrates the variation of the microchannel heat exchanger effectiveness ε with channel volume for different thermal conductivity ratios at $\text{Re}=200$ and $t_s=50\mu\text{m}$. For all K_r , the effectiveness decreases with channel volume. This is due to the amount of fluid increases when channel volume increase and then ΔT decrease.

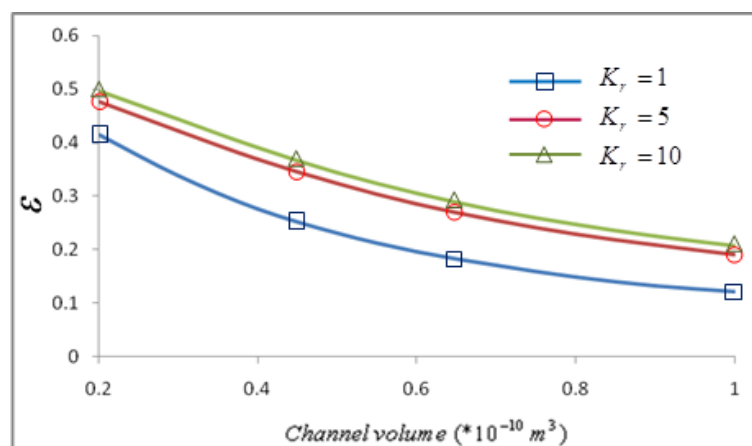


Figure 18 Variation of the heat exchanger effectiveness with channel volume for different thermal conductivity ratios.

Figure 19 shows the variation of the microchannel heat exchanger effectiveness ε with thermal conductivity ratio K_r for different aspect ratios at $Re=200$ and $t_s=50\mu m$. The ε increases with K_r , this is due to increasing the conductivity of the separating wall and more heat is transferred in this case in spite of the axial conduction also increases, but the heat transferred between the two fluids overcome on it. Also, the ε at $\alpha=0.2$ more than the others, this is because the amount of fluid decreases when the α decrease. For $\alpha=0.2$ the effectiveness increase with K_r , but normally not above $\varepsilon=0.5$ for nearly $K_r=10$ then the effectiveness will be constant.

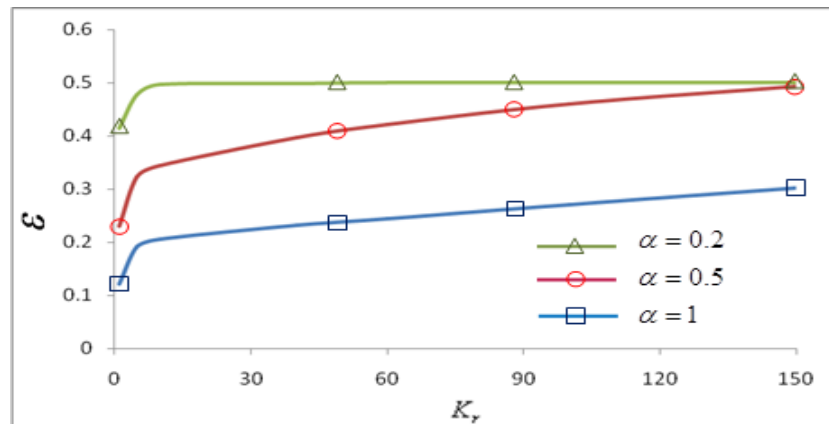


Figure 19 Variation of the heat exchanger effectiveness with thermal conductivity ratio for different aspect ratios.

Figure 20 illustrates the variation of the microchannel heat exchanger effectiveness to average axial conduction ratio $\varepsilon/q''_{average}$ with Reynolds number for different aspect ratios at $K_r=1$ and $t_s=50\mu m$. For all α , $\varepsilon/q''_{average}$ decreases with Re , this is because the effectiveness decreases and the axial conduction in the solid increases with Re . For $\alpha=0.2$ gives the best value of $\varepsilon/q''_{average}$ especially at low Re due to both the ε increase and $q''_{average}$ decrease at small Re .

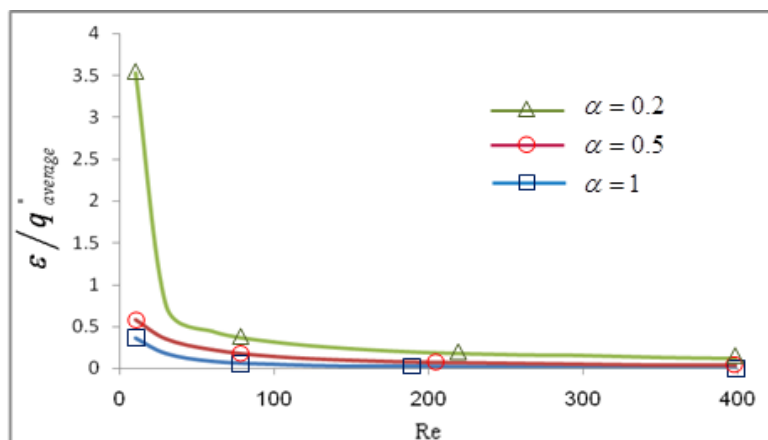


Figure 20 Variation of the microchannel heat exchanger effectiveness to average axial heat conduction ratio with Reynolds number for different aspect ratios.

Figure 21 shows the variation of the microchannel heat exchanger effectiveness to average axial heat conduction ratio $\varepsilon/q_{average}''$ with thermal conductivity ratio for different aspect ratios at $Re=200$ and $t_s=50\mu m$. $\varepsilon/q_{average}''$ decreases with K_r , this is due to the $q_{average}''$ increases with K_r , in spite of that ε also increase in this case, but the increasing in $q_{average}''$ is more than that for the ε . Also, at $\alpha=0.2$ gives the best value of $\varepsilon/q_{average}''$.

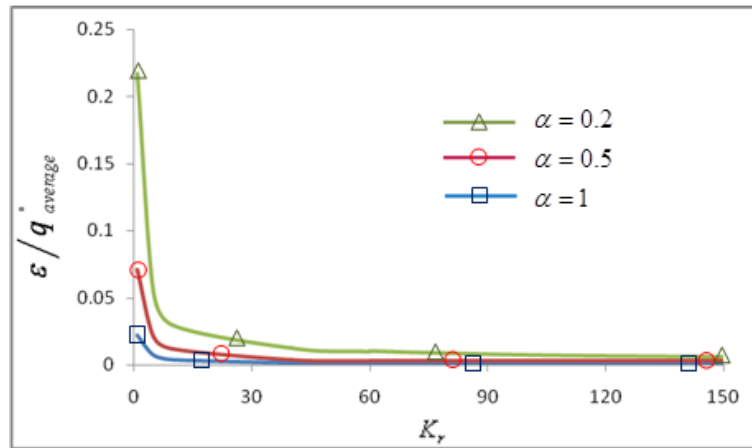


Figure 21 Variation of the microchannel heat exchanger effectiveness to average axial heat conduction ratio with thermal conductivity ratio for different aspect ratios.

Figure 22 illustrates the variation of the microchannel heat exchanger effectiveness to average axial heat conduction ratio $\varepsilon/q_{average}''$ with thermal conductivity ratio K_r for different Reynolds numbers at $\alpha=1$ and $t_s=50\mu m$. For all Re , as expected $\varepsilon/q_{average}''$ is decrease with K_r . Also, $\varepsilon/q_{average}''$ decrease with Re , since amount of fluid increases when Re increase then ΔT and ε decreases. On other hand, the axial conduction in the solid also increase with Re .

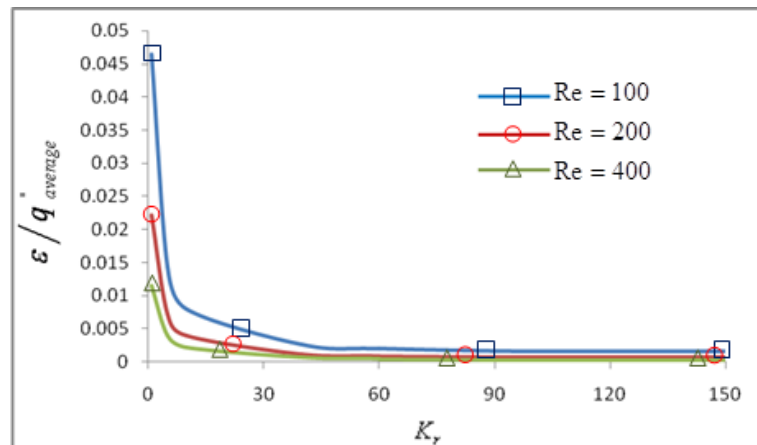


Figure 22 Variation of the microchannel heat exchanger effectiveness to average axial heat conduction ratio with thermal conductivity ratio for different Reynolds numbers.

Figure 23 shows the variation of the microchannel heat exchanger effectiveness to average axial heat conduction ratio $\varepsilon/q''_{average}$ with channel volume for different Reynolds numbers at $K_r=1$ and $t_s=50\mu\text{m}$. For all Re, $\varepsilon/q''_{average}$ decreases with channel volume this is due to the effectiveness decreases with channel volume and the axial conduction in the solid increases with channel volume.

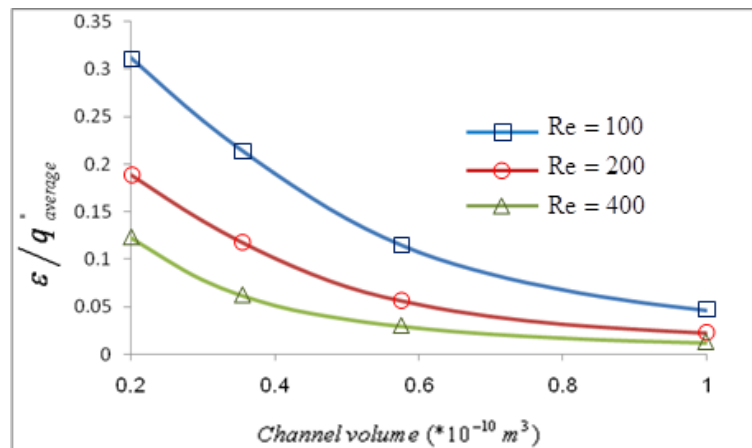


Figure 23 Variation of the microchannel heat exchanger effectiveness to average axial heat conduction ratio with channel volume for different Reynolds numbers.

Figure 24 shows the variation of the microchannel heat exchanger effectiveness to average axial heat conduction ratio $\varepsilon/q''_{average}$ with channel volume for different thermal conductivity ratios at $\text{Re}=200$ and $t_s=50\mu\text{m}$. It seen from this figure the best ratio of $\varepsilon/q''_{average}$ is at $K_r=1$.

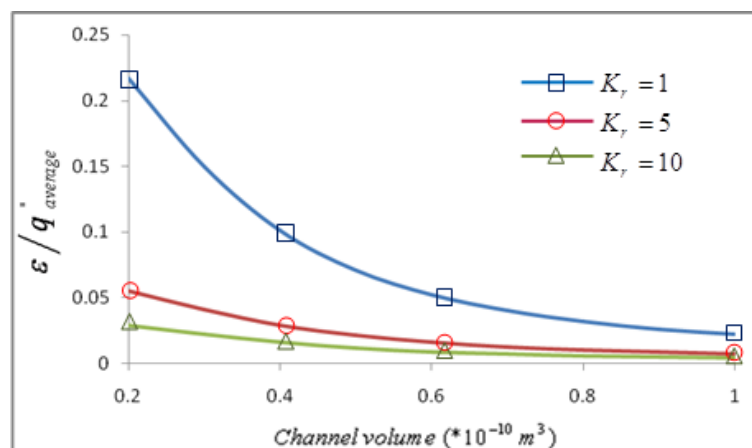


Figure 24 Variation of the microchannel heat exchanger effectiveness to average axial heat conduction ratio with channel volume for different thermal conductivity ratios.

5. CONCLUSIONS

The effects of axial heat conduction in rectangular microchannel heat exchanger with parallel flow was studied numerically through the microchannel heat exchanger effectiveness to average axial conduction ratio $\varepsilon/q''_{average}$ considering thermally and hydrodynamically developing flow conditions. The Navier–Stokes and energy equations are solved in a three-dimensional domain using the finite-volume method with FORTRAN code. However, from the results obtained the following conclusions can be drawn:

- The parameters affect the axial conduction and the effectiveness in rectangular microchannel heat exchanger are: thermal conductivity ratio K_r , Reynolds number Re , aspect ratio α and channel volume.
- Increasing of the thermal conductivity ratio K_r , Reynolds number Re , aspect ratio α and channel volume each separately lead to increase of the axial heat conduction and vice versa.
- The microchannel heat exchanger effectiveness ε increase with increasing thermal conductivity ratio K_r while decrease with increasing Reynolds number Re , aspect ratio α and channel volume each separately.
- The effect of the axial heat conduction is reflected in the microchannel heat exchanger effectiveness to average axial heat conduction ratio $\varepsilon/q''_{average}$ which decrease with increasing thermal conductivity ratio K_r in spite of the effectiveness increase due to the axial heat conduction effect, and increasing of K_r will not enhance the effectiveness, and $\varepsilon/q''_{average}$ decreases with Reynolds number Re , aspect ratio α and channel volume each separately.

REFERENCES

- [1] M.A. Al-Nimr, M. Maqableh, A.F. Khadrawi, S.A. Ammourah, "Fully developed thermal behaviors for parallel flow microchannel heat exchanger", *International Communications in Heat and Mass Transfer*, Vol. 36, pp. 385-390, 2009.
- [2] B. Mathew, H. Hegab, "Application of effectiveness-NTU relationship to parallel flow microchannel heat exchangers subjected to external heat transfer", *International Journal of Thermal Sciences*, Vol. 30, pp.1-10, 2009.
- [3] H. Al-bakhit and A. Fakheri, "A hybrid Approach for Full Numerical Simulation of Heat Exchangers", *ASME Heat Transfer Summer Conference*, San Francisco, CA, USA, pp. 17-22, 2005.
- [4] M.A. Al-Nimr, M. Maqableh, A.F. Khadrawi, S.A. Ammourah, "Fully developed thermal behaviors for parallel flow microchannel heat exchanger", *International Communications in Heat and Mass Transfer*, Vol. 36, pp. 385-390, 2009.
- [5] Yin X. and Bau H. H., "Axial Conduction Effect Performance of Micro Heat Exchangers", *ASME Winter Annual Meeting*, New Orleans, Louisiana, USA, November 28-December 3, 1992.
- [6] Stief T., Langer O. U. and Schubert K., "Numerical Investigation of Optimal Heat Conductivity in Micro Heat Exchangers", *Chem Engineering Technology*, Vol. 22, pp. 297-303, 1999.
- [7] Hussien Al-bakhit and Ahmad Fakheri, "Numerical Simulation of Heat Transfer in Simultaneously Developing Flows in Parallel Rectangular Ducts", *Applied Thermal Engineering*, Vol. 26, pp. 596-603, (2006).
- [8] Mushtaq I. Hasan, "Numerical Simulation of Counter Flow Microchannel Heat Exchanger with Different Channel Geometries and Working Fluid", *PhD Thesis*, Mechanical Engineering Department, Collage of Engineering, Basrah University, 2009.
- [9] Hyder M. Hasan, "Numerical Simulation of Parallel Flow Microchannel Heat Exchanger with Isosceles Right Triangular Geometry", *MSc Thesis*, Engineering Collage, University of Basrah, 2009.
- [10] Sean Ashman and Satish G. Kandlikar, "A review of Manufacturing Processes for Microchannel Heat Exchanger Fabrication", *Proceedings of ICNMM2006*, Fourth International Conference on Nanochannels, Microchannels and Minichannels, Limerick, Ireland, June 19-21 (2006).
- [11] H. K. Versteeg and W. Malalasekera, "An introduction to Computational Fluid Dynamics-The Finite-Volume Method", Longman, (1995).
- [12] Amit S. Kulkarni, "Effects of Surface Roughness in Microchannel Flows", *MSc Thesis*, University of Florida, (2004).